Development of Flexible Finite-Fault Inversion Method to Estimate Fault Geometry from Teleseismic Data

January 2022

Kousuke SHIMIZU

Development of Flexible Finite-Fault Inversion Method to Estimate Fault Geometry from Teleseismic Data

A Dissertation Submitted to
the Graduate School of Science and Technology,
University of Tsukuba
in Partial Fulfillment of Requirements
for the Degree of Doctor of Philosophy in Science

Doctoral Program in Geosciences,
Degree Programs in Life and Earth Sciences

Kousuke SHIMIZU

Development of Flexible Finite-Fault Inversion Method to Estimate Fault Geometry from Teleseismic Data

Kousuke Shimizu

Abstract

Finite-fault inversion of seismic waveforms has been used as a common tool to understand rupture evolution during an earthquake since 1980s. Despite the development of dense and high-quality seismic networks, especially since the 2000s, difference of source models for the same earthquake has been pointed out, which may come from modeling errors due to inappropriate assumption of source model. In particular, modeling errors of fault geometry can largely distort solutions and bias understanding of source processes. In recent years, there have been studies introducing modeling errors of fault geometry into seismic source inversion. However, fault geometry is crucial information to understand regional tectonics and earthquake dynamics, and seismic waveforms generally contain information on fault geometry as well as rupture evolution. This dissertation aimed at development of inversion methods simultaneously to estimate rupture evolution and fault geometry from teleseismic *P* waveforms. In the first step, we implemented an inversion method extracting information on fault geometry as well as rupture evolution, named potency density tensor inversion, by representing fault slip on the assumed simple fault plane by the superposition of five basis double-couple components of potency density tensor, instead of two double-couple components compatible with the fault direction. Because teleseismic *P*-wave Green's function is quite sensitive to shear-slip direction while relatively insensitive to shear-slip location, the inversion method enables us to infer spatiotemporal potency density tensor distribution without detailed assumptions about fault geometry. In the next step, making use of the developed potency density tensor inversion method, a further advanced inversion method to construct fault geometry was implemented as a non-linear inversion process, first assuming a flat fault surface and then updating the fault geometry by using the information on slip direction. The developed inversion methods were evaluated by numerical simulations and applications to teleseismic P waveforms of the M_{W} 7.7 2013 Balochistan, Pakistan and the M_{W} 7.9 2015 Gorkha, Nepal, earthquakes, which occurred along geometrically complex fault systems. The obtained spatiotemporal potency density tensor distribution of the Balochistan earthquake suggests that the rupture propagated unilaterally towards southwest from the epicenter, and its constructed fault shows a curved strike-slip fault convex to southeast, which is consistent with the observed surface ruptures. The constructed fault of the Gorkha earthquake is a reverse fault with a ramp-flat-ramp structure, which is also consistent with the fault geometry derived from geodetic and geological data. These results exhibit that the developed inversion methods work well for estimating fault geometry of an earthquake and make great contribution to the advancement of detailed understanding of earthquake source processes and tectonics.

Keywords: Finite-Fault Inversion, Fault Geometry, Nonlinear Inversion, The 2013 Balochistan Pakistan Earthquake, The 2015 Gorkha Nepal Earthquake

Contents

List of Tables

List of Figures

1. General introduction

Earthquake is a shear slip phenomenon occurring along fault surface internal of the Earth (e.g. Aki & Richards, 2002), and the seismic source is of great interest to seismologists. In general, seismic waveform contains information on both rupture evolution and fault surface geometry during an earthquake, and seismic source analyses by using seismic waveforms have been conducted since 1970s (e.g. Trifunac, 1974). One method to estimate spatial and temporal rupture distribution during an earthquake is finite-fault inversion of seismic waveforms, which has been used since 1980s (e.g. Olson & Apsel, 1982; Hartzell & Heaton, 1983; Ji *et al.*, 2002; Yagi & Fukahata, 2011a). That method requires Green's function, which is a seismic waveform per unit slip rate and represents propagation effects from a source point to an observation station, and then estimates shear-slip distribution along an assumed model fault embedded in possible source area from seismic waveforms. Finite-fault source models have also been utilized to investigate characteristics and common features of rupture among earthquakes, such as a nucleation point on fault (Mai *et al.*, 2005), scaling properties of source parameters (e.g. Ye *et al.*, 2016; Hayes, 2017), and temporal pattern of seismic moment release (e.g. Meier *et al.*, 2017). Thus, the finite-fault inversion is a key technique to help understand rupture diversity and source physics of earthquake.

Development of observation network in recent decades, especially since 2000s, has increased quality and quantity of waveform records, and we can freely and quickly get them after an earthquake via internet (e.g. IRIS Data Management Center; https://ds.iris.edu/ds/nodes/dmc/). It is natural to expect that the high quality data makes it possible to construct a source model representing more detailed rupture behavior that have conventionally been difficult to retrieve. However, non-uniqueness of the source models for the same earthquake constructed by different inversion schemes has been problematic in studies of seismic source inversion (e.g. Beresnev, 2003; Mai *et al.*, 2016), which can disturb unified interpretation and comprehension of earthquake source process. It has been pointed out that differences of assumed Earth structure and fault geometry, which are used for calculating theoretical Green's function, may be sources of the non-uniqueness (e.g. Mai *et al.*, 2016), but these are uncertain and we can never know them. Therefore, it can be said that the seismic source inversion possibly contains methodological problem and has not fully utilized the improved observational data.

In recent years, especially since 2010s, several studies aimed to suppress effects originated from uncertainty by introducing it into seismic source inversion. Yagi & Fukahata (2011a) pointed out that modeling errors originated from uncertainty of Green's function, which comes from a discrepancy between the true and the calculated Green's function due to inaccuracy of the Earth's structural model, can largely distort solutions and developed a novel inversion scheme in which data covariance matrix includes uncertainty of Green's function. The inversion scheme proposed by Yagi & Fukahata (2011a) made it possible to construct a source model that is less susceptible to choices of Earth structural model, and then, several inversion schemes introducing the uncertainty into the data covariance matrix have been developed (e.g. Minson *et al.*, 2013; Duputel *et al.*, 2014). One notable point of the inversion method of Yagi & Fukahata (2011a) is that their formulation enables us to estimate the slip-rate function stably without applying the non-negative slip constraint, which had been a common constraint to stabilize the estimation of slip (e.g. Du *et al.*, 1992; Freymueller *et al.*, 1994). Inversion method proposed by Minson *et al.* (2013) was stable and also no longer requires a smoothing constraint, which assumes spatial or spatiotemporal smoothness of slip distribution and is a common constraint to stabilize inversion estimation (e.g. Yabuki & Matsu'ura, 1992; Ide *et al.*, 1996; Fukahata *et al.*, 2003), as a prior probability density function, although a smoothing constraint that forces constant slip on each subfault is still imposed implicitly in their method (e.g. Bodin *et al.*, 2009; Nocquet, 2018). These pioneering studies have paved the way for flexible and stable seismic source inversion methods with fewer a priori constraints by better evaluation of the errors involved in seismic source inversion.

Uncertainty of fault geometry is another major source of the modeling errors that can largely distort solutions. Most finite-fault inversion studies have modeled fault geometry based on a priori information, such as aftershock distribution, surface rupture trace, centroid moment tensor (CMT) solution, and other fault models (e.g. Wald & Heaton, 1994; Koketsu *et al.*, 2004; Fielding *et al.*, 2013; Yue *et al.*, 2013; Avouac *et al.*, 2014; Ye *et al.*, 2017; Okuwaki & Yagi, 2017). In particular, for earthquakes occurring on geometrically complex fault systems, an overly simple and inappropriate approximation of the fault geometry may result in an inappropriate source model, even when the uncertainty of the Green's function is taken into account (e.g. Ragon *et al.*, 2018; Shimizu *et al.*, 2020). Ragon *et al.* (2018) took into account uncertainty of the fault geometry by introducing it into the data covariance matrix based on the framework of Duputel *et al.* (2014), allowing for robust estimation of the slip distribution even if the approximated fault geometry deviates slightly from the true one. The introduction of the uncertainty of fault geometry as well as Green's function into an inversion scheme would contribute to the construction of unbiased source models, but is not for extracting the information on fault geometry from observational data.

Another approach to suppress possible bias of source image originated from uncertainty of fault geometry, which is a new proposal in this dissertation, is to extract information on fault geometry and simultaneously to estimate shear-slip distribution from observational data. Information on fault geometry is a subject of interest to researchers because it has been shown that geometric complexity of fault is related to regional tectonics (e.g. Fielding *et al.*, 2013; Avouac *et al.*, 2014; Elliott *et al.*, 2016), to introduce spatiotemporal complexities in the regional seismicity by numerical simulation studies (e.g. Qiu *et al.*, 2016; Dal Zilio *et al.*, 2019), and to play an important role in rupture propagation (e.g. Aki, 1979; Wald & Heaton, 1994), such as controlling acceleration and deceleration of rupture propagation (Okuwaki & Yagi, 2018; Okuwaki *et al.*, 2020; Yamashita *et al.*, 2021). Therefore, fault geometry contains important information for a better understanding of earthquake dynamics and regional tectonics, and should be abundantly contained in observational data with good quality.

This dissertation proposes finite-fault inversion frameworks of teleseismic waveforms that enables us to estimate both fault geometry and shear-slip evolution, which had generally been a difficult challenge because of strong nonlinearity in the inversion analysis (e.g. Fukahata & Wright, 2008; Asano & Iwata, 2009). First, we propose the potency density tensor inversion; a new finite-fault inversion method that introduces uncertainty of Green's function into the data covariance matrix following the inversion formulation of Yagi & Fukahata (2011a) and adopts five basis double-couple components (Kikuchi & Kanamori, 1991) to represent fault slip, which means that the direction of shear-slip is not confined on the assumed fault plane. Of course, the true fault geometry should be compatible with the actual slip direction, but because the teleseismic *P*-wave Green's function is insensitive to slight changes in the absolute source location but sensitive to an assumed direction of shear-slip, the new inversion method makes it possible to estimate the spatiotemporal distribution of potency density tensors (e.g. Ampuero & Dahlen,

2005) on the assumed model fault plane. Potency density tensors, which are moment density tensors divided by rigidity, contain information on the fault displacement direction (i.e. strike, dip and rake) and hence represent information on true fault geometry. Moreover, potential bias in the source image due to inappropriate assumptions of fault geometry can be reduced in our proposed inversion framework because the shear slip direction can be represented independently of the assumed model fault plane. Unlike multiple point source inversions that have been developed to estimate focal mechanisms and source locations of several subevents from seismic waveforms (e.g. Kikuchi & Kanamori, 1991; Duputel *et al.*, 2012a,b; Duputel & Rivera, 2017; Shi *et al.*, 2018; Yue & Lay, 2020), the potency density tensor inversion resolves rupture propagation and associated changes of focal mechanism between subevents and elucidates the details of rupture propagation and its relationship to fault geometry. In Chapter 2, we present the formulation of the developed method and evaluate it through synthetic tests and application to waveforms of the M_W 7.7 2013 Balochistan, Pakistan earthquake, which occurred on geometrically complex fault systems and is a typical case of an earthquake where inappropriate fault geometry assumption can significantly distort the inversion solution.

Next, we propose an iterative inversion method to construct fault geometry from teleseismic P waveforms. This method uses the potency density tensor inversion to solve the spatial distribution of strike and dip angles on the assumed fault, and iterative solutions allow us to update the fault geometry step by step, constructing a fault geometry that is consistent with the spatial distribution of strike and dip angles. Unlike a conventional method in which fault geometry is determined subjectively by an analyst, this method makes it possible to objectively obtain fault geometry from observational data. Moreover, potency density on the obtained fault can be more directly interpreted as slip, which makes it possible to properly understand rupture propagation velocity and its relation to fault geometry. In Chapter 3, we present the methodology and evaluate it through synthetic tests and application to waveforms of the Balochistan earthquake and also the M_W 7.9 2015 Gorkha, Nepal, earthquake, which occurred on well-known, geometrically complex fault systems.

The author notes that contents of this dissertation is based on the published articles below:

- Shimizu, K., Yagi, Y., Okuwaki, R., & Fukahata, Y., 2020. Development of an inversion method to extract information on fault geometry from teleseismic data. *Geophysical Journal International*, **220**(2), 1055–1065. doi:10.1093/gji/ggz496

- Shimizu, K., Yagi, Y., Okuwaki, R., & Fukahata, Y., 2021. Construction of fault geometry by finite-fault inversion of teleseismic data. *Geophysical Journal International*, **224**(2), 1003–1014. doi:10.1093/gji/ggaa501

2. Development of potency density tensor inversion method

In this chapter, we proposes a new finite-fault inversion method, named potency density tensor inversion, that resolves spatiotemporal distribution of potency density tensor on a model fault and also mitigates effects originated from uncertainty of fault geometry. The fundamental framework of the new inversion method is the finite-fault inversion of teleseismic waveforms developed by Yagi & Fukahata (2011a). Yagi & Fukahata (2011a) showed that uncertainty of Green's function is a major source of modeling errors which can largely distort inversion solution and showed that a formulation introducing uncertainty of Green's function into the data covariance matrix makes it possible to mitigate effects of the uncertainty. Notably, the inversion method of Yagi & Fukahata (2011a) enables us to flexibly estimate rupture evolution without applying non-negative slip constraint, which has been confirmed by applications of it to inversion analyses of the M_W 9.1 2011 Tohoku-oki, the M_W 7.9 2008 Wenchuan, China, and the M_W 8.1 2017 Chiapas, Mexico earthquakes (Yagi & Fukahata, 2011b; Yagi *et al.*, 2012b; Okuwaki & Yagi, 2017). In order to develop a flexible finite-fault inversion method that estimate potency density tensor distribution during an earthquake, we adopted the inversion method proposed by Yagi & Fukahata (2011a) as a framework. Here we present mathematical formulation of the potency density tensor inversion in Section 2.1 and demonstrate it through numerical simulations in Section 2.2 and application of it to teleseismic waveforms of the M_W 7.7 2013 Balochistan, Pakistan earthquake in Section 2.3.

2.1 Mathematical formulation

In general, earthquake sources can be represented by moment rate volume density tensors $\dot{\boldsymbol{M}}(t,\xi)$ (e.g. Backus & Mulcahy, 1976) which is represented by a linear combination of five

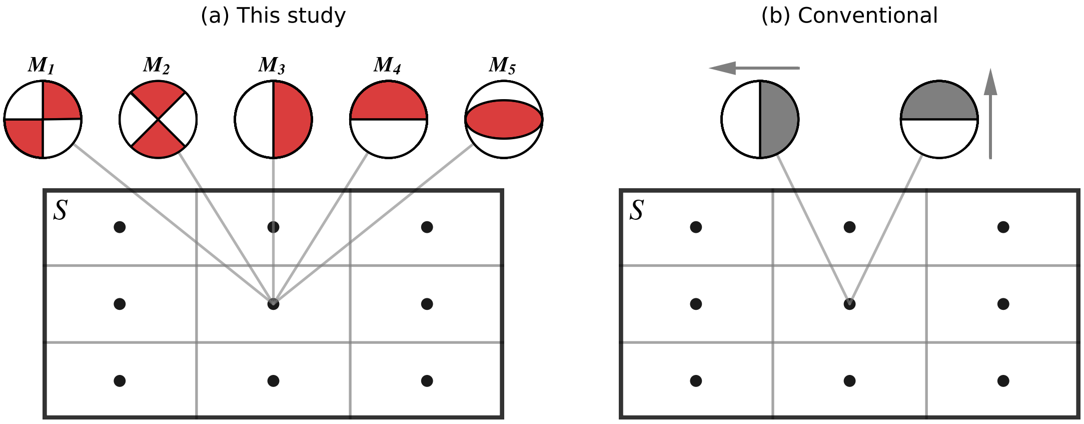

Figure 2.1: Shear-slip representations at each subfault on a model plane S by (a) the new method and (b) conventional method. Each dot represents a central point of each subfault on the model plane S. (a) The five beach balls denote the five basis double-couple components shown by (Kikuchi & Kanamori, 1991). Each component corresponds to a shear dislocation source, but is not needed to be parallel to the model plane S. The focal mechanisms, plotted by using a lower-hemisphere projection, are not rotated according to the model plane setting. (b) The two beach balls represent the two basis double-couple components corresponding to the shear dislocation sources along the model plane S. Arrows represent the slip directions of the two double-couple components whose nodal planes correspond to model plane S. The two focal mechanisms, plotted by using a lower-hemisphere projection, are rotated so that their one nodal planes match to model plane S; therefore, they are not equivalent to $\boldsymbol{M}_3$ and $\boldsymbol{M}_4$ shown in (a).

basis double-couple components $\boldsymbol{M}_q$ (Kikuchi & Kanamori, 1991) (Fig. 2.1a):

$$\dot{\boldsymbol{M}}(t,\xi) = \sum_{q=1}^{5} \dot{m}_q(t,\xi)\boldsymbol{M}_q, \tag{2.1}$$

where “five” prescribes the degree of freedom of the moment-rate tensor except for isotropic expansion sources, $\dot{m}_q(t,\xi)$ is a spatiotemporal moment rate volume density function of qth basis double-couple component, and ξ represents a position in the source area. Conventional finite-fault inversion solves a slip-rate function at each subfault with one or two directions of shear-slip along the assumed fault plane (e.g. Olson & Apsel, 1982; Ide *et al.*, 1996; Ji *et al.*, 2002), which corresponds to solving the potency rate areal density function for two double-couple components (Fig. 2.1b), where the potency rate corresponds to the moment rate divided by the rigidity. As shown in Fig. 2.1b, in the conventional scheme, one of the two nodal planes must match the model fault plane. However, we adopt the inversion framework of Yagi & Fukahata (2011a) and then propose a formulation for finite-fault inversion of teleseismic waveforms that solves the potency rate areal density function for five basis double-couple components (Fig.

2.1a),

Here a seismic waveform u_j for a far-field term observed at a station j is represented by a linear combination of moment rate volume density functions of five basis double-couple components (Fig. 2.1a):

$$u_j(t) = \sum_{q=1}^{5} \int_V G^0_{qj}(t, \xi) * \dot{m}_q(t, \xi) d\xi + e_{bj}(t), \tag{2.2}$$

where V is a three-dimensional source area, G^0_{qj} is a Green's function, e_{bj} is a background and instrumental noise, and $*$ denotes the time domain convolution operator. Eq. (2.2) represents the spatiotemporal distribution of moment rate volume density in a three dimensional model source space. In order to simply represent the three-dimensional source area as a finite-fault model in two dimensions, we assume that a finite-fault model obtained by a teleseismic body wave inversion is insensitive to a slight change of source location of the Green's function:

$$G^0_{qj}(t, \xi + \delta\xi) \approx G^0_{qj}(t, \xi), \tag{2.3}$$

where $\xi + \delta\xi$ is a neighbouring position around ξ. However, Green's function can change according to the source depth (e.g. Yagi *et al.*, 2012a; Okuwaki *et al.*, 2019), and we evaluated the sensitivity of finite-fault model to a slight change of source depth by performing numerical simulations in Section 2.2. We found some differences in source models according to source depth, such as the amplitude and the timing of moment rate peaks of source-time function, but proved that the change of source depth does not seriously affect the estimation of focal mechanisms and overall features in the source-time function (Fig. 2.8).

The approximation of eq. (2.3) makes it possible to reduce the dimension of the integral from a volume to a surface integral on a model plane S set in the source area V. Then, eq. (2.2) becomes

$$u_j(t) = \sum_{q=1}^{5} \int_S G^0_{qj}(t, \xi) * \dot{m}'_q(t, \xi) d\xi + e_{bj}(t), \tag{2.4}$$

where $\dot{m}'_q(t, \xi)$ is the moment rate areal density function, which is the the volume density of the moment rate function $\dot{m}_q$ projected on the model plane S.

The areal density of moment rate function is represented by the areal density of potency rate function $\dot{D}_q$:

$$\dot{m}'_q(t, \xi) = \mu(\xi)\dot{D}_q(t, \xi), \tag{2.5}$$

where $\mu(\xi)$ is the rigidity.

By substituting eq. (2.5) into eq. (2.4), the observed waveform u_j is represented by the areal density of potency rate function $\dot{D}_q$:

$$u_j(t) = \sum_{q=1}^{5} \int_S \tilde{G}_{qj}(t, \xi) * \dot{D}_q(t, \xi) d\xi + e_{bj}(t), \tag{2.6}$$

with

$$\tilde{G}_{qj}(t, \xi) = \mu(\xi) G^0_{qj}(t, \xi). \tag{2.7}$$

Eq. (2.6) means that the finite-fault inversion method can estimate the distribution of potency rate areal density tensors. The slip rate corresponds to potency rate areal density under a condition that a shear plane and its area are explicitly given, and the potency rate areal density corresponds to the slip rate when the slip direction of the potency rate areal density tensor lies along the model plane S.

In the conventional formulation, one of the two nodal planes of the two basis double-couple components correspond to the model plane S, which means that the fault geometry is assumed to be the model plane S (Fig. 2.1b). In this study, we adopt $q = 5$ for the areal density of potency rate function in eq. (2.6), which means that the shear plane is resolved with the five basis double-couple components and hence is no longer required to be consistent with the presumed model plane geometry a priori (Fig. 2.1a).

We represent the areal density of potency rate function $\dot{D}_q$ by a linear combination of a finite number of basis functions according to the multiple-time-window inversion scheme (e.g. Olson & Apsel, 1982):

$$\dot{D}_q \cong \sum_{k=1}^{K} \sum_{l=1}^{L} a_{qkl} X_k(\xi) T_l(t - t_k), \tag{2.8}$$

where X_k and T_l are the basis functions for space and time, respectively, and a_{qkl} are the expansion coefficients (model parameters) to be estimated from the seismic waveform. t_k is the start time of rupture at a space knot k.

Substituting eq. (2.8) into eq. (2.6), we represent the observed waveform u_j by the basis functions of space and time:

$$u_j(t) = \sum_{k=1}^{K}\sum_{l=1}^{L}\sum_{q=1}^{5} a_{qkl} \int_S \tilde{G}_{qj}(t,\xi) * \Big(X_k(\xi)T_l(t-t_k)\Big)d\xi + e_{bj}(t). \tag{2.9}$$

Adopting the formulation of Yagi & Fukahata (2011a), we introduce the modeling error of Green's function δG_{qj} as

$$\tilde{G}_{qj}(t,\xi) = G_{qj}(t,\xi) + \delta G_{qj}(t,\xi). \tag{2.10}$$

Using the modeling error of Green's function δG_{qj}, we rewrite eq. (2.9) as:

$$u_j(t) = \sum_{k=1}^{K}\sum_{l=1}^{L}\sum_{q=1}^{5} a_{qkl} \int_S \Big(G_{qj}(t,\xi) + \delta G_{qj}(t,\xi)\Big) * \Big(X_k(\xi)T_l(t-t_k)\Big)d\xi + e_{bj}(t). \tag{2.11}$$

Then, we represent the observation equation at the jth station in vector form as

$$\boldsymbol{d}_j = \boldsymbol{H}_j\boldsymbol{a} + \boldsymbol{e}_{gj}(\boldsymbol{a}) + \boldsymbol{e}_{bj}, \tag{2.12}$$

where $\boldsymbol{d}_j$ is the N_j (number of data point at the jth station) dimensional data vector representing the observed waveform u_j, $\boldsymbol{a}$ is the M $(= 5KL)$ dimensional model parameter vector, $\boldsymbol{H}_j$ is the $N_j \times M$ dimensional coefficient matrix representing convolutions of the calculated Green's functions and basis functions in time, $\boldsymbol{e}_{gj}$ is the N_j dimensional vector representing the modeling error of Green's function, and $\boldsymbol{e}_{bj}$ is the N_j dimensional vector that represents the background and instrumental noise. We calculate the data covariance matrix of $\boldsymbol{d}$ from eq. (2.12) following the method of Yagi & Fukahata (2011a), and represent the stochastic model relating the data vector $\boldsymbol{d}$ for all stations by the model parameters $\boldsymbol{a}$.

We adopt the smoothing constraint as prior constraints on each areal density of potency rate function $\dot{D}_q$ in space and time:

$$\nabla^2 \dot{D}_q(t,\xi) + e_s = 0, \tag{2.13}$$

$$\frac{\partial^2}{\partial t^2}\dot{D}_q(t,\xi) + e_t = 0. \tag{2.14}$$

As shown in eq (2.13), we also apply the smoothing constraint to spatial distribution of areal density of potency rate function $\dot{D}_q$ instantaneously at each time step, which stabilizes inversion solution better than the smoothing constraint only on the total spatial distribution (e.g. Ide *et al.*, 1996; Ji *et al.*, 2002).

We rewrite eqs (2.13) and (2.14) in vector form as,

$$\boldsymbol{S}_1\boldsymbol{a} + \boldsymbol{e}_s = \boldsymbol{0}, \tag{2.15}$$

$$\boldsymbol{S}_2\boldsymbol{a} + \boldsymbol{e}_t = \boldsymbol{0}, \tag{2.16}$$

where $\boldsymbol{S}_1$ and $\boldsymbol{S}_2$ are $M \times M$ dimensional matrices. Following the formulation developed by Fukahata *et al.* (2003, 2004), we combine these two prior constraints into a single probability density function.

Following the method of Yagi & Fukahata (2011a), the unknown scaling parameters of the modeling error, background noise, and prior constraints are determined on the basis of Akaike's Bayesian Information Criterion (ABIC; Akaike, 1980; Yabuki & Matsu'ura, 1992) and model parameter vectors are iteratively solved in the rest of the formulation process. Fukuda & Johnson (2008) demonstrated that ABIC without applying non-negative constraints avoids the problems of over-smoothing and under-smoothing, and hence our inversion scheme, which employs ABIC without non-negative constraints, also avoids them. However, Yamashita *et al.* (2021) and Yamashita *et al.* (2021b) pointed out that our inversion scheme tends to solve spatiotemporally smooth distribution of potency density tensor and they proposed new smoothing constraints to resolve clearer source image, which will be discussed in Chapter 4.

For a simple description, we use "potency rate density" and "potency density" instead of "potency rate areal density" and "potency areal density" in the following sections.

2.2 Numerical simulation

In order to test the formulation developed in this study, we performed numerical simulations in which we analyze synthetic waveforms generated by using a prepared source model

Table 2.1: Near-source velocity model derived from Avouac *et al.* (2014) for calculating Green's functions.

V_P (km/s)	V_S (km/s)	Density (10^3kg/m^3)	Thickness (km)
5.44	3.00	2.50	4.00
6.25	3.45	2.60	12.00
6.53	3.60	2.70	14.00
6.80	3.90	2.90	12.00
7.50	4.30	2.90	3.00
8.11	4.49	3.30	0.00

and theoretical Green's function. We took 26.951°N and 65.501°E as the epicenter of input source models, and then calculated input synthetic waveforms for the selected stations shown in Fig. 2.9d by using theoretical Green's functions and input source models (Figs 2.2–2.6). We calculated theoretical Green's functions following the method shown by Kikuchi & Kanamori (1991) at a 0.1 s interval by adopting the one-dimensional near source velocity structure (Table 2.1) used in Avouac *et al.* (2014), and set the attenuation time constant t^* for the P wave to be 1.0 s. We added an error of Green's function and background noise in the synthetic waveforms. We added random Gaussian noise with zero mean and a standard deviation of 5 % of maximum amplitude of each calculated Green's function as an error of Green's function, and added random Gaussian noise with zero mean and a standard deviation of 1 μm to synthetic waveforms as the background noise. In the inversion process, we resampled the input waveform data at a 0.8 s interval without applying any filter to either the input waveforms or the theoretical Green's functions.

We prepared 3 cases of input source models to check the performance of our new method. In the case 1, we prepared a simple reverse faulting model with two large potency density areas on a single flat fault plane with a length of 150 km and a width of 40 km. The fault plane was configured by a strike of 90° and a dip of 45°, which was discretized into 10 km × 10 km subfaults and a depth of 25 km was adopted as the hypocentral depth (Figs 2.2a and 2.3a). Total duration of the input potency rate density function at each subfault was asssumed to be 10 s.

In the case 2, we prepared a input source model with variable focal mechanisms. The input source model consists of four large potency density areas with focal mechanisms of $\boldsymbol{M}_1$, $\boldsymbol{M}_2$, $\boldsymbol{M}_3$, and $\boldsymbol{M}_5$ (Fig. 2.1), respectively, on a single model plane with a length of 190 km and a width of 50 km. The fault plane was configured by a strike of 180° and a dip of 0°, which was discretized into 10 km × 10 km subfaults and a depth of 25 km was adopted as the hypocentral

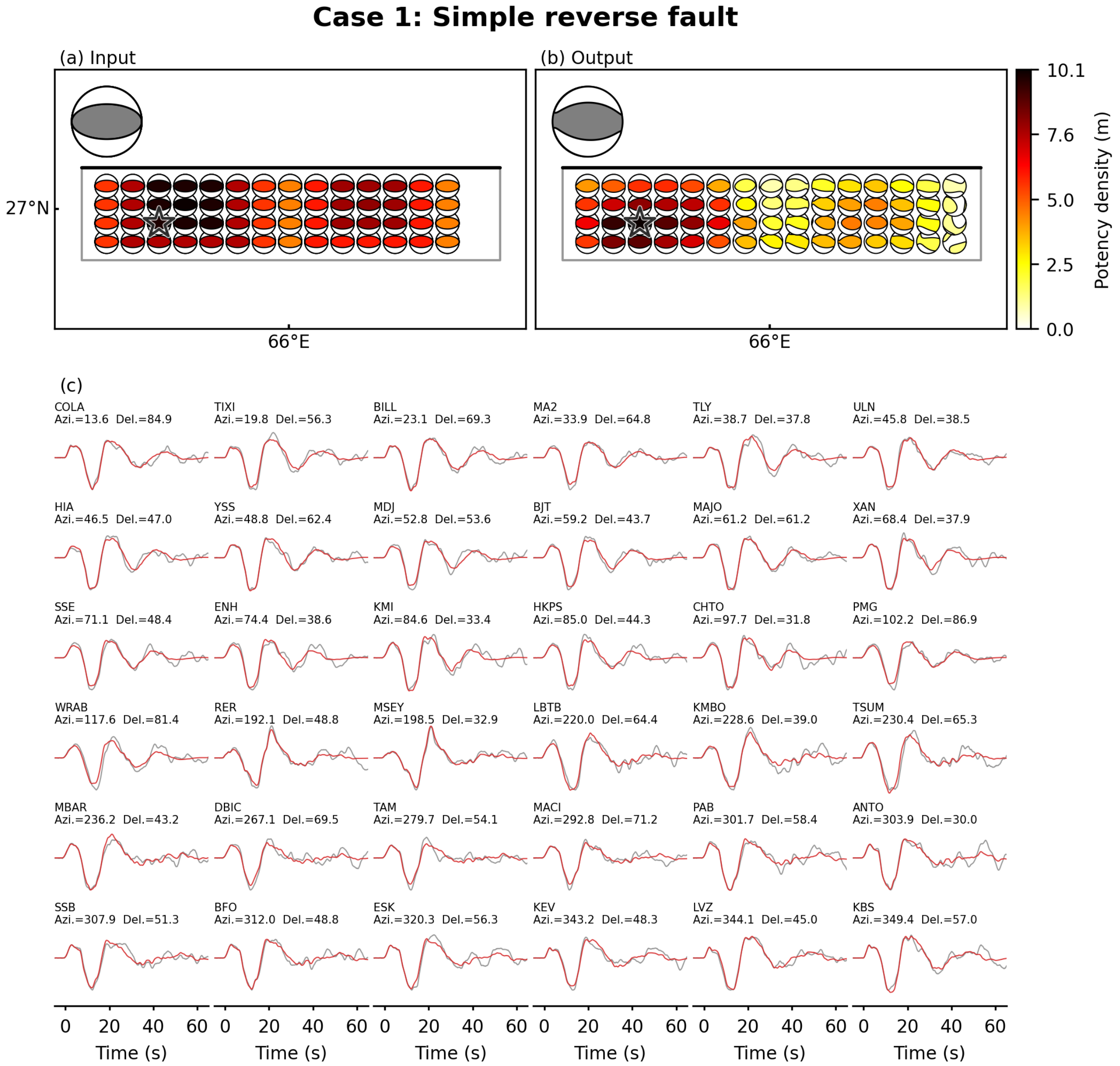

Figure 2.2: (a) Input source model, (b) Output source model, and (c) waveform fitting between input and output synthetic waveforms at all stations in the case 1. (a, b) The beach ball color shows the potency density. The gray line outlines the model fault plane, and the black line shows the top of the model fault plane. The star denotes the epicenter. The large gray beach ball represents the total moment tensor obtained by integrating the potency density tensors in space. (c) Gray and red traces are input and output waveforms, respectively. Station code, azimuth, and epicentral distance of each station are shown above the trace.

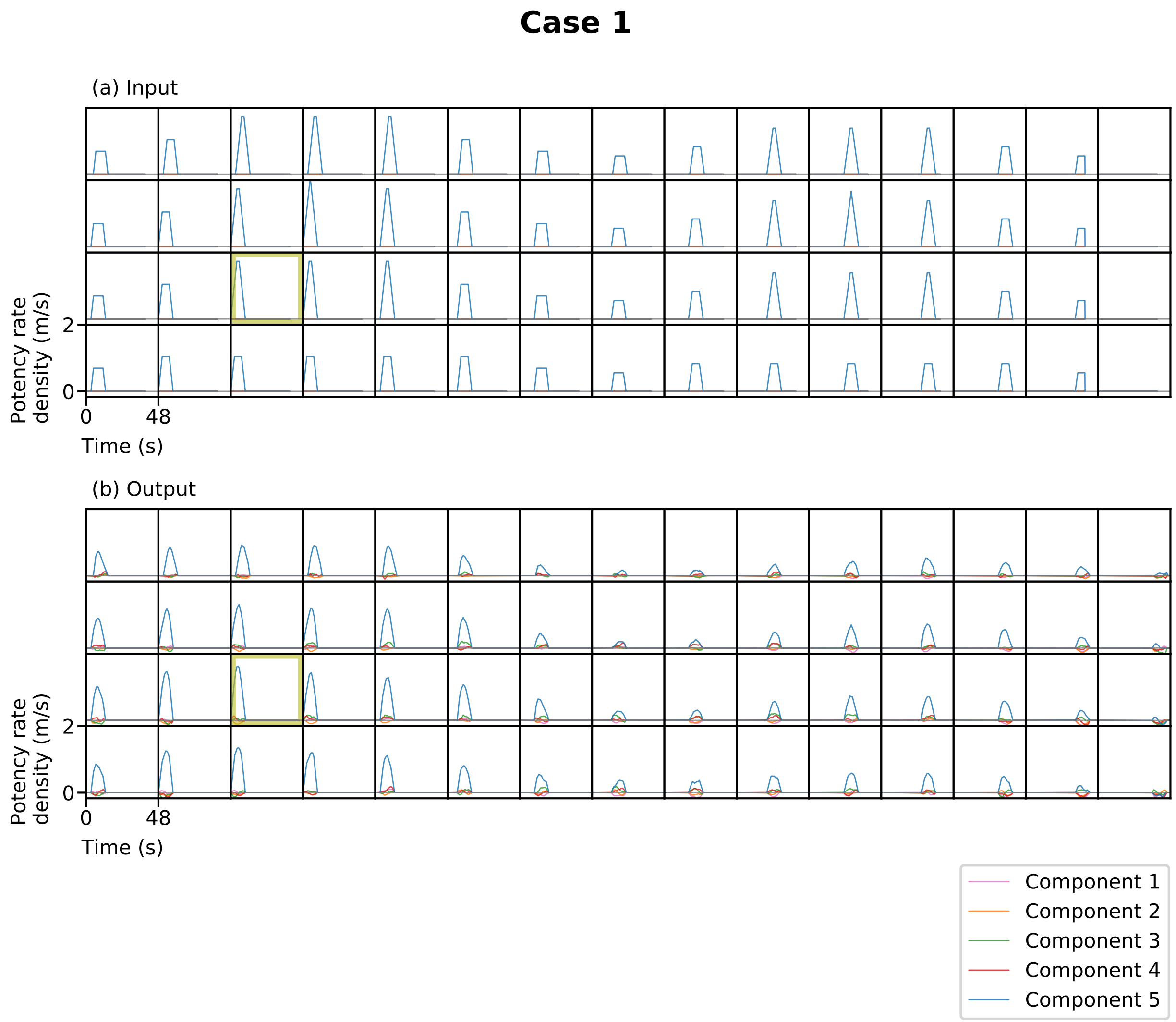

Figure 2.3: Potency rate density functions of (a) input and (b) Output source models at all subfaults in the case 1. Each colored trace corresponds to the basis double-couple compnent shown in Fig. 2.1. The cell outlined by yellow line represents the initially ruptured subfault.

depth (Figs 2.4a and 2.5a). Total duration of the input potency rate density function at each subfault was asssumed to be 10 s.

In the inversion process of the cases 1 and 2, we assumed that a model plane whose geometry is the same as the input one.

In the case 3, we prepared a left-lateral strike-slip faulting model within a bending fault consisting of two, 60 km long and 30 km wide, vertical fault planes, with strikes of 135° and 180°, respectively (Figs 2.6 a and b). The input fault plane was discretized into 10 km and 5 km subfaults along strike and dip, respectively, and a depth of 30 km was adopted as the hypocentral depth (Figs 2.6 a and b). Total duration of the input potency rate density function at each subfault was assumed to be 20 s. In our new method, we assume that a finite-fault model obtained by a teleseismic body wave inversion is insensitive to a slight change of source location of the Green's function (eq. 2.3), which means that the model plane used for inversion analysis can be spatially deviated from the true fault plane to some extent. Therefore, in the inversion process of this case, we set a single model plane, 120 km long and 40 km wide, with a strike of 165° and a dip of 0°, horizontally covering the input source area (Fig. 2.6b) to verify the extent to which the assumption affects the solution. The model plane was discretized into 10 km × 10 km subfaults and we took a depth of 30 km as the initial rupture depth.

For all cases, we assumed that the total duration of the potency rate density function used for the inversion analysis is the same as the input one.

The results show that the spatiotemporal distribution of focal mechanisms in the input source models were well reproduced by the obtained output source models (Figs 2.2b, 2.3b, 2.4b, 2.5b, 2.6c and d), although the amplitude of output potency rate density function at each subfault is smaller and smoother than the input ones (Figs 2.3b and 2.5b), which may be originated from the input models which do not fully obey our smoothing constraints (eqs 2.13 and 2.14). The input synthetic waveforms were well explained by the output waveforms (Figs 2.2c, 2.4c and 2.6e).

In the case 3, it should be noted that the 45° change of a strike orientation of strike-slip mechanism during the rupture evolution in the input source model can be reproduced in the output source model adopting the horizontal model plane (Figs 2.6c, 2.6d and 2.7), and the output waveforms explained the input synthetic waveforms well (Fig. 2.6e). This result implies that the approximation of teleseismic *P* waveform Green's function (eq. 2.3) works well and simplified assumptions of model space, such as the single horizontal model plane, can be adopted

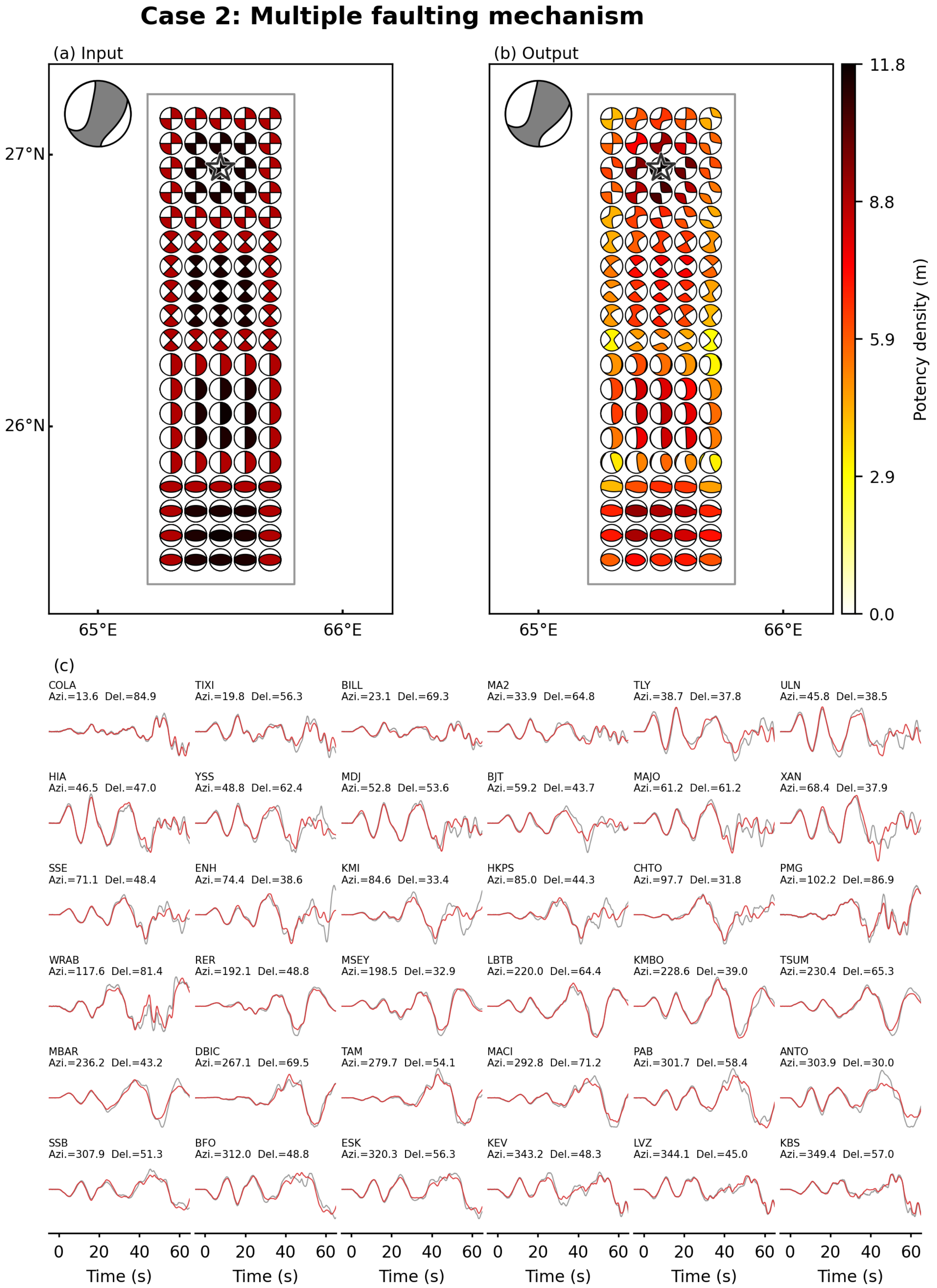

Figure 2.4: *Caption next page.*

Figure 2.4: (a) Input source model, (b) Output source model, and (c) waveform fitting at all stations between input and output synthetic waveforms in the case 2. (a, b) The beach ball color shows the potency density. The gray line outlines the model fault plane. The star denotes the epicenter. The large gray beach ball represents the total moment tensor obtained by integrating the potency-density tensors in space. (c) Gray and red traces are input and output waveforms, respectively. Station code, azimuth, and epicentral distance of each station are shown above the traces.

for estimation of potency density tensor distribution of an earthquake.

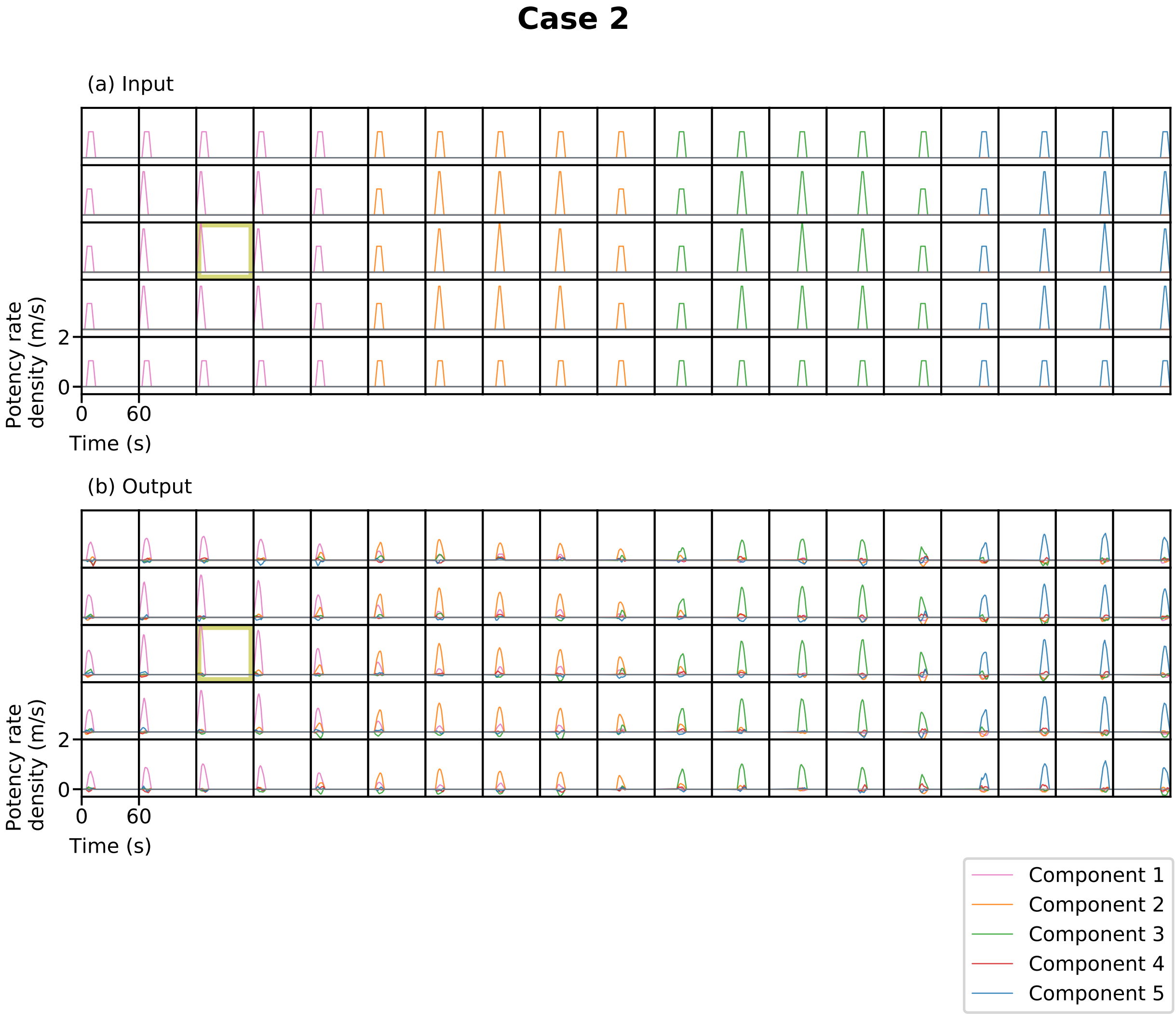

Figure 2.5: Potency rate density functions of (a) input and (b) Output source models at all subfaults in the case 2. Each colored trace corresponds to the basis double-couple compnent shown in Fig. 2.1. The cell outlined by yellow line represents the initially ruptured subfault.

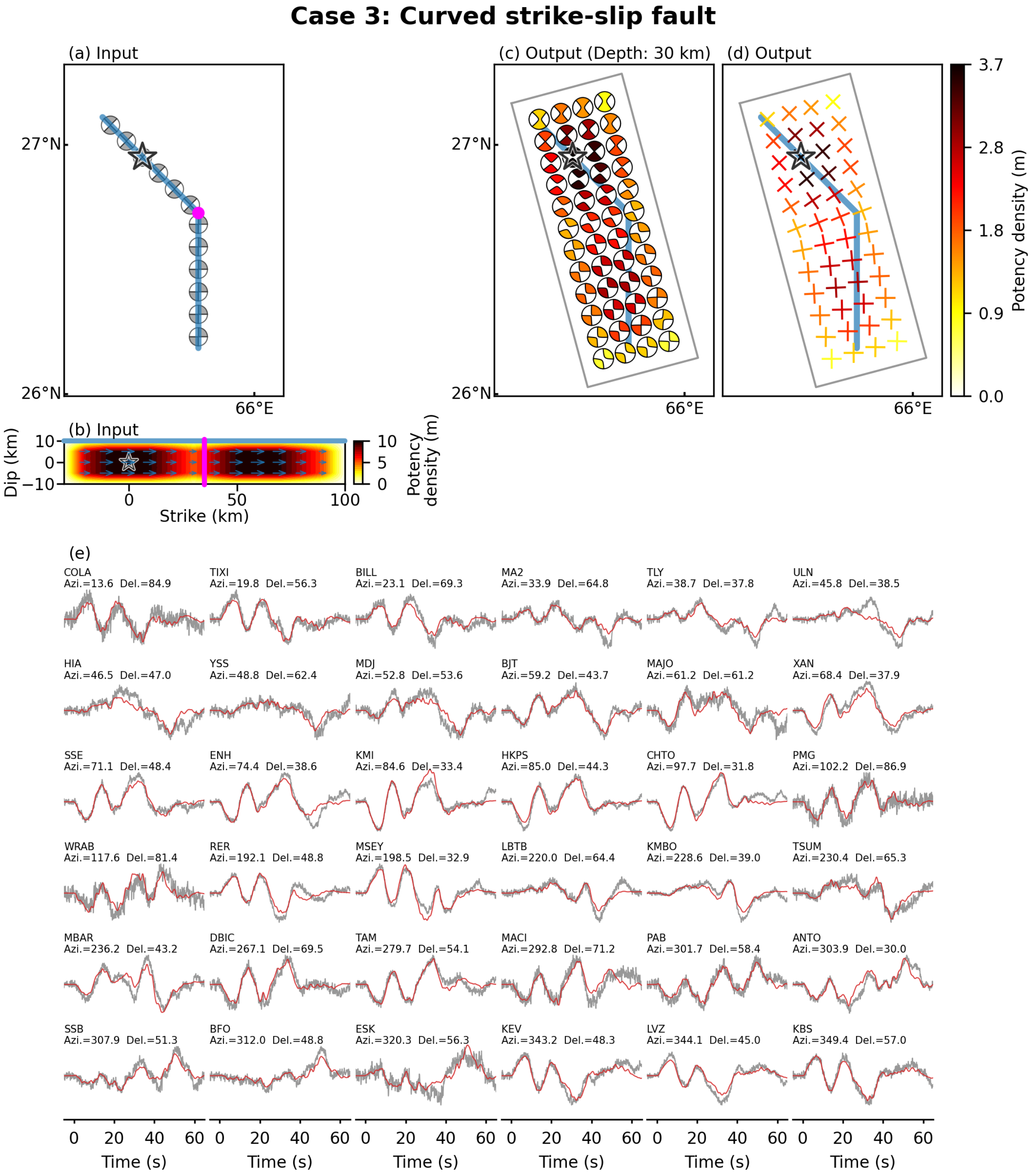

Figure 2.6: *Caption next page.*

Figure 2.6: (a) Fault geometry and focal mechanisms of the input source model, (b) distribution of potency density and slip angles of the input source model, (c) output source model, (d) distribution of strike angles extracted from the output source model, and (e) waveform fitting at all stations between input and output synthetic waveforms in the case 3. (a) The blue line represents the top of the input fault plane. The star denotes the epicenter. The pink circle denotes the point where strike angle of the fault changes. Beach balls show assumed focal mechanisms. (b) The blue arrow denotes the slip vector, and its length is related to the amount of potency density. The star denotes the initial rupture point. The pink line represents the boundary where strike angle of the fault changes. Color shows the potency density. (c, d) Color shows the potency density. The star denotes the epicenter. The gray line outlines the horizontally assumed model plane. The blue line represents the top of a fault plane of the input source model. The small beach ball, shown in (c), shows the focal mechanism at each subfault, plotted using a lower-hemisphere projection. Direction of the bar shown in (d) corresponds to the strike angle extracted from the focal mechanism shown in (c). (e) Gray and red traces represent the input and output waveforms. Station code, azimuth, and epicentral distance of each station are shown above the traces.

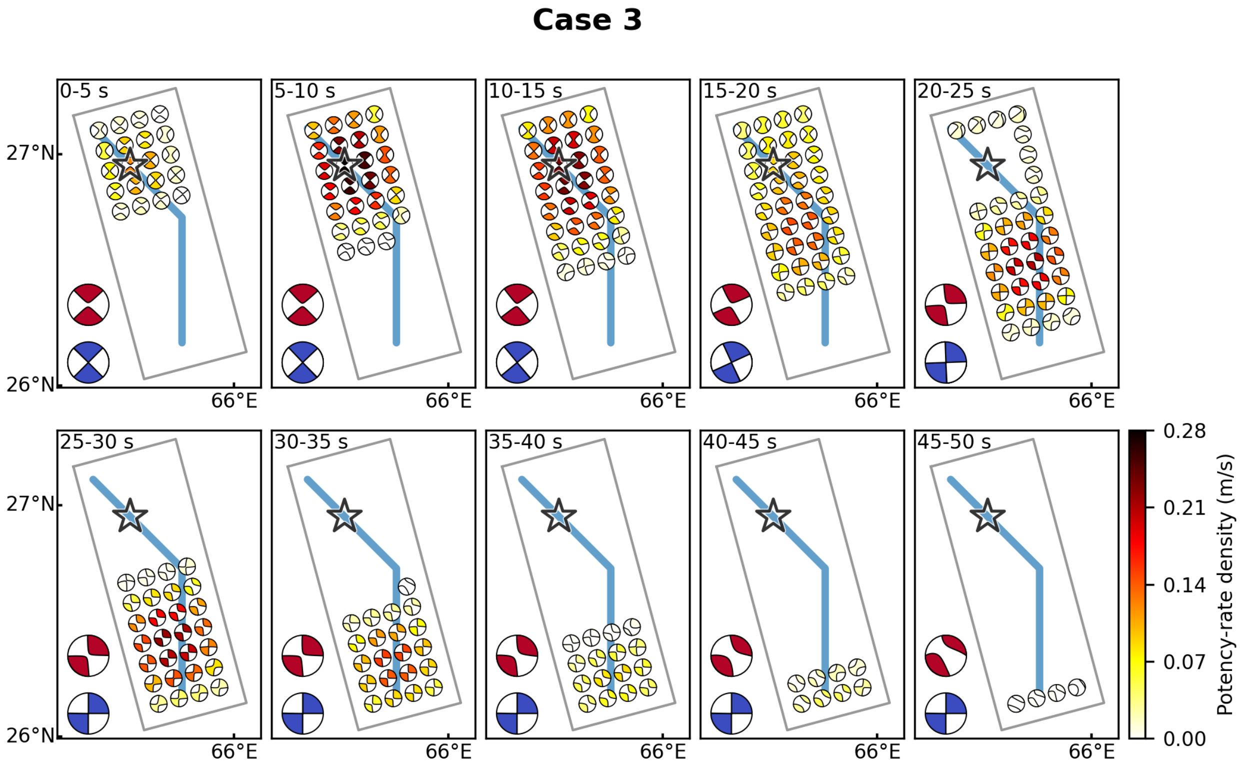

Figure 2.7: Snapshots of output source model in the case 3. Color of small beach ball represents the potency rate density. The star denotes the epicenter. The gray line outlines the horizontally assumed model plane. The blue line represents the top of a fault plane of the input source model. The small beach ball shows the potency density tensor at each subfault, plotted using a lower-hemisphere projection. The large blue and red beach balls are the centroid potency density tensor obtained by integrating potency rate density function in space and time at each time window for the input and output source models, respectively.

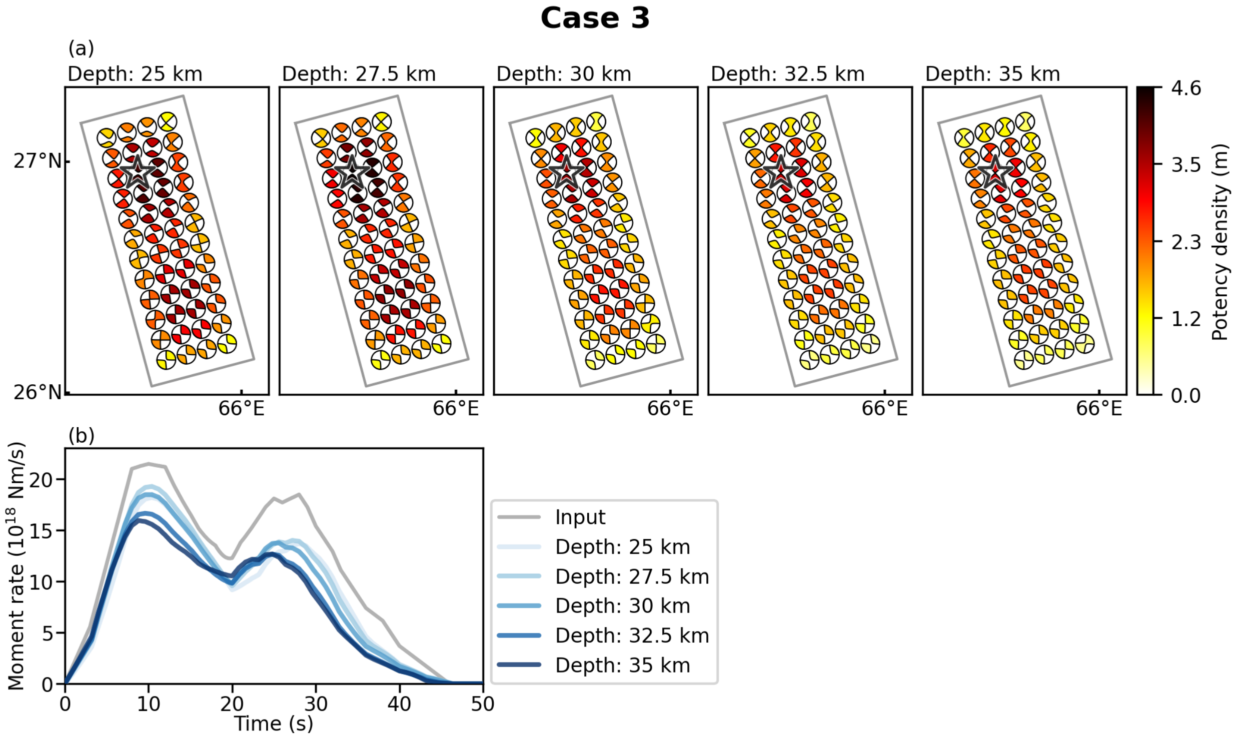

Figure 2.8: (a) Output source models with different source depths and (b) their moment rate functions in the case 3. (a) The small beach ball shows the focal mechanism at each subfault, and its color represents the potency rate density. The star denotes the epicenter. The gray line outlines the horizontally assumed model fault plane. Focal mechanisms are plotted using a lower-hemisphere projection.

In the case 3, we further evaluated a sensitivity to an assumption of the depth of the horizontal model plane, ranging between 25 km and 35 km every 2.5 km. The obtained potency density tensor distributions at variable model plane depths showed a similar pattern of focal mechanisms (Fig. 2.8a) and suggest that the change of initial rupture depths does not significantly affect a resultant potency density tensor distribution, although deeper source model shows smaller intensity of overall potency density due to relatively high amplitude of Green's function with deeper source depth. We can recognize that an arrival time of peaks in the source-time function is shifted in time within 1.6 s according to the model plane depth, which is explained by travel time difference expected from the difference in depth (Fig. 2.8b). The peak of the moment rate at around 10 s in the output source-time function is at most 26 % smaller than that of the input one, which is originated from the difference of depth range between the input and output rupture extent. However, the relative amplitudes and the number of moment rate peaks in the source-time functions of all output source models are similar to those of the input source model (Fig. 2.8b).

2.3 Application to real waveforms

2.3.1 The 2013 Balochistan earthquake

We applied the method developed in this study to teleseismic waveforms of the 2013 Balochistan, Pakistan, earthquake to test the formulation. The epicenter (26.951°N, 65.501°E), determined by the U.S. Geological Survey, National Earthquake Information Center (USGS NEIC; https://earthquake.usgs.gov/earthquakes/eventpage/usb000jyiv) was located in the east of the Makran accretionary wedge in the south-western Pakistan. In the eastern part of the Makran accretionary wedge, the Arabia plate subducts under the Eurasia plate at a rate of ~40 mm/yr in the southern part of Makran accretionary wedge and the eastern side of the Makran accretionary wedge adjoins the India plate northwardly converging towards the Eurasia plate at a rate of ~40 mm/yr (DeMets *et al.*, 2010) (Fig. 2.9a). According to observed surface rupture distribution (Zinke *et al.*, 2014) and analyses of optical satellite images (Avouac *et al.*, 2014; Jolivet *et al.*, 2014; Zinke *et al.*, 2014) and of interferometric synthetic aperture radar (InSAR) data (Barnhart *et al.*, 2014), the Balochistan earthquake shows a curved surface rupture pattern, which is similar to the arcuate topographic features around the epicenter. The global centroid moment tensor (GCMT; http://www.globalcmt.org/CMTsearch.html) solution and the W-phase moment tensor solution estimated by USGS (https://earthquake.usgs.gov/earthquakes/eventpage/usb000jyiv) suggest that the Balochistan earthquake was a left-lateral strike-slip earthquake (Fig. 2.9c). Studies of back-projection technique resolved spatiotemporal distributions of high-frequency radiation sources showing mostly unilateral rupture propagation towards the south-west from the epicenter (Avouac *et al.*, 2014; Wang *et al.*, 2016). Finite-fault modeling studies proposed source models with curved fault geometry which was represented by multiple rectangles (Avouac *et al.*, 2014) or a non-planar surface (Jolivet *et al.*, 2014). As mentioned in the General Introduction, such the possibly curved and geometrically complex fault of the Balochistan earthquake could prevent us from constructing a reliable source model because an inappropriate and a simplified assumption of fault geometry can yield significant modeling errors. In fact, the Balochistan earthquake is a case in which an assumption of simplified single planar fault largely distorts inversion solution (unrealistic estimate of rupture propagation direction). For example, Japan Meteorological Agency provisionally constructed a finite-fault model with teleseismic waveforms by using a single flat fault (https://www.data.jma.go.jp/svd/eqev/data/world/20130924/sr201309242029.pdf), and the source model suggested the north-eastward rupture

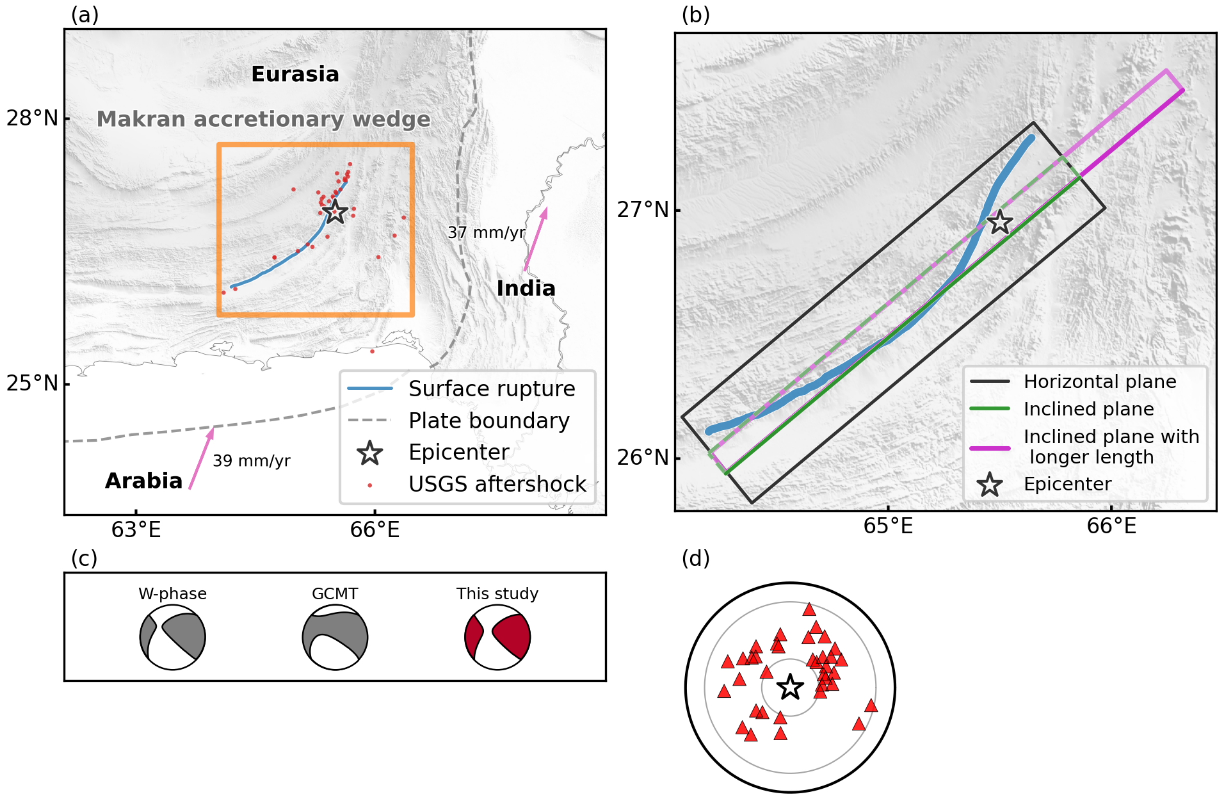

Figure 2.9: Tectonic setting and the observed surface rupture trace of the 2013 Balochistan earthquake, the model plane settings, and the moment tensor solutions from USGS NEIC, GCMT, and this study. (a) Blue line represents the surface rupture trace derived from Zinke *et al.* (2014). Aftershocks with $M_W \geq 3$ occurring within 1 week of the mainshock (USGS NEIC; https://earthquake.usgs.gov/earthquakes) are plotted as red dots. Pink arrows represent the relative motions of the Arabia and India plates against the Eurasia plate from the UNAVCO (https://www.unavco.org) plate motion calculator following the MORVEL model (DeMets *et al.*, 2010). The orange rectangle outlines the area shown in Fig. 2.9(b). Topography was drawn by using 2010 Global Multi-resolution Terrain Elevation Data 7.5 arcsecond median elevations (GMTED; https://topotools.cr.usgs.gov/gmted_viewer/) (Danielson & Gesch, 2011) and the shadows were drawn with the light coming from a 45° azimuthal direction. (b) Model planes used in this study. The top of each model fault plane is shown by a bold line, and the light-colored lines outline the inclined model planes. The star denotes the epicenter. The blue line represents the trace of surface rupture measured by Zinke *et al.* (2014). (c) Moment tensor solutions. The gray beach balls show the *W*-phase CMT solution estimated by USGS (https://earthquake.usgs.gov/earthquakes/eventpage/usb000jyiv/moment-tensor) and the GCMT solution from the Global CMT Catalog Search (http://www.globalcmt.org/CMTsearch.html). The red beach ball represents the total moment tensor estimated by using a horizontal model plane in this study. (d) Station Distribution (red triangles) around the epicenter (star) in an azimuthal equidistant projection. The circles show the teleseismic distances at 30° and 90°.

propagation that is inconsistent with results of back-projection analyses and observational data (e.g. Wang *et al.*, 2016; Avouac *et al.*, 2014; Zinke *et al.*, 2014) and would be originated from modeling error of fault geometry. In Section 2.4.3, we demonstrate the unrealistic source image originated from modeling error of fault geometry and discuss it further. Thus, the 2013 Balochistan earthquake is a suitable case for testing the fault geometry resolvability of the new finite-fault inversion framework developed in this study and for showing its insensitivity to modeling errors of fault geometry.

2.3.2 Data processing and model setting

We downloaded the waveform data from the Incorporated Research Institutions for Seismology Data Management Center (IRIS-DMC). 36 vertical components of globally observed teleseismic P waveforms were selected based on a view point of a high signal-to-noise ratio and a good azimuthal coverage (Fig. 2.9d). We manually determined the first motion of the teleseismic P waveforms, deconvolved the instrumental response from the original waveforms to convert into velocity waveforms, and then resampled the waveform data at a 0.8 s sampling interval. Following the method of Kikuchi & Kanamori (1991), we calculated theoretical Green's functions at a 0.1 s interval, and the attenuation time constant t^* for the P wave was set to 1.0 s. We used the one-dimensional layered velocity structure model around the source region (Table 2.1) adopted by Avouac *et al.* (2014) to calculate the theoretical Green's functions. We do not apply any filter to either the observed waveforms or the theoretical Green's functions to extract detailed information of rupture process possibly recorded in the high-frequency components of the seismic records. Since our new inversion method makes it possible to estimate spatiotemporal potency density tensor distribution whose focal parameters are independent of the strike and dip angles of the assumed model fault plane, which was described in Section 2.1, we embedded the model fault plane horizontally at a certain depth. We set a single model fault plane striking 230° and dipping 0° with a length of 200 km and a width of 45 km wide (Fig. 2.9b) that horizontally covered the entire surface rupture area inferred by Zinke *et al.* (2014). As the depth of the model fault plane, we took 7.5 km hypocentral depth that minimized the ABIC value among different hypocentral depth configurations. The model plane was expanded into bilinear B-spline functions with an interval of 5 km and adopted the epicenter for the initial rupture point. The potency rate density function at each source knot was represented by a linear

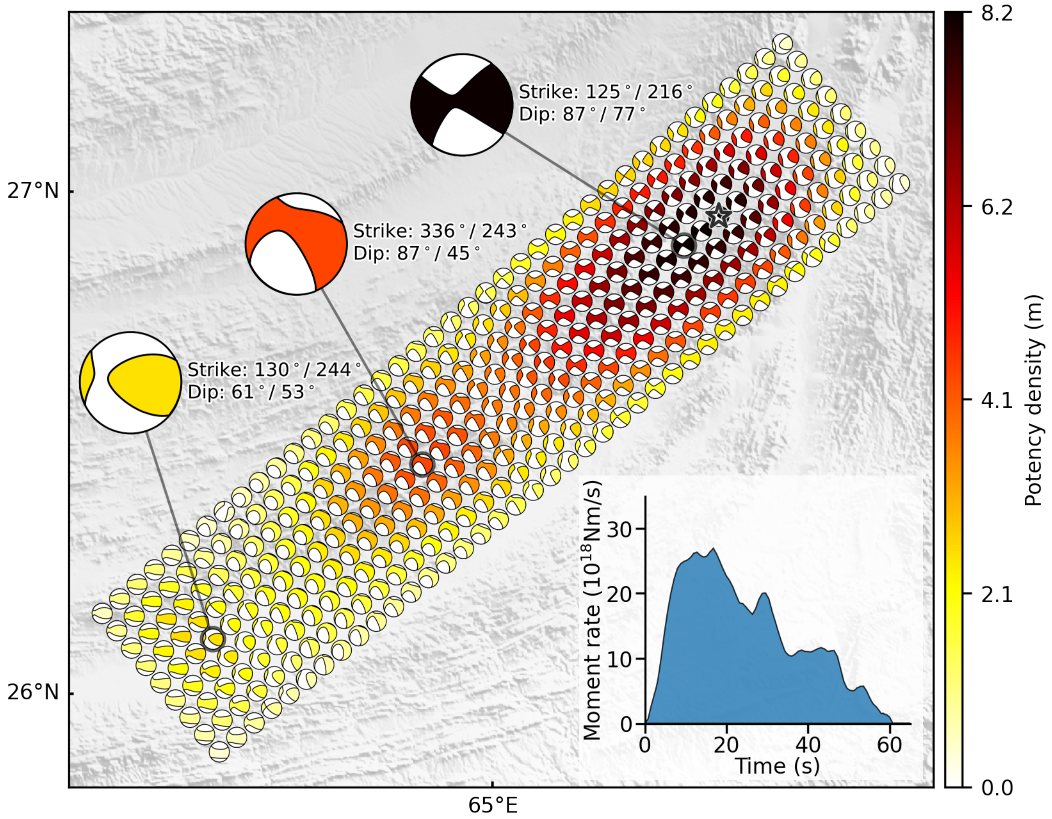

Figure 2.10: Spatial distribution of potency density tensors and source-time function (inset). The small beach ball shows the focal mechanism at each subfault, plotted using a lower-hemisphere projection. The star denotes the epicenter. The beach ball color shows the potency density. Several beach balls (black outlines) were selected and magnified to emphasize the spatial variation of the focal mechanism. The strike and dip angles are shown on the right side of the enlarged beach ball.

combination of B-spline functions with a temporal interval of 0.8 s and a duration of 31 s so as to flexibly represent variation of rupture behaviours. We also assumed a total source duration of 60 s on the basis of source-time functions estimated by previous finite-fault studies (Avouac *et al.*, 2014; Barnhart *et al.*, 2014). The maximum rupture-front velocity was set as 4 km/s that takes into account the possibility of supershear rupture reported by Avouac *et al.* (2014).

2.3.3 Results

Integrating potency rate density function for each basis double-couple component at each subfault in time, we obtained the spatial distribution of potency density tensors on the model fault plane (Fig. 2.10). The CLVD component of potency density tensor at each subfault is not clearly significant (Fig. 2.10), which suggests that teleseismic P waveforms are useful to constrain a CLVD component of a shallow strike-slip earthquake under the condition of a good azimuthal coverage of station distribution. In this study, the potency density at each subfault is represented as an average of absolute value of eigenvalues for T- and P- axes of a diagonalized potency density tensor at each subfault. As shown in Fig. 2.10, large potency density area is distributed around the epicenter and extends to south-west from the epicenter about 150 km. Obtained potency density tensor has two set of fault parameters (i.e. strike, dip and rake angles) and our method can not uniquely choose a set of fault parameters alone. In order to simply describe the variation of potency density tensors, we take the fault plane whose strike was in the range between 180° and 270° based on the mapping of the surface rupture (e.g. Zinke *et al.*, 2014) and hereafter describe about a nodal plane of each potency density tensor close to the fault plane. The spatial distribution of potency density tensor shows that strike-slip faulting is dominated throughout the model space, and a potency density tensor estimated around the epicenter shows strike-slip faulting with a strike of 216° and a dip of 77° (Fig. 2.10). Around 80 km south-west from the epicenter, strike-slip faulting with a strike of 243° and a dip of 45° was estimated, and around 140 km south-west from the epicenter, a potency density tensor with a reverse or oblique-slip faulting with a strike of 244° and a dip of 53° was estimated (Fig. 2.10). Integrating the spatial distribution of potency density tensors shown in Fig. 2.10, we obtained a total moment tensor. The total moment tensor shows a strike-slip faulting with a strike of 226° and a dip of 61° and includes 8% of the non-double-couple components (Fig. 2.9c). The total released seismic moment was 7.53×10^{20} Nm (M_W 7.8) that is comparable to the GCMT solution of 5.59×10^{20} Nm (M_W 7.8). The source-time function, obtained by calculating the seismic moment at each time step, has a major peak at around 17 s and three minor peaks at around 29 s, 43 s and 53 s (Fig. 2.10).

In order to make the spatiotemporal variation of focal mechanisms recognizable, we showed a potency density tensor in 10-s time window on its centroid location by integrating the potency rate density in space and time along the model plane (Fig. 2.11). The centroid locations and the potency density tensors show that the centroid location migrates unilaterally towards the south-west from the epicenter, and migration distances from 20 to 50 s is longer than those before 20 s and after 50 s. We can see a successive transition of the potency density tensor in each time window from strike-slip faulting with a strike of 205° and dip of 68° to oblique-slip faulting with a strike of 241° and a dip of 39° during 0 to 60 s, indicating a clockwise rotation of the strike orientation from north to south (Fig. 2.11). We can also see this temporal transition of the focal mechanism in the static, spatial variation of the distribution of potency density tensors

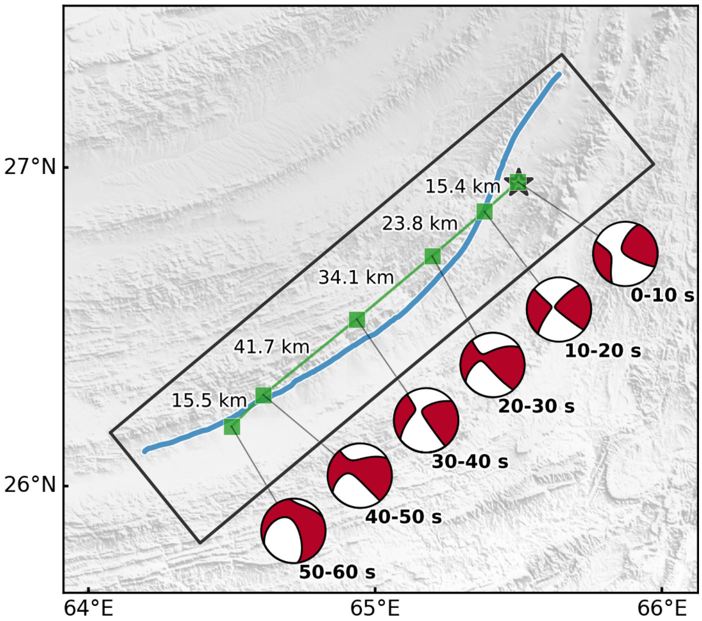

Figure 2.11: Centroid potency density tensors during the rupture evolution. The centroid locations of the potency rate density (green squares) and its potency density tensor (red beach ball) is shown at each time window. The distance between the adjacent centroid locations and the corresponding time window for the centroid location are shown. The blue line represents the trace of surface rupture measured by Zinke *et al.* (2014). The black rectangle outlines the horizontal model plane. The star denotes the epicenter.

(Fig. 2.10).

In order to further visualize the variation of focal mechanism during rupture evolution at all subfaults, we calculated a potency density tensor by temporally integrating the potency rate density function in each time window at each subfault and then plotted their stike and dip angles within a strike angle range between 180° and 270° (Fig. 2.12a). The histogram snapshots (Fig. 2.12a) shows a successive transition of strike angle from 200° to 240° during 0 to 50 s, which means the clockwise rotation of fault plane during rupture propagation. Focusing on dip angles, we can see temporal variation of dip angles, showing steep, around 80°, during 0 to 20 s, and shallow, around 60°, during 20 to 50 s. While the centroid location migrates fast from 20 s to 50 s (Fig. 2.11), the dip angles seems more scattered than those during 0 to 20 s. In the last time window, The distributions of strike angle and dip angle seems scattered, but shows a small peak of dip angle around 40°. We also plotted the strike and dip angles of the two fault plane of potency density tensor at all subfaults for all time windows without any range of strike angles (Fig. 2.12b). We can see two modes of strike angle at around 130° and 230° (Fig. 2.12b) that can be consisdered to represent the two conjugated fault planes.

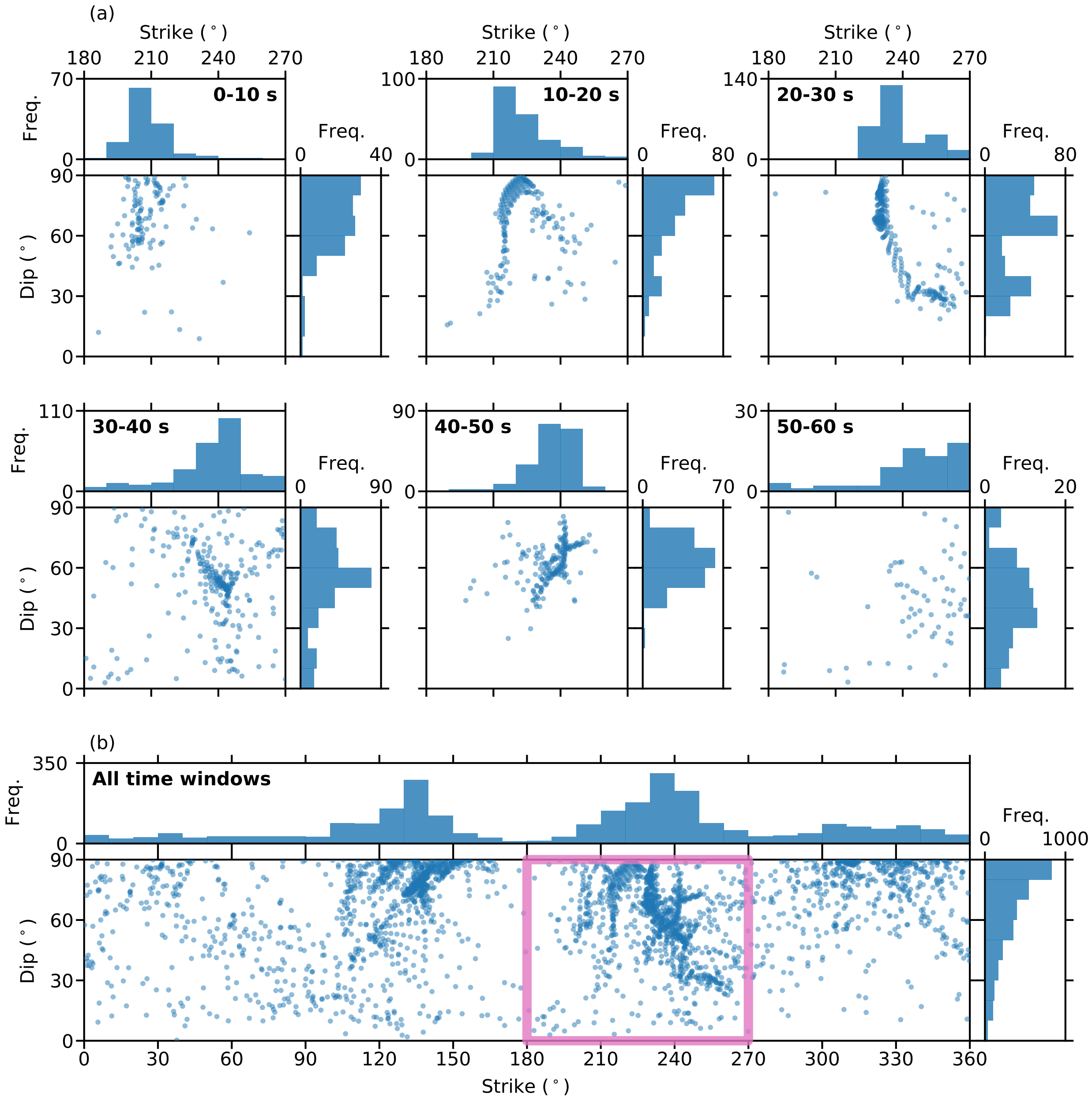

Figure 2.12: Strike and dip angles at all subfaults in (a) each time window and (b) all time windows every 10° bin. The range of strike and dip angles in (a) is denoted by the pink rectangle in (b).

2.4 Discussion

2.4.1 Rupture propagation and fault geometry of the 2013 Balochistan earthquake

We estimated unilateral rupture propagation towards the south-west from the epicenter (Fig. 2.11), which is consistent with the spatiotemporal distribution of high-frequency radiation sources tracked by the back-projection analyses (Avouac *et al.*, 2014; Wang *et al.*, 2016). During 20 to 50 s, the estimated migration velocity of average centroid location was 3.8 km/s (Fig. 2.11) which exceeds the near source shear-wave velocity at the hypocentral depth of the model fault plane we set (Table. 2.1). Regarding the centroid location migration velocity as a rupture velocity and comparing it directly with rupture front velocity inferred by the back-projection analyses (Avouac *et al.*, 2014; Wang *et al.*, 2016) are principally impossible, but the period from 20 to 50 s when the centroid migration speed exceeds the shear-wave velocity well matches the period when a rupture velocity exceeded the local shear-wave velocity reported by Avouac *et al.* (2014).

The trace of surface rupture measured by Zinke *et al.* (2014) has a strike orientation of 200° around the epicenter, 230° around 80 km south-west of the epicenter, and 240° around 140 km south-west of the epicenter. These strike orientations of surface rupture trace are consistent with the strike angles of the static potency density tensor distribution (Fig. 2.10) and spatiotemporal transition pattern of strike angle of potency density tensor every 10 s during rupture evolution (Fig. 2.11). As can be seen in Fig. 2.10, we estimated relatively shallow dipping fault rupture in the south-western part of the source area, showing 45° dip angle around 80 km south-west from the epicenter and 53° dip angle around 140 km south-west from the epicenter. We also estimated the shallow dip angle in the temporal evolution (Figs 2.11 and 2.12), showing 39° dip angle of centroid potency density tensor during 50–60 s in Fig. 2.11 and relatively high peak of dip angle around 40° in Fig. 2.12. It has been shown that the Makran accretionary wedge accommodates thrust fault (Haghipour *et al.*, 2012), and it can be considered that the estiamted shallow dipping fault represents the thrust fault the Balochistan earthquake ruptured.

We performed the synthetic test in which the source model of the 2013 Balochistan earthquake is adopted as an input model and then evaluated the robustness of the obtained results (Figs 2.13a, b and 2.14). The results show that our new method can reproduce the variation of potency density tensors including the clockwise rotation of strike orientation of strike-slip faulting during the rupture propagation toward the south-west from the epicenter (Figs 2.13c and d), suggesting the rupture propagation along the curved fault. This result suggests that our estimation of the focal mechanism change along with the rupture propagation in the real application is robust.

These results prove that the new inversion method enables us to estimate the direction of rupture propagation and the curved pattern of fault geometry which are consistent with the back-projection analysis and optical satellite images, even by simply assuming model space as the single horizontal plane. This would be attributable to the the relatively narrow depth range of rupture extent of the Balochistan earthquake, shallower than 15 km shown by (e.g. Avouac *et al.*, 2014; Barnhart *et al.*, 2014). Another factor of our estimated realistic results is that the uncertainty of Green's function is taken into account in our new method, and we verified it by applying a method that is the same as our new method but neglecting uncertainty in Green's function (Fig. 2.15). The obtained source model shows that the estimated strike angles of potency density tensors are inconsistent with the strike orientation around both the north-east and the south-west ends of the surface rupture trace measured by Zinke *et al.* (2014) (Fig. 2.15). Thus, introducing uncertainty of Green's function is indispensable to the stable estimation of potency density tensor distribution. However, for an earthquake with a wide rupture extent in depth, such as a subduction zone earthquake, Green's function should be more variable and hence it is better to adopt a inclined model plane for calculating depth varying Green's function.

2.4.2 Sensitivity to a model plane geometry

In Section 2.1, we assumed that Green's function of teleseismic body wave is insensitive to a slight change of source location (eq. 2.3), which neglects modeling errors originated from uncertainty of the space configuration, and then represented the potency density tensor distribution in a simple two-dimensional model space in Sections 2.2 and 2.3. Here, we applied the new method with a use of a different geometry of model space and then evaluated the effects of the assumption of Green's function in eq. (2.3).

As a model space geometry different from the one used in Section 2.3, we adopted an inclined plane with a length of 200 km, a width of 25 km, and a dip of 64° which is an average dip angle of model planes of finite-fault source model constructed by USGS NEIC

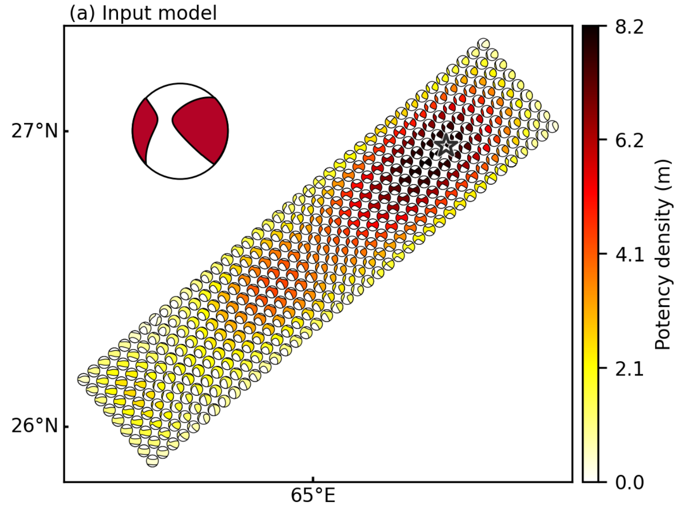
(a) Input model

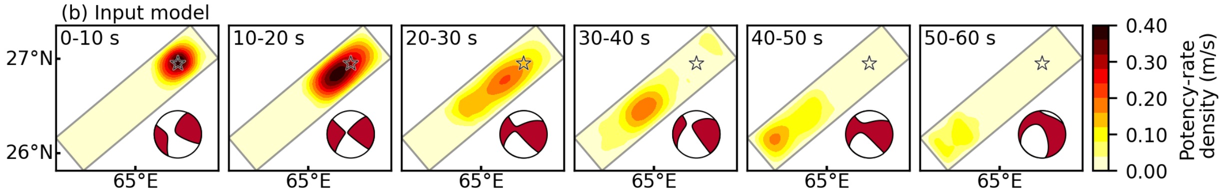
(b) Input model

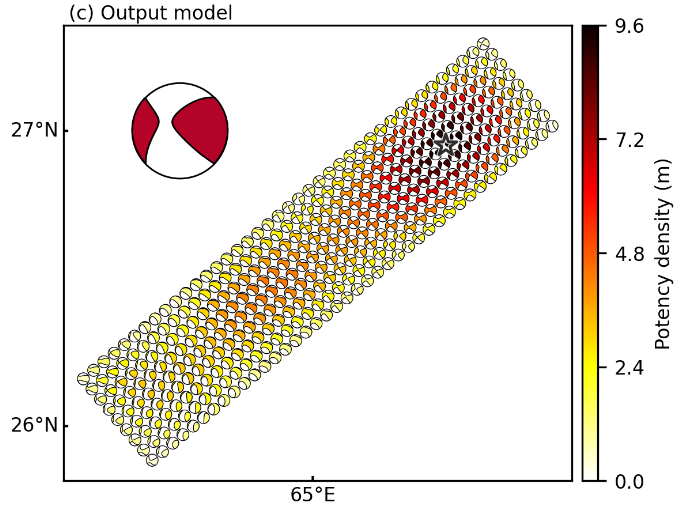
(c) Output model

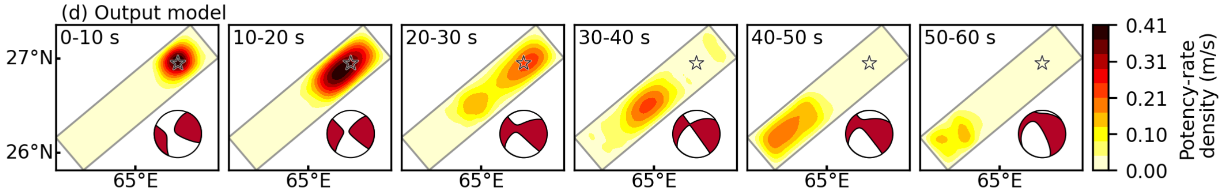
(d) Output model

Figure 2.13: (a, b) Input and (c, d) output source model in the synthetic test for evaluation of our result. (a, c) The small beach ball color shows the potency density. The star denotes the epicenter. The large red beach ball represents the total moment tensor obtained by integrating the potency density tensors in space. (b, d) Color shows the potency rate density. The gray line outlines the model plane. The star denotes the epicenter. The large red beach ball represents the centroid potency density tensor at each time window.

Figure 2.14: Potency rate density functions of input (our result) and output (reproduced) source models at all subfaults in the synthetic test for evaluation of our result. Gray and red traces correspond to input (our result) and output (reproduced) models, respectively. The cell outlined by yellow line represents the initially ruptured subfault.

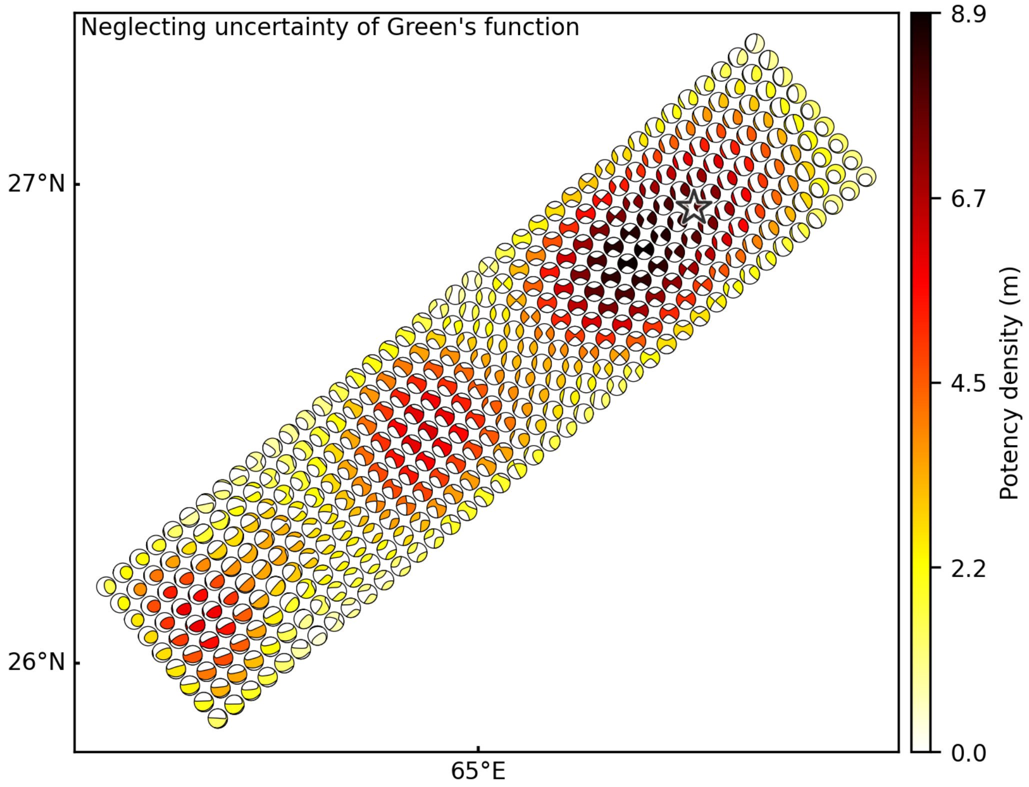

Figure 2.15: Spatial distribution of the potency density tensors obtained by using the formulation that neglects uncertainty of Green's function. The small beach ball shows the focal mechanism at each source knot, plotted using a lower-hemisphere projection. The star denotes the epicenter. The beach ball color shows the potency density.

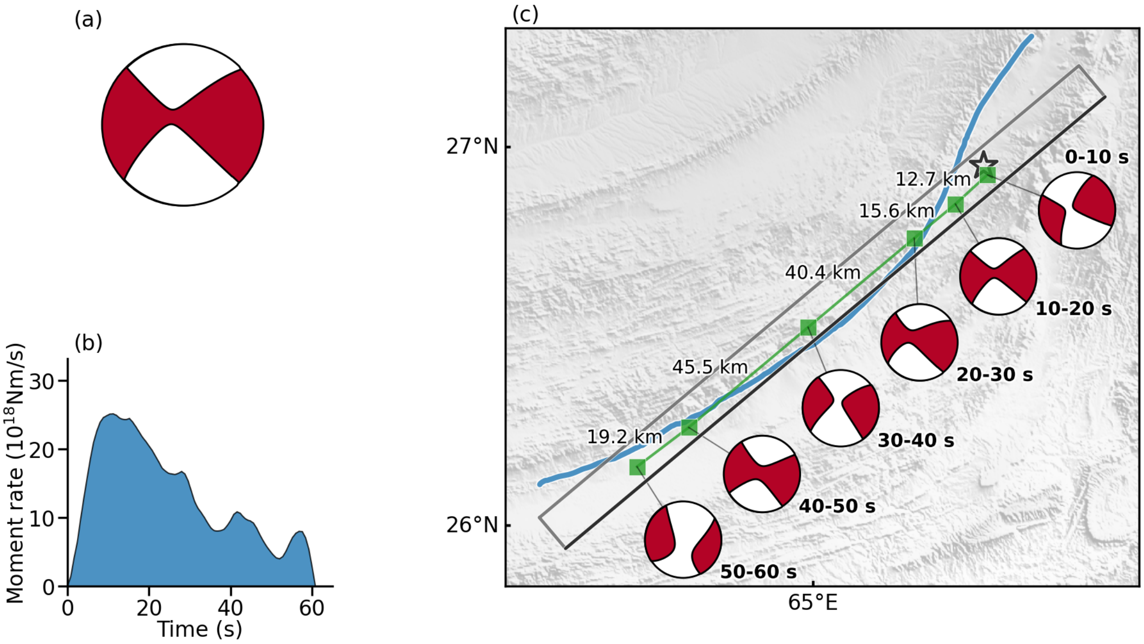

Figure 2.16: (a) Total moment tensor, (b) source-time function, and (c) the centroid potency density tensors during rupture evolution obtained by using the inclined model plane. The star denotes the epicenter. The gray line outlines the model fault plane, and the black line shows the top of the model fault plane, respectively. The green squares and beach balls represent the centroid location and the centroid potency density tensor at each time window, respectively. Time windows and the distance between adjacent centroid locations for the centroid location are shown.

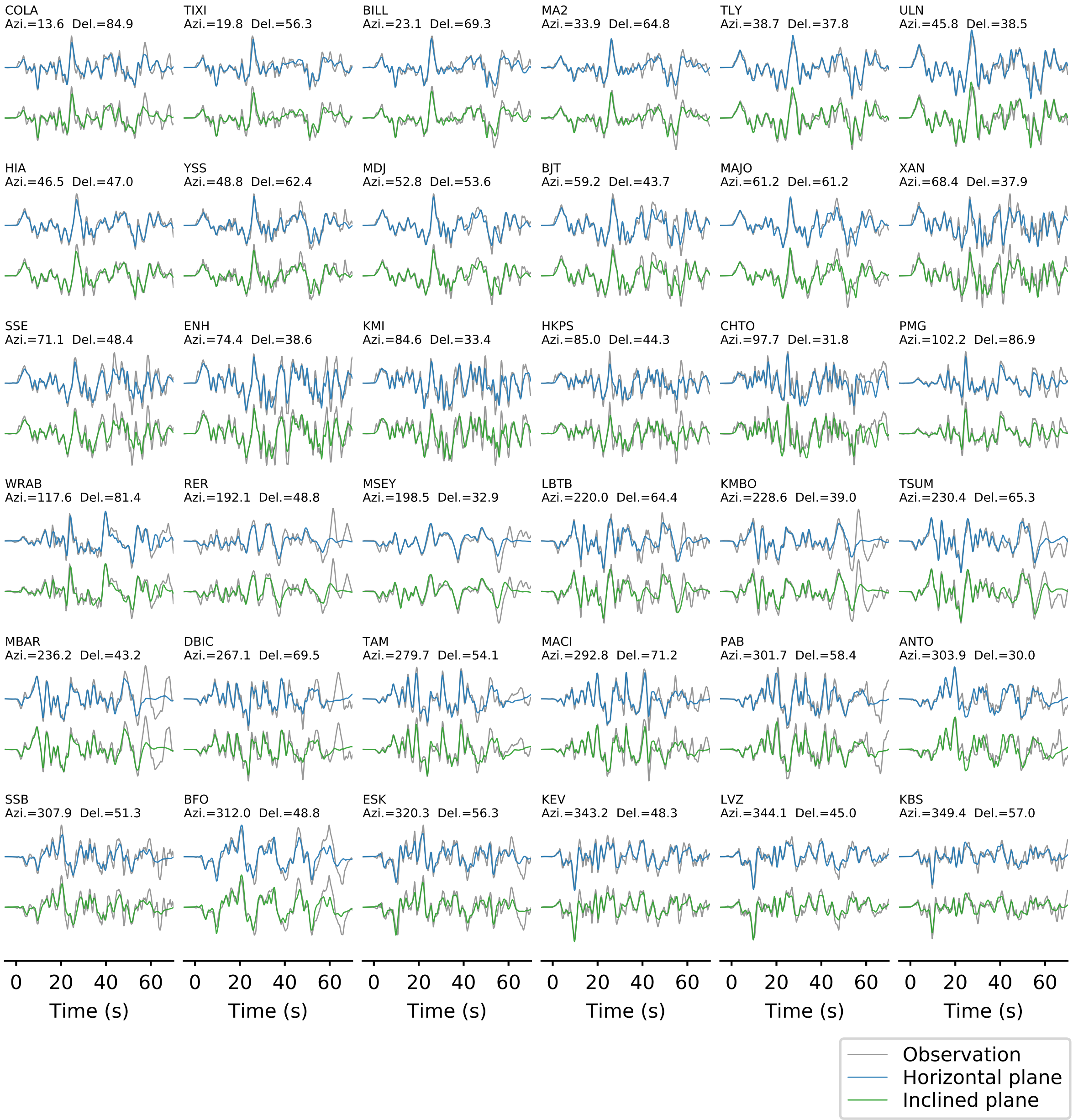

Figure 2.17: Waveform fitting between observed (top gray line) and synthetic waveforms for the analyses using the horizontal model plane (middle blue line) and inclined model plane (bottom green line). Station code, azimuth, and epicentral distance at each station are shown above the traces.

(https://earthquake.usgs.gov/earthquakes/eventpage/usb000jyiv) (Fig. 2.9b). The other model parameters, such as a temporal interval and a duration of potency rate density function, are the same as in Section 2.3.

The obtained total moment tensor indicates strike-slip faulting, and the more realistic fault plane has a strike of 226° and a dip of 77° (Fig. 2.16a), which shows a steeper dip angle than that of the total moment tensor obtained by using a horizontal model plane in Section 2.3 (Fig. 2.9c). The total released seismic moment was 7.00×10^{20} Nm (M_{W} 7.8), which is close to the one obtained in the analysis adopting a horizontal model plane in Section 2.3. In the source-time function (Fig. 2.16b), we can recognize a large peak around 11 s and three smaller peaks around 28 s, 42 s, and 57 s. Comparison with the source-time function obtained by using the horizontal model plane (Fig. 2.10) indicates that the timings of the peaks of the source-time function are earlier in time in the range of 1–5 s. This is explainable by the travel time difference originated from the model space difference, which means that the source model with deeper extent allows earlier start of rupture and we reproduced it in the synthetic test case 3 (Fig. 2.8b). However, the number and relative amplitudes of the peaks are similar with the one obtained by adopting horizontal model plane (Fig. 2.10). Focusing on the centroid potency density tensors at every 10 s (Fig. 2.16) during 0 to 30 s, we can see the similar transition pattern of focal mechanism to the one obtained by adopting the horizontal model plane (Fig. 2.11), showing the strike-slip mechanism and the clockwise rotation of strike orientation during the rupture propagation towards the south-west from the epicenter, and the rotation of the strike orientation continued until 50 s. The average speed of centroid location migration during 20 to 50 s reaches to 4.3 km/s (Fig. 2.16) which is close to the one in the previous result (Fig. 2.11).

We can recognize a similar pattern of potency density tensor distributions between the inclined model plane and the horizontal model plane analyses, showing the clockwise rotation of strike angle during the unilateral rupture propagation towards south-west from the epicenter. However, the inclined plane model yielded the potency density tensors having steeper dip angle during 30 to 60 s (Fig. 2.16c) and the discrepancy of dip angle becomes larger as the rupture evolves. Here, we defined the variance to quantify the waveform fit:

$$Variance = \frac{\sum_{j}\sum_{t}\left(u_j^{obs}(t) - u_j^{syn}(t)\right)^2}{\sum_{j}\sum_{t} u_j^{obs}(t)^2}, \tag{2.17}$$

where u_j^{obs} and u_j^{syn} represent observed and synthetic waveforms obtained by the inversion analysis at the jth station at time t. The degree of fitting between the observed and synthetic waveforms is quite similar between the two analyses (Fig. 2.17), but the variance (eq. 2.17) is 0.04 larger, meaning worse fit, in the analysis using the inclined model plane. The dip angle of the model plane prescribes the spatial source location, and the horizontal model plane more broadly covers the possible rupture extent than the inclined model plane (Fig. 2.9b). The horizontal model plane with the larger coverage may be less suffered from the possible error of model space assumption in the analysis of the Balochistan earthquake.

2.4.3 Bias due to limited flexibility of slip direction

In this Subsection, we show that modeling errors of fault geometry can significantly distort the solution of conventional inversion methods that limit the estimated slip direction (Fig. 2.1b) and that our new method is robust to the modeling errors of fault geometry. We applied the conventional method to the Balochistan earthquake and adopted a single model plane with a length of 260 km, which is 60 km longer in the north-east direction than the model planes used in Section 2.3 and Subsection 2.4.2, and a width of 25 km, a strike of 230°, and a dip of 64° (Fig. 2.9b). As the conventional method, we employed the formulation of Yagi & Fukahata (2011a) that introduces uncertainty of Green's functions into the data covariance matrix, which is the fundamental framework of our new method, but adopts only the two basis double-couple components to represent fault slip (Fig. 2.1b).

The resultant seismic moment obtained by the conventional inversion scheme was 7.27×10^{20} Nm (M_W 7.8), which is comparable to that obtained by new our method (6.43×10^{20} Nm, M_W 7.8). However, the conventional method estimated the opposite direction of rupture propagation to that of the new inversion schemes (Fig. 2.18). The potency density distribution estiamted by conventional method showed that the rupture unilaterally propagated toward north-east from the epicenter (Fig. 2.18b) and accordingly the main ruptured area are distributed in the area north-east of the epicenter (Fig. 2.18d), which is consistent with the source model with a single flat fault constructed by Japan Meteorological Agency (https://www.data.jma.go.jp/svd/eqev/data/world/20130924/sr201309242029.pdf) However, this north-eastward rupture propagation seems unrealistic because the studies of back-projection analysis estimated the south-westward rupture propagation from the epicenter (e.g. Avouac *et al.*, 2014; Wang *et al.*, 2016)

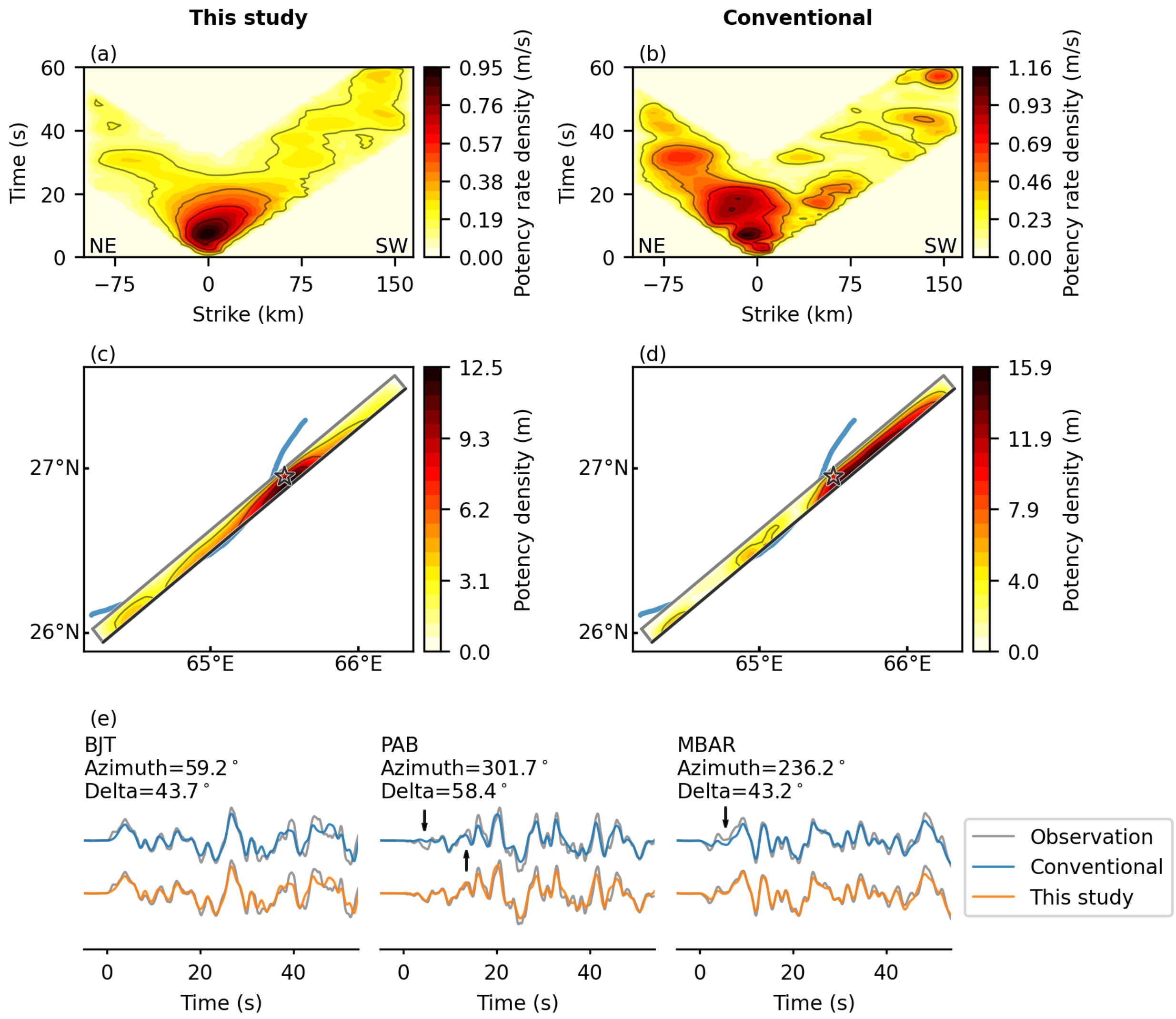

Figure 2.18: Comparison of source models between the formulation developed in this study and the one used by Yagi & Fukahata (2011a). (a, b) Time evolution of potency rate density along the strike direction and (c, d) potency density distribution obtained with the new and conventional method, respectively. The star denotes the epicenter. The gray line outlines the model plane, and the black line shows the top of the model plane. Contour intervals in (a), (b), (c) and (d) are 0.19 m/s, 0.23 m/s, 3.1 m and 4.0 m, respectively. (e) Waveform fitting comparison at selected stations between the new (orange) and the conventional (blue) method. The station code, azimuth, and epicentral distance are shown above the traces. Several phases where the observed waveform was not well reproduced by the conventional method are pointed out by arrows.

and the surface rupture is distributed mainly in the area south-west from the epicenter (e.g. Avouac *et al.*, 2014; Zinke *et al.*, 2014). While some phases of the observed waveforms were not well reproduced by the conventional inversion scheme at some stations (Fig. 2.18e), the variance of the waveform fittings obtained with the conventional method was only 0.04 larger than that obtained with our new method. Even though the difference of the variance between the two methods seems small, the conventional method limiting estimated slip direction could not reproduce the realistic rupture propagation direction independently inferred from observational data and other previous analyses. It can be said that even if we introduce the uncertainty in Green's functions into the covariance matrix, a simplified assumption of the fault geometry within a conventional inversion framework limiting slip direction may distort the solution (Fig. 2.18) and biase interpretations of the source process. In an actual case, when we have little information on fault geometry in an analysis immediately after an earthquake occurrence, we usually adopts a single and wide plane as a model space. However, this inappropriate assumption of fault geometry possibly yeilds an unrealistic source model distorted by modeling errors of fault geometry. Our new method makes it possible to mitigate such a problem, and to construct a realistic source model relatively quickly without detailed information about the fault geometry.

3. Development of an approach to construct fault geometry

The seismic waveform contains information on both rupture propagation and fault geometry underground. Finite-fault inversion of seismic waveforms has been widely used for resolving rupture propagation in detail along a model fault plane, but it had been generally difficult to constrain the fault geometry of an earthquake solely by using it because the inverse problem that should be solved becomes strongly nonlinear (Fukahata & Wright, 2008; Asano & Iwata, 2009). The finite-fault modeling developed in Chapter 2, named potency density tensor inversion, which introduces uncertainty of Green's functions into seismic source inversion Yagi & Fukahata (2011a) and adopts five basis double-couple components (Kikuchi & Kanamori, 1991) to represent fault slip, has made it possible to extract information on fault geometry as well as rupture propagation from teleseismic *P* waveforms. Taking into account the insensitivity of teleseismic *P*-wave Green's function to slight changes of absolute source location, the new inversion method enables us to infer the spatiotemporal distribution of potency density tensors, which are moment density tensors by divided by rigidity. Because spatiotemporal distribution of potency density tensor contain information on the direction of fault displacement, we can extract information on fault geometry (i.e. strike and dip angles) from seismic waveforms, which was proven by numerical simulations and an application to real teleseismic waveforms in Chapter 2.

While the the flexibility of the model space assumption in potency density tensor inversion, the locations of potency density tensors estimated on an assumed model fault surface can deviate from their true location, which means that the spatial distribution of the strike and dip angles of potency density tensors cannot directly be interpreted as the fault geometry. Moreover, as we described in Section 2.1, the estimated potency density cannot be directly interpreted as slip because the assumed model fault surface is not always identical to the real fault surface. It is

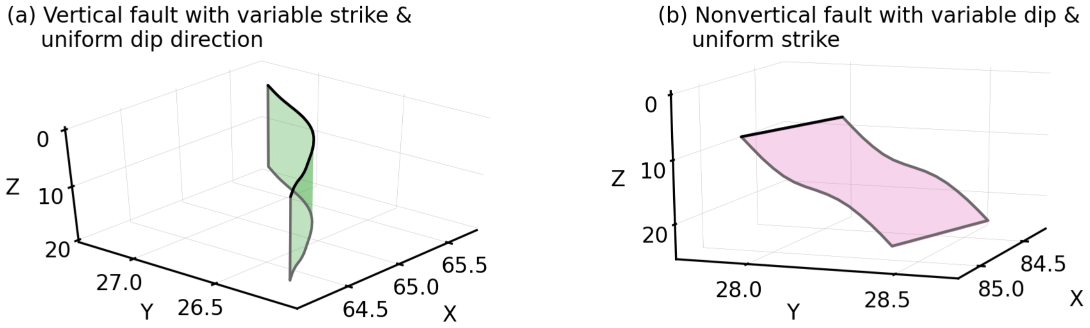

Figure 3.1: Schematic illustration of fault geometry constructed by our new method: (a) vertical fault with variable strike and uniform dip direction, and (b) nonvertical fault with variable dip and uniform strike. Colored non-planar surface outlined by gray line represents the fault. The top of fault plane is shown by a black line.

sometimes difficult to properly understand rupture propagation velocity and its relation to fault geometry without explicit representation of fault geometry. Thus, source models obtained by the potency density tensor inversion may not be interpreted in the same way as those obtained by conventional inversion methods, in which a shear slip direction is fixed on the assumed model fault surface.

Here, we propose a nonlinear inversion method to construct fault geometry from teleseismic *P* waveforms that uses the potency density tensor inversion to solve the spatial distribution of strike and dip angles on the assumed fault. By iteratively solving spatial distribution of potency density tensor and updating fault geometry step by step, it is possible to constrain a fault geometry that is consistent with the spatial distribution of strike and dip angles. An obtained source model, whose model fault geometry is constrained by inversion of seismic waveforms, provides us to better estimation of the relationship between rupture propagation and fault geometry without suffering from possible bias due to inappropriate assumption of fault geometry, which implies that the new method shows the way for flexible finite-fault modeling that extracts more information from data with fewer assumptions. This chapter presents the methodology of the new approach and our evaluation of the proposed method through the synthetic tests and real application of it to waveforms of the M_{W} 7.7 2013 Balochistan, Pakistan and the M_{W} 7.9 2015 Gorkha, Nepal, earthquakes involving geometrically complex fault systems.

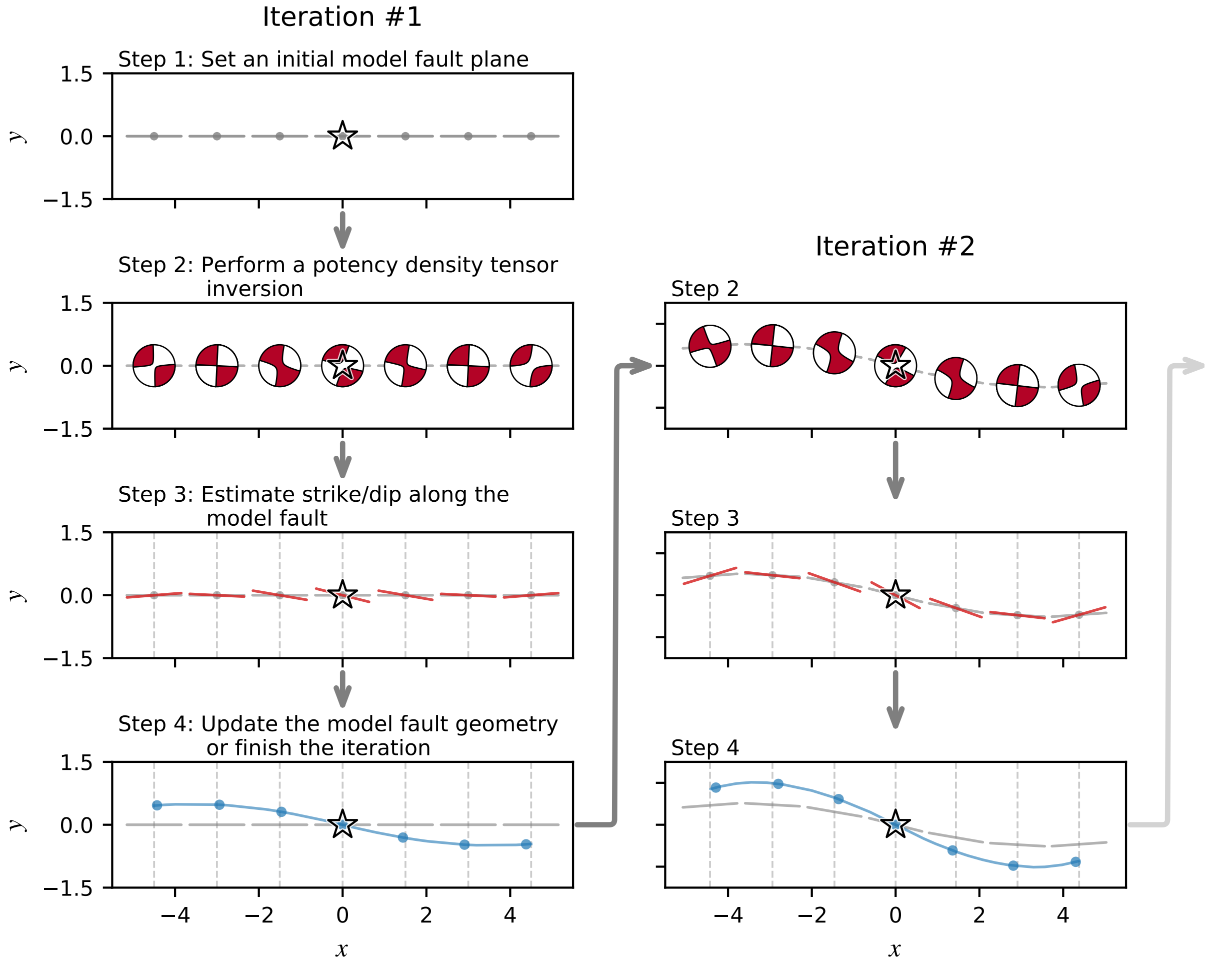

Figure 3.2: Workflow of the iterative inversion process for construction of fault geometry developed in this study. The x axis represents the distance from the hypocenter along the strike (or dip) direction of the initial flat model fault plane. The y axis represents the displacement of the updated model fault plane perpendicular to the x axis. The location of the hypocenter is denoted as the star. Gray bars with gray circles at their centers represent subfaults of the model fault plane used in the finite-fault inversion analysis. The red beach ball at each subfault shown in step 2 represents a focal mechanism obtained by the potency density tensor inversion. The red line in step 3 represents one of the nodal planes of the double-couple components used for constructing fault geometry. The blue line in the step 4 represents the updated fault geometry determined by spline interpolation with quadratic functions and is used as the model fault geometry in the next iteration.

3.1 Workflow

We used the potency density tensor inversion developed in Chapter 2 to construct fault geometry that is consistent with the spatial distribution of the strike or dip of the obtained potency density tensors. Since the obtained potency density tensors is robust to the assumed model fault geometry but is affected to some degree (Figs 2.11 and 2.16), the inversion analysis needs to be performed iteratively to construct the fault geometry, at each step solving the spatial distribution of potency density tensors on the assumed fault surface. In this study, we assumed that the fault geometry changes only either along strike or along dip and also neglected discontinuity of fault and multiplane fault system for simplicity. This assumption results in two types of fault model: a vertical fault with variable strike and uniform dip direction (Fig. 3.1a), and a nonvertical fault with variable dip and uniform strike (Fig. 3.1b). The proposed method consists of four steps.

Step 1: Set an initial model fault plane

The initial model fault is a single rectangle plane, which is placed to roughly cover the possible rupture extent of an earthquake (Step 1 in Fig. 3.2). The model fault is discretized into a finite number of flat subfaults evenly spaced along the strike and dip directions, and each subfault has the same strike and dip as those of the model fault plane. The initial rupture point corresponds to the earthquake hypocenter, which was independently estimated by other studies.

Step 2: Perform a potency density tensor inversion

The potency density tensor inversion is performed to get the spatial distribution of potency density tensors on the initial model fault plane or the non-planar fault surface obtained after the previous iteration. Following the formulation described in Chapter 2, the potency density tensor inversion introducing the modeling error of the Green's function into the data covariance matrix (Yagi & Fukahata, 2011a) stably estimates potency rate density function from observed waveforms (eq. 2.6). Integrating the potency rate density functions in time, we obtain the spatial distribution of the potency density tensors.

Step 3: Estimate strike/dip along the model fault

In this study, we considered that a fault surface curves only along the strike, in which case the fault is flat in the dip direction, or curves only along the dip direction, in which case the fault is flat in the strike direction. We calculate the average potency density tensors along the direction in which the fault is flat. Thus, for example, we obtain focal mechanisms averaged in the dip direction along the strike direction of the model fault surface (Step 2 in Fig. 3.2). In order to construct a model fault surface, it is required to select one of the two nodal planes of the averaged focal mechanism for each subfault. In this study, we select one of the two nodal planes by calculating the inner product between the normal vectors of the two nodal planes and the normal vector of a reference surface defined by the analyst, and the nodal plane with the larger inner product (in the absolute) value is selected as the realistic fault plane (Step 3 in Fig. 3.2). For simplicity, the reference surface is not updated after the first iteration in this study.

Step 4: Update the model fault geometry or finish the iteration

Taking the nodal plane selected in step 3 as the direction of the fault surface, we update the fault geometry by locating the direction of that nodal plane at the center of each subfault. We smoothly connect the central points of the subfaults by adopting a spline interpolation with a quadratic function f_i:

$$\begin{aligned} y &= f_i(x), \\ f_i(x) &= a_i(x - x_i)^2 + b_i(x - x_i) + c_i \qquad (x_i \leq x \leq x_{i+1}), \\ i &= 1, 2, ..., N - 1, \end{aligned} \tag{3.1}$$

where x is the distance from the hypocenter along the strike/dip direction of the initial flat model fault surface, y is the displacement of the model fault surface perpendicular to the initial flat model fault surface, and N denotes the number of subfaults along the strike/dip. The x_i term, which corresponds to a knot of the quadratic function f_i, is the x coordinate of the central point of the ith subfault along the strike/dip.

Here, the unknown parameters are a_i, b_i, and c_i and the total number of them is $3(N - 1)$. The displacement y and its derivative are continuous at the knots from $i = 2$ to $N - 1$:

$$\begin{aligned} f_{i-1}(x_i) &= f_i(x_i), \\ f'_{i-1}(x_i) &= f'_i(x_i), \\ i &= 2, 3, ..., N - 1. \end{aligned} \tag{3.2}$$

The number of these conditions is $2(N-2)$. In addition, the gradient of the fault surface at each knot is given by the direction of the nodal plane selected in step 3:

$$\begin{aligned} y'(x_i) &= d_i, \\ i &= 1, 2, ..., N, \end{aligned} \tag{3.3}$$

where d_i represents the gradient of the fault surface at the ith subfault along the strike/dip. The number of this condition is N. Therefore, by determining the location of the hypocenter (i.e. $f_i(x) = 0$), it is possible to uniquely determine the values of a_i, b_i, and c_i and to obtain the updated geometry of the model fault surface (Step 4 in Fig. 3.2).

After the update of fault geometry, the model fault surface is discretized into rectangular subfaults again. Here, the interval between central points of adjacent subfaults is taken to be the same as the original one and the distance of the strike/dip direction, to which the fault is bending, is measured not along the original fault strike/dip (the x axis) but along the fault surface. In this study, each subfault is not assigned the same area, which yields slight biases in the estimated density of potency. The model fault surface obtained in step 4 is adopted to update the fault geometry, and the process goes back to step 2 (Fig. 3.2).

The iterations end when the strike/dip direction obtained by step 3 is acceptably similar to that of the model fault surface used in the inversion analysis. The similarity of the two strikes/dips is evaluated by the inner product between the unit vectors representing the two strikes/dips. When the inner product averaged over the subfaults along the strike/dip is sufficiently close to 1 (more than 0.99 in this study), the model fault surface is regarded as the fault geometry.

To sum up, the nonlinear inversion method starts from step 1 and then proceeds from step 2 to 4 iteratively. We assign (step 1) or update (step 4) the fault geometry, with which we obtain the potency density tensor distribution (step 2), and then extract the strike/dip from that solution (step 3) to update the fault geometry (step 4).

3.2 Numerical simulation

In order to validate the performance of our proposed method, we performed numerical simulations composed of a strike-slip fault (case 1) and a dip-slip fault (case 2). For both cases,

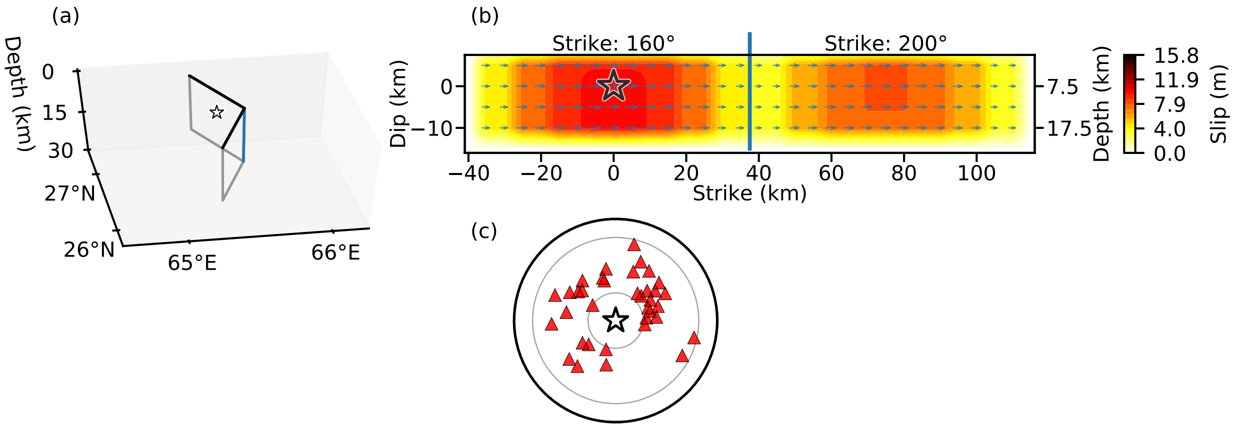

Figure 3.3: Input source model for case 1. (a) Fault geometry in a 3-D view. The input fault plane consists of two vertical planes with different strikes that reach the surface along the black lines and intersect on the blue line. The star denotes the hypocenter. (b) Slip distribution on the input fault plane. The arrows are slip vectors and their lengths are proportional to slip amounts. The star denotes the hypocenter. (c) Station distribution (red triangles) around the epicenter (star) in an azimuthal equidistant projection. The gray circles indicate the 30° and 90° epicentral distances.

we prepared input source models described below, and calculated synthetic velocity waveforms using theoretical Green's functions. In both cases, the slip-rate function at each subfault was represented as a combination of linear B-spline functions with a 0.8 s interval. Theoretical Green's functions were calculated following the method of Kikuchi & Kanamori (1991) at 0.1 s intervals, and the attenuation time constant t^* for the P wave was taken to be 1.0 s. The one-dimensional near source velocity structures for the cases 1 and 2 are listed in Tables 2.1 and 3.1, respectively. In the calculation of the synthetic waveforms, errors in the Green's function and background noise were added to the synthetic waveform. We added random Gaussian noise with zero mean and a standard deviation of 5% of the maximum amplitude of each calculated Green's function to each calculated Green's function as an error of Green's function. We then added random Gaussian noise with zero mean and a standard deviation of 1 μm as the background noise. In the inversion process, the calculated synthetic waveform data was resampled at a 0.8 s interval, and the calculated waveforms or the theoretical Green's functions were not low-pass filtered.

3.2.1 Case 1: Strike-slip fault with variable strike

We applied the proposed method for a vertical fault variating strike angle with uniform dip angle. The input fault is composed of two vertical fault planes, each one 75 km long and 20 km

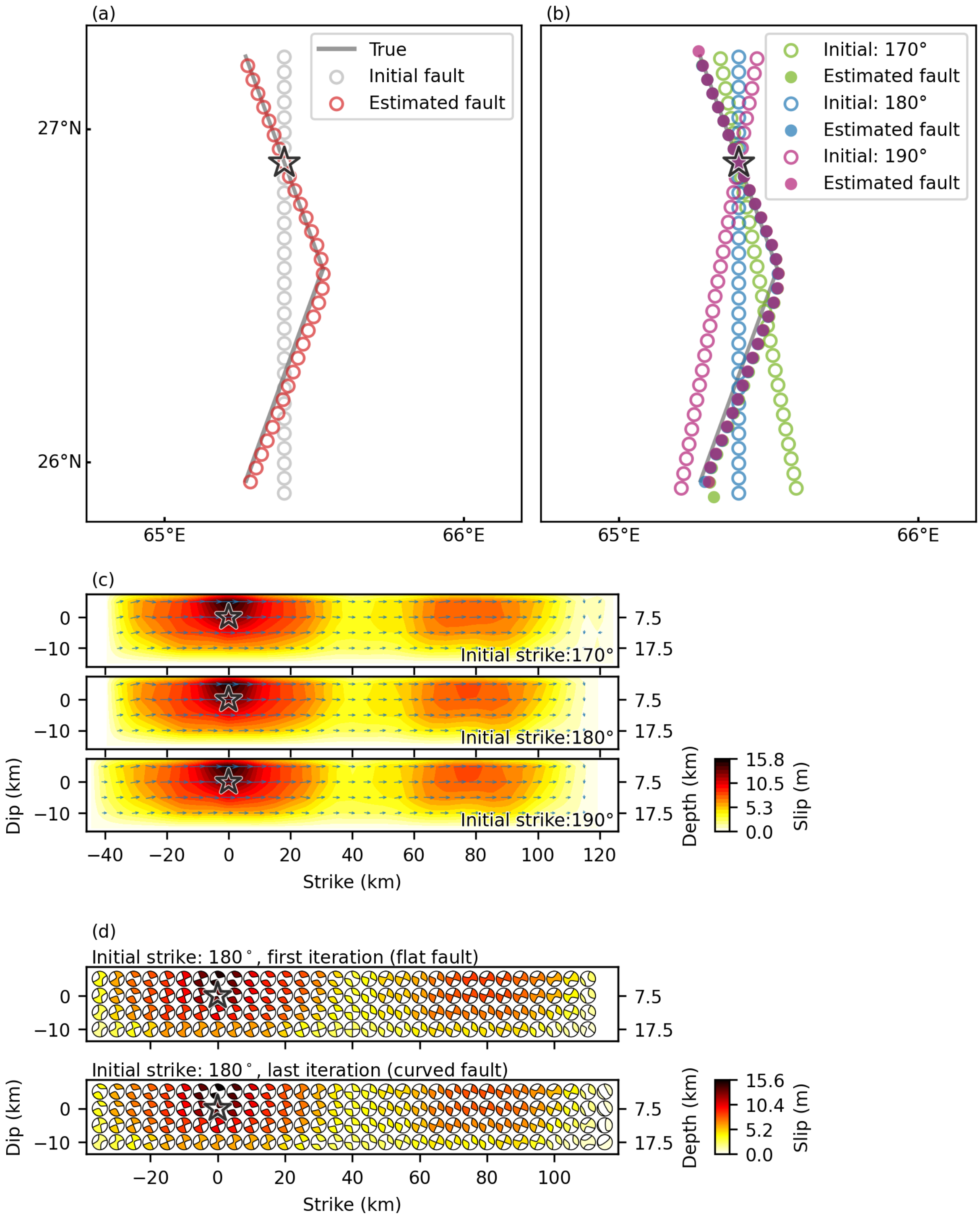

Figure 3.4: *Caption next page.*

Figure 3.4: Results of case 1 in synthetic tests. (a) True, initial, and estimated fault traces. Trace of the true fault surface is drawn by the gray line. The central points of subfaults of the initial and estimated model fault surfaces are represented by gray and red circles, respectively. The star denotes the epicenter. (b) Results of sensitivity test to the strike of the initial model fault plane. All three initial fault planes (open circles) result in estimated fault traces (filled circles) that are almost indistinguishable at the scale of this plot. (c) Slip distribution estimated on the model fault surface. The arrows represent slip vectors and their lengths are proportional to slip amounts. (d) Potency density tensor distribution obtained after the first (flat model surface) and the last iterations (curved model surface) in the case 1 in synthetic tests. The beach ball represents the focal mechanism at each subfault and their color shows the amount of slip. The star denotes the hypocenter.

wide, with strikes of 160° and 200°, respectively (Fig. 3.3a). Two slip patches are distributed on the fault, and the slip direction is pure right lateral (Fig. 3.3b). The total duration of input slip-rate function at each subfault was assumed to be 6 s, and the hypocenter location was 26.900°N, 65.400°E at a depth of 7.5 km. Rupture of each subfault was triggered by the expanding circular rupture front propagating from the hypocenter at 3 km/s. Synthetic waveforms were calculated for the selected stations shown in Fig. 3.3c.

In the inversion analysis, we adopted the initial model fault as a vertical plane with a length of 150 km, a width of 20 km, and a strike of 180° (Fig. 3.4a). The potency rate density functions on this plane were expanded by bilinear B-spline functions with a spatial interval of 5 km and by linear B-spline functions with a temporal interval of 0.8 s and a total duration of 6 s. The hypocenter was the same one used as the input, and the maximum rupture front velocity was assumed to be 3 km/s. As a reference plane for selecting a realistic nodal plane in Step 3 of the nonlinear inversion method, we adopted the plane with 354° strike and 89° dip obtained from the total potency tensor in the preliminary analysis.

The fault model, constrained by two iterations, showed straight parts and a bend of fault and well reproduced the geometric features of input fault (Fig. 3.4a). The estimated slip distribution showed two slip patches and overall pure right lateral slip direction (Fig. 3.4c), which is consistent with the slip distribution of input source model (Fig. 3.3b). Although the potency density tensor distributions obtained after the first and the last iterations are quite similar to each other (Fig. 3.4d), the source model obtained after the last iteration also reproduced fault geometry of the input source model (Fig. 3.4a). This can be said as the advancement made in this study because our proposed method helps us interplate a source model and its fault geometry better. We tested sensitivity of a constructed fault geometry to the strike of the initial model plane by

Table 3.1: Near-source velocity model from CRUST1.0 (Laske *et al.*, 2013) used for calculating Green's functions.

V_P (km/s)	V_S (km/s)	Density (10^3kg/m^3)	Thickness (km)
6.00	3.52	2.72	27.25
6.30	3.68	2.79	13.08
6.60	3.82	2.85	14.17
8.44	4.68	3.45	0.00

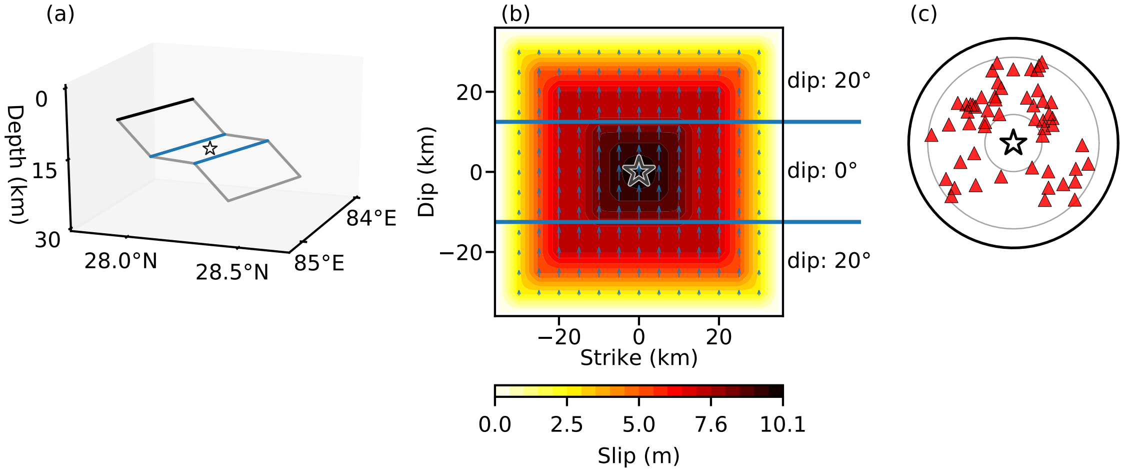

Figure 3.5: Input source model for case 2. (a) Fault geometry in a 3-D view. The input fault plane consists of three planes with a ramp-flat-ramp structure. Black and blue lines are top of model fault and intersections of sub-planes, respectively. The star denotes the hypocenter. (b) Slip distribution on the input fault plane. The arrows represent slip vectors and its length is proportional to slip amount. (c) Station distribution (red triangles) around the epicenter (star) in an azimuthal equidistant projection. The gray circles indicate the 30° and 90° epicentral distances.

changing it to 170° and 190°, and obtained the similar results (Figs 3.4 b and c). However, the fault model with a 170° initial strike slightly deviated from the true fault geometry at the southern end of the model fault (Fig. 3.4b). It would be originated from a large deviations of the initial fault plane from the true one and the modeling error of the Green's function increasing with distance from the hypocenter. These results prove that the proposed method can be used for constructing faults with variable strike under the condition that the initial model fault plane is reasonably accurate.

3.2.2 Case 2: Reverse fault with variable dip angle

We applied the proposed method for a nonvertical fault with variable dip and uniform strike. The input fault is composed of three adjacent planes with different dips (Fig. 3.5a). The three

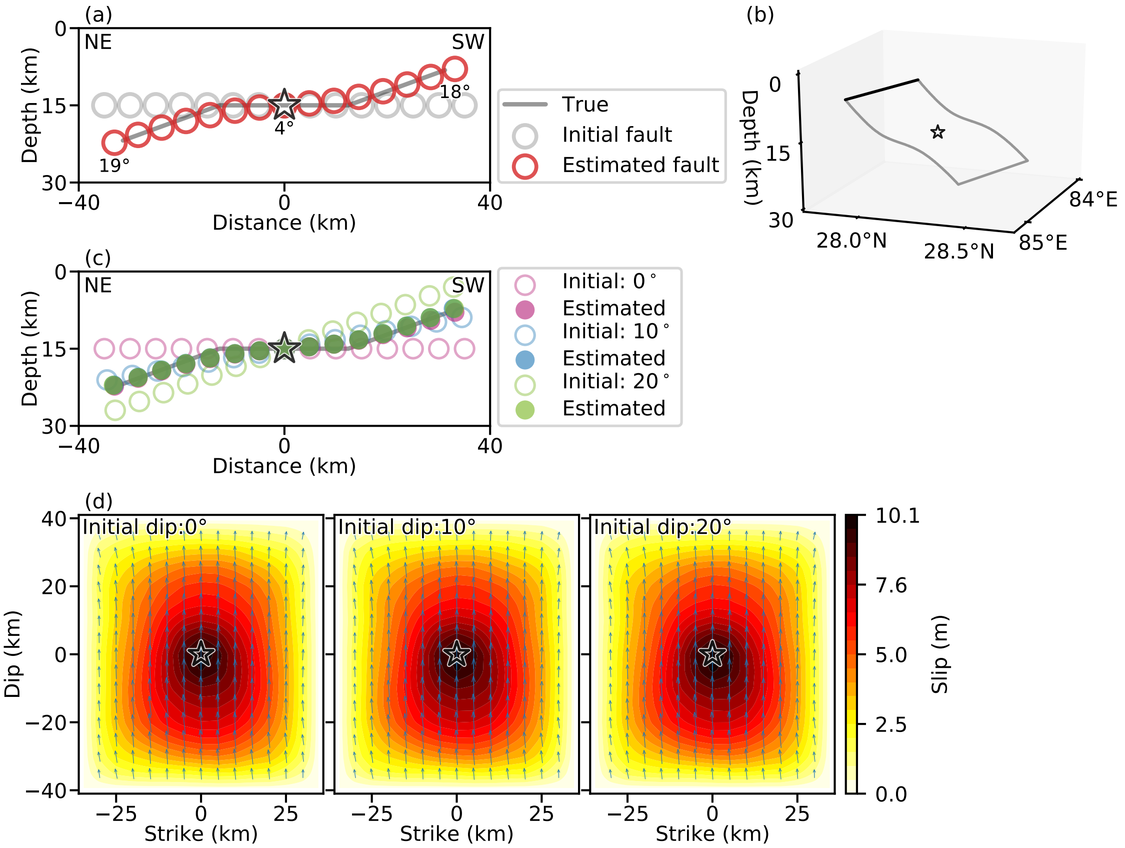

Figure 3.6: Results of synthetic test case 2. (a) Cross sections of the true, initial, and estimated fault surfaces. (b) Estimated fault geometry in a 3-D view. The star denotes the hypocenter. (c) Results of sensitivity test to the dip of the initial fault plane. All three initial fault planes (open circles) result in estimated fault traces (filled circles) that are indistinguishable at the scale of this plot. (d) Estimated slip distribution on the model fault surface. The arrows represent slip vectors and their lengths are proportional to slip amounts.

planes had a 285° strike and together extended 65 km; from top to bottom their dips were 20°, 0° and 20°, and their widths were 20 km, 25 km, and 20 km, respectively. The input source model has a large slip patch at around the center of the fault and pure dip slip (Fig. 3.5b). The total duration of input slip-rate function at each subfault was assumed to be 10 s, and the hypocenter location was 28.231°N, 84.731°E at a depth of 15 km. Rupture of each subfault was triggered by the expanding circular rupture front propagating from the hypocenter at 3 km/s. Synthetic waveforms were calculated for the selected stations shown in Fig. 3.3c.

In the inversion analysis, We adopted a horizontal plane with a length of 65 km, a width of 75 km, a depth of 15 km, and a strike of 285° as the initial model fault (Fig. 3.6b). The potency rate density functions on this plane were expanded by bilinear B-spline functions with a spatial interval of 5 km and by linear B-spline functions with a temporal interval of 0.8 s and a total duration of 10 s. The hypocenter was the same one used as the input, and the maximum rupture front velocity was assumed to be 3.0 km/s. As a reference plane for selecting a realistic nodal plane, the plane with 273° strike and 11° dip derived from the total potency tensor obtained from the preliminary analysis was adopted.

The obtained fault model after two iterations, shown in Fig. 3.6a a cross sectional view and in Fig. 3.6b as as a 3-D view, is characterized by a dip ranging from 4° around the hypocenter to 18° and 19° near the up-dip and down-dip edges, respectively. The obtained fault geometry was slightly smoother than the input but reproduced the geometric pattern of input fault geometry and its slip distribution well (Fig. 3.6d). We tested the sensitivity of source model to the dip of the initial model plane by changing it to 10° and 20°, we obtained the similar results (Figs 3.6 c and d). These results prove that the proposed method can be used for constructing faults with bending along dip.

3.3 Application to real waveforms

In order to further examine the validity of the proposed method, we applied it to teleseismic waveforms of the M_{W} 7.7 2013 Balochistan, Pakistan, and the M_{W} 7.9 2015 Gorkha, Nepal, earthquakes. Fault geometries of the both earthquakes have been probed by previous studies and shown that they occurred on non-planar faults. Thus, these earthquakes provide us opportunities to test whether the proposed method can reconstruct curved fault geometries.

3.3.1 The 2013 Balochistan earthquake

Global Centroid Moment Tensor (GCMT; Dziewonski *et al.*, 1981; Ekström *et al.*, 2012, https://www.globalcmt.org/CMTsearch.html) solution and the *W*-phase moment tensor solution determined by the U.S. Geological Survey, National Earthquake Information Center (USGS NEIC; https://earthquake.usgs.gov/earthquakes/eventpage/usb000jyiv) indicated that the Balochistan earthquake was a strike-slip event. Analyses of optical satellite images acquired after the earthquake (Avouac *et al.*, 2014; Jolivet *et al.*, 2014; Zinke *et al.*, 2014) showed surface displacements describing a curve convex to the south-east. The teleseismic *P*-waveform inversion analysis described in Chapter 2 provided a source model showing strike-slip faulting in which the strike orientation clockwisely rotates from 205° at the north end to 240° at the south end (Figs 2.10 and 2.11).

In this Chapter, our inversion analysis used the vertical components of teleseismic *P* waveforms observed at 36 stations shown in Fig. 3.3c and converted to velocity (Fig. 3.9), the same data used in Chapter 2, and then resampled the waveform data at a 0.8 s interval without applying any filter. We adopted the epicenter of USGS finite-fault model and the hypocentral depth of 7.5 km used in Chapter 2. Theoretical Green's functions were computed the same way as the synthetic tests in Section 3.2, using the one-dimensional near source velocity structure (Table. 2.1) used in Avouac *et al.* (2014). The initial fault plane had a length of 200 km and a width of 20 km, with a strike of 230° and a dip of 90°, that roughly followed the trace of the surface rupture observed by Zinke *et al.* (2014) (Fig. 3.7a). The potency rate density functions on this plane were expanded by bilinear B-spline functions with a spatial interval of 5 km and by linear B-spline functions with a temporal interval of 0.8 s and a total duration of 31 s. We also assumed the maximum rupture-front velocity to be 4 km/s and the total source duration to be 60 s, following the finite-fault inversion analysis in Chapter 2. We adopted a plane with a strike of 226° and a dip of 69°, derived from the total potency tensor obtained by a preliminary analysis, as the reference surface used for selecting realistic nodal planes in step 3 of our nonlinear inversion approach.

The nonlinear procedure finished after the third iteration, and the resultant source model is shown in Fig. 3.7 and well reproduced observed waveforms at all stations (Fig. 3.9) with the variance (eq. 2.17) of 0.307. The estimated fault trace is 205 km long and shows a curved pattern whose strike angle smoothly changes from 218° at the northern edge around 50 km

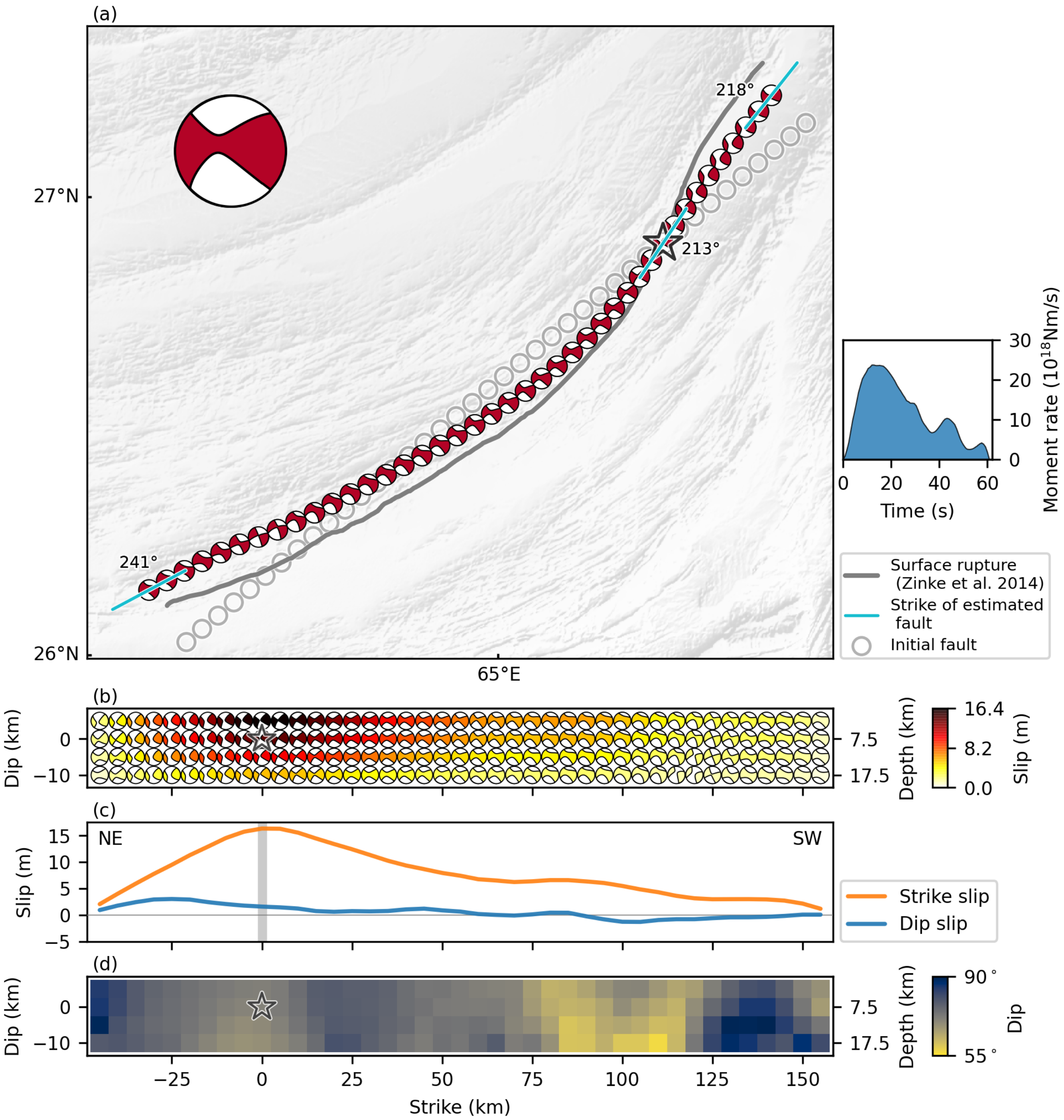

Figure 3.7: *Caption next page.*

Figure 3.7: Fault geometry and slip distribution of the 2013 Balochistan earthquake estimated in this study (a) Gray circles represent the center of subfaults of the initial fault plane. The small beach ball symbols show the focal mechanisms of the subfaults on the estimated fault trace, obtained by integrating the potency density tensors, shown in (b), with respect to the dip direction. Blue bars and numbers indicate the strike orientations of the subfaults at the hypocenter and both ends of the estimated fault. The large beach ball symbol shows the total potency tensor of the earthquake, obtained by integrating the potency density tensors shown in (b), over the fault surface. The gray line represents the surface rupture trace observed by Zinke *et al.* (2014). The moment rate function of the earthquake estimated in this study is shown at the right of the map. The star denotes the epicenter. Topography was drawn by using 2010 GMTED 7.5 arc-second median elevations (https://topotools.cr.usgs.gov/gmted_viewer/) (Danielson & Gesch, 2011). (b) Potency density tensor distribution on the estimated fault surface. beach ball symbols indicate the focal mechanism at each subfault and their color indicates the slip amount. (c) strike-slip and dip-slip profiles along the model fault trace, which was estimated from the potency density tensors at the top of the fault surface. The strike-slip component is positive for left-lateral faulting, and the dip-slip component is positive for reverse faulting. The gray vertical bar represents the location of the epicenter. (d) Distribution of dip angle (color) on the estimated fault surface.

north-east of the epicenter, to 213° around the epicenter, to 241° at the southern edge around 140 km south-west of the epicenter (Fig. 3.7a). The curved pattern of fault geometry is consistent with the curved pattern of surface rupture trace observed after the earthquake (e.g. Zinke *et al.*, 2014), shown by the gray line in Fig. 3.7a, but the estimated fault geometry is slightly smoother than the observed surface rupture trace, which may be originated from our methodology uniformly assigning the vertical dip angle along the fault surface. Focal mechanisms along the estimated fault trace (Fig. 3.7a), obtained by integrating the potency density tensors (Fig. 3.7b) along the dip direction, are predominated by strike-slip faulting. Integrating the potency density tensors (Fig. 3.7b) over the model fault surface, we obtained the total potency tensor of this earthquake (Fig. 3.7a), which shows strike-slip faulting with a strike of 226° and a dip of 69°. The total seismic moment release is 6.16 × 10 Nm (M_W 7.8), which is comparable to the estimate of 7.53×10^{20} Nm (M_W 7.8) in Chapter 2 and the GCMT solution of 5.59×10^{20} Nm (M_W 7.8). The estimated source-time function has a prominent peak at around 12 s and three minor peaks at around 28, 43, and 58 s (Fig. 3.7a), which is comparable to the results in Chapter 2 (Figs 2.10 and 2.16b).

Focal mechanisms are composed of two nodal planes, and we could select the realistic fault plane from the focal mechanisms obtained in this inversion analysis by using the same criteria as used in step 3 in our nonlinear inversion approach (Figs 3.7 a and b). Decomposing the

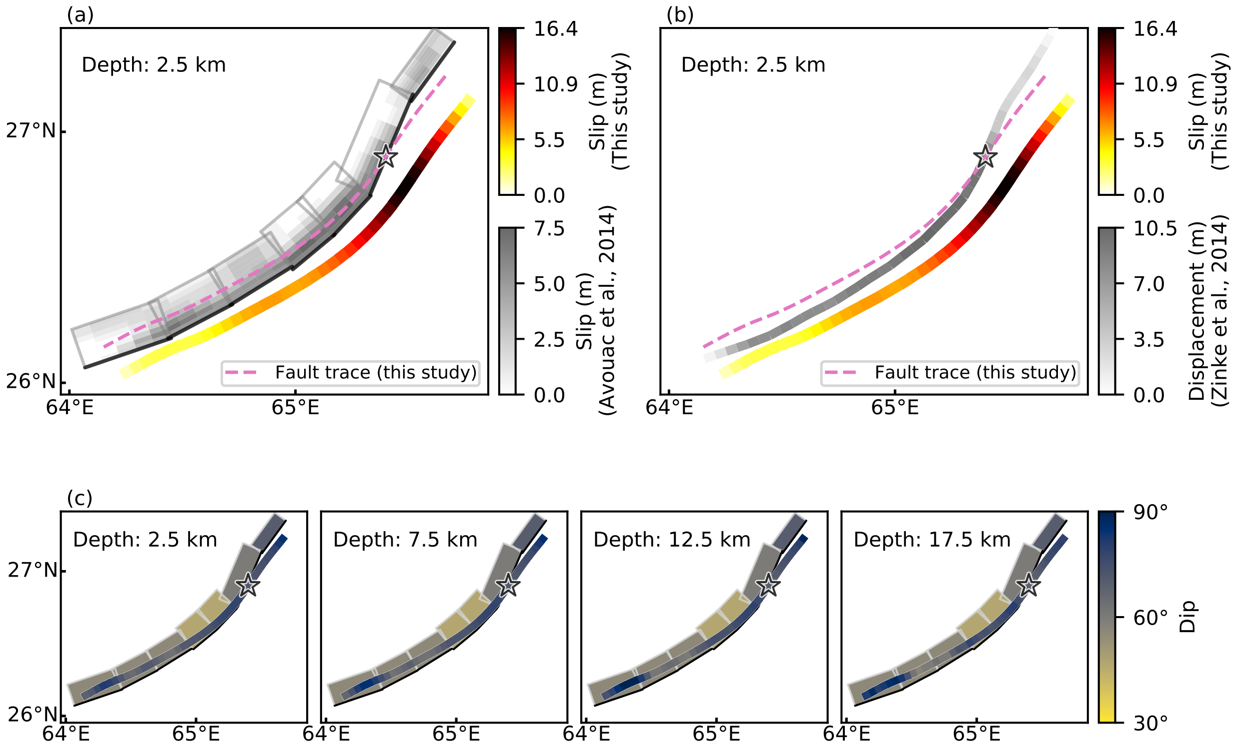

Figure 3.8: Finite-fault source model of the Balochistan earthquake obtained this study compared with that of Avouac *et al.* (2014) and the surface displacements obtained by the analysis of optical image correlation by Zinke *et al.* (2014). (a) Slip distribution obtained in this study and Avouac *et al.* (2014). Slip distribution of Avouac *et al.* (2014) is shown as the background gray color and outlined by the black and gray lines. Slip distribution at the top layer (2.5 km depth) of the fault plane estimated in this study is represented as the warm colored line, which is drawn at the shifted location from the trace of the estimated fault (pink dashed line) for visibility. The star denotes the epicenter. (b) Slip distribution obtained in this study and the surface displacements estimated by Zinke *et al.* (2014). Surface displacements of Zinke *et al.* (2014) are represented as the gray colored line. Slip distribution at the top layer (2.5 km depth) of the fault plane estimated in this study is represented as the warm colored line, which is drawn at the shifted location from the trace of the estimated fault (pink dashed line) for visibility. The star denotes the epicenter. (c) Dip distribution at each depth of the fault estimated in this study (drawn as a curved line) and that of the finite-fault source model of Avouac *et al.* (2014). The star denotes the epicenter.

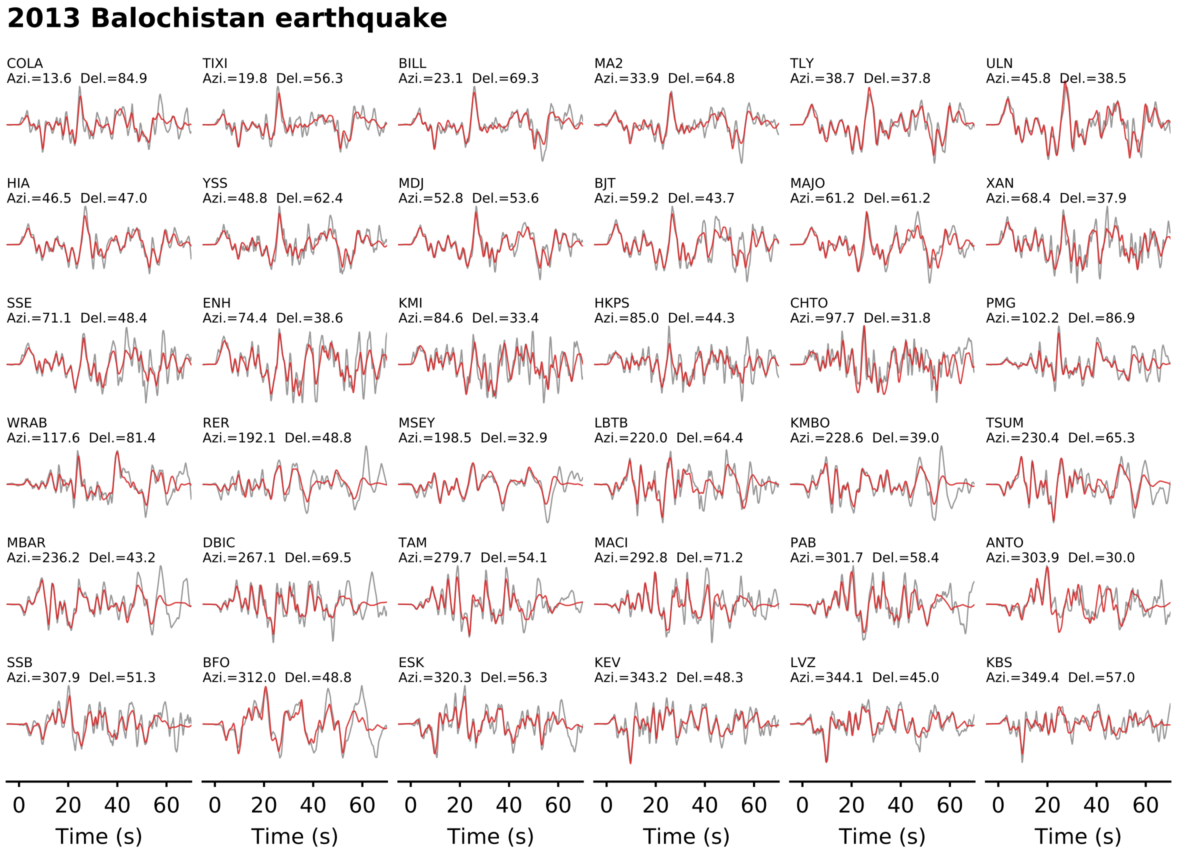

Figure 3.9: Waveform fitting at all stations between observed (gray line) and synthetic waveforms (red line) in the analysis of the Balochistan earthquake by using the constrained fault model. Station code, azimuth, and epicentral distance of each station are shown above the traces. The variance (eq. 2.17) is 0.307.

potency density tensors at the top of the fault into the strike-slip component (positive for left-lateral and negative for right-lateral fault slip) and the dip-slip component (positive for reverse and negative for normal fault slip), we recognized that left-lateral strike-slip is predominant, reaching a maximum of 16.3 m near the epicenter and gradual decrease toward both ends of the fault (Fig. 3.7c). The dip-slip component has a maximum value of 3.0 m at around 25 km north-east of the epicenter and decreases to −1.3 m (1.3 m normal faulting) at around 100 km south-west of the epicenter involving small fluctuation (Fig. 3.7c).

By selecting realistic fault planes from the estimated potency density tensors, we obtained distribution of dip angles on the fault surface and recognized the variation of dip angles ranging from 57° to 89° (Fig. 3.7d). The dip is clearly depth-dependent, being steeper in the shallower part of the fault surface, especially around the epicenter and in the area 100 km south-west of the epicenter (Fig. 3.7d), consistent with the idea of a listric fault. In the vicinity of the epicenter, the dip increases gradually from 68° at 17.5 km depth to 72° at 2.5 km depth (Fig. 3.7d). In the are around 100 km south-west of the epicenter, the dip angle increases from 60° at 17.5 km depth to 71° at 2.5 km depth (Fig. 3.7d), indicating that the depth dependence of the dip angle is clearer than that around the epicenter.

3.3.2 The 2015 Gorkha earthquake

According to the GCMT solution (Dziewonski *et al.*, 1981; Ekström *et al.*, 2012) and the W-phase moment tensor solution determined by the USGS NEIC (https://earthquake.usgs.gov/earthquakes/eventpage/us20002926) indicate that the Gorkha earthquake was a thrust event with a fault plane dipping at 7°. A teleseismic P-waveform inversion analysis (Yagi & Okuwaki, 2015) provided a finite-fault source model in which the main rupture area was distributed around 50 km east of the epicenter. The Gorkha earthquake has been reported to have occurred along the Main Himalayan Thrust (e.g. Avouac *et al.*, 2015; Elliott *et al.*, 2016; Hubbard *et al.*, 2016; Duputel *et al.*, 2016). An analysis of Interferometric Synthetic Aperture Radar (InSAR) and Global Navigation Satellite System (GNSS) data (Elliott *et al.*, 2016) showed that the earthquake occurred on a north-dipping fault with a ramp-flat-ramp structure, dipping at 30° from the surface to 5 km depth, 7° in a relatively flat section 75 km wide, and 20° in the deepest section 30 km wide. Hubbard *et al.* (2016) proposed a similar geometric model of the Main Himalayan Thrust, covering the source area of the Gorkha earthquake, on the basis of geologi-

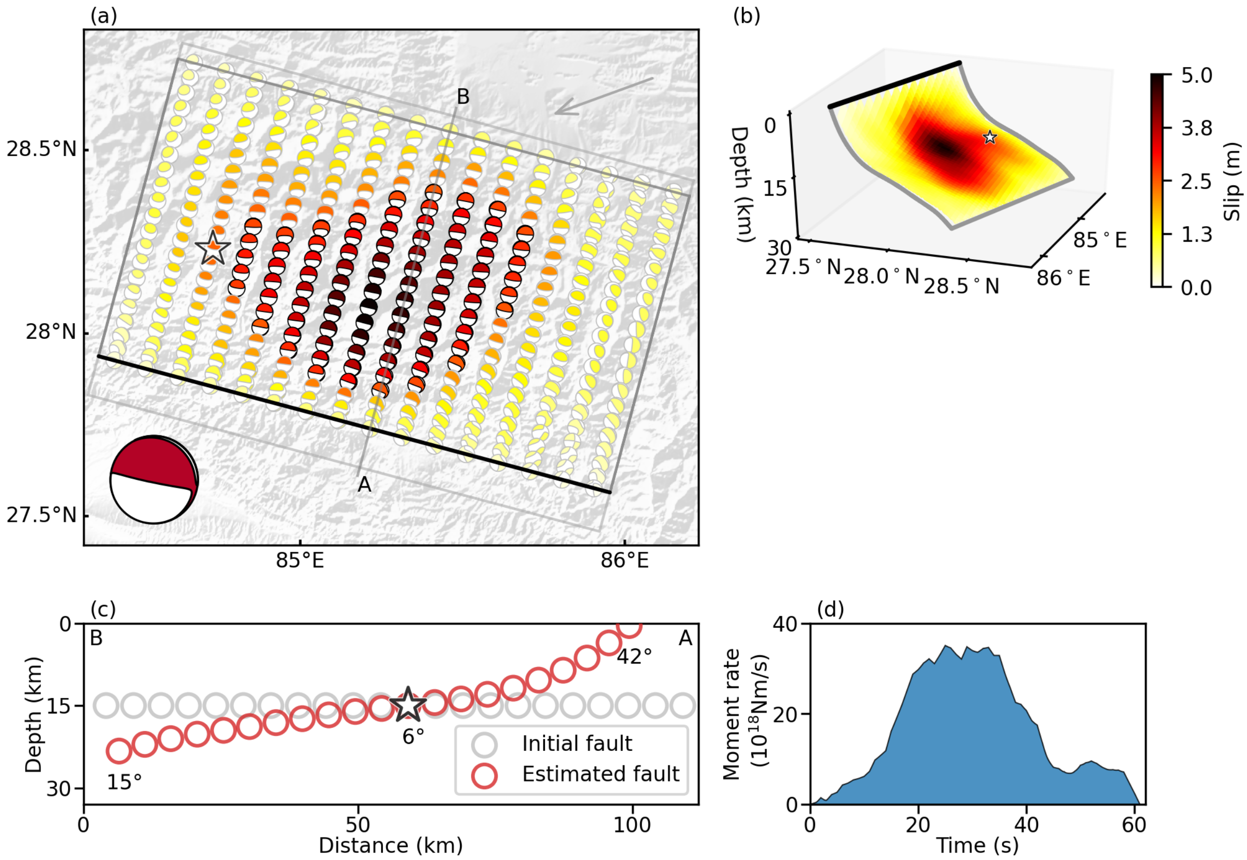

Figure 3.10: Source model of the 2015 Gorkha earthquake estimated by the proposed method. (a) Potency density tensor distribution on the estimated fault surface. The light gray line outlines the initial fault plane. Small beach ball symbols indicate the focal mechanism for each subfault and their color indicates the slip amount according to the color scale in (b). The beach balls more than 50% of the maximum slip amount are emphasized by black lines. The large beach ball symbol shows the total potency tensor of the earthquake, obtained by integrating the potency density tensors over the fault surface. Arrow indicates azimuth of 3-D view of (b). Topography was drawn by using 2010 GMTED 7.5 arcsecond median elevations (https://topotools.cr.usgs.gov/gmted_viewer/) (Danielson & Gesch, 2011). (b) 3-D view of the estimated fault geometry and slip distribution viewed from the north-east indicated by the arrow in (a). (c) Cross section of the model-fault surface along line A–B in (a). Central points of subfaults of the initial and estimated model fault surfaces are represented by gray and red circles, respectively. Denoted numbers are dip angles at the hypocenter and both ends of the estimated fault. (d) Moment rate function of the earthquake estimated in this study.

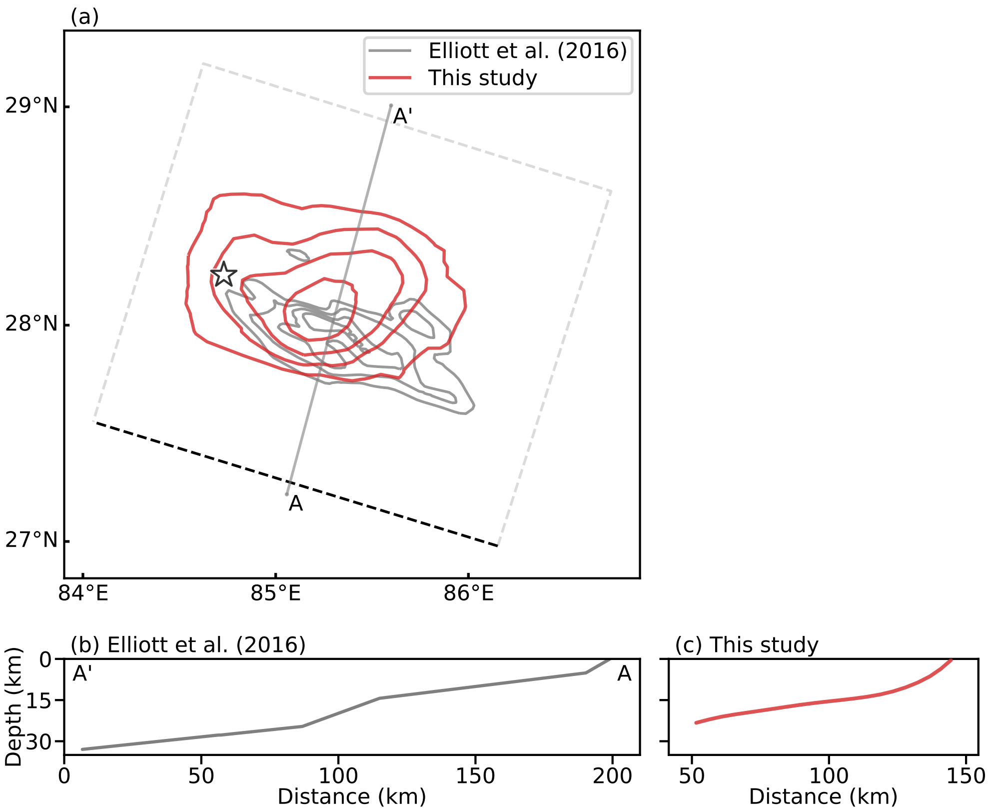

Figure 3.11: Fault geometry and slip distribution of the Gorkha earthquake estimated in this study and Elliott *et al.* (2016). (a) Slip distribution estimated in this study (red line) and Elliott *et al.* (2016) (gray line). The top of fault surface estimated by Elliott *et al.* (2016) is shown by the black dashed line, and the gray dashed lines outline the dipping fault surface. Contour intervals of this study and Elliott *et al.* (2016) are 1.0 m and 1.6 m, respectively. The star denotes the epicenter. (b) Cross section of the model fault estimated by Elliott *et al.* (2016) along line A–A' in (a). (c) Cross section of the model fault estimated in this study along line A–A' in (a).

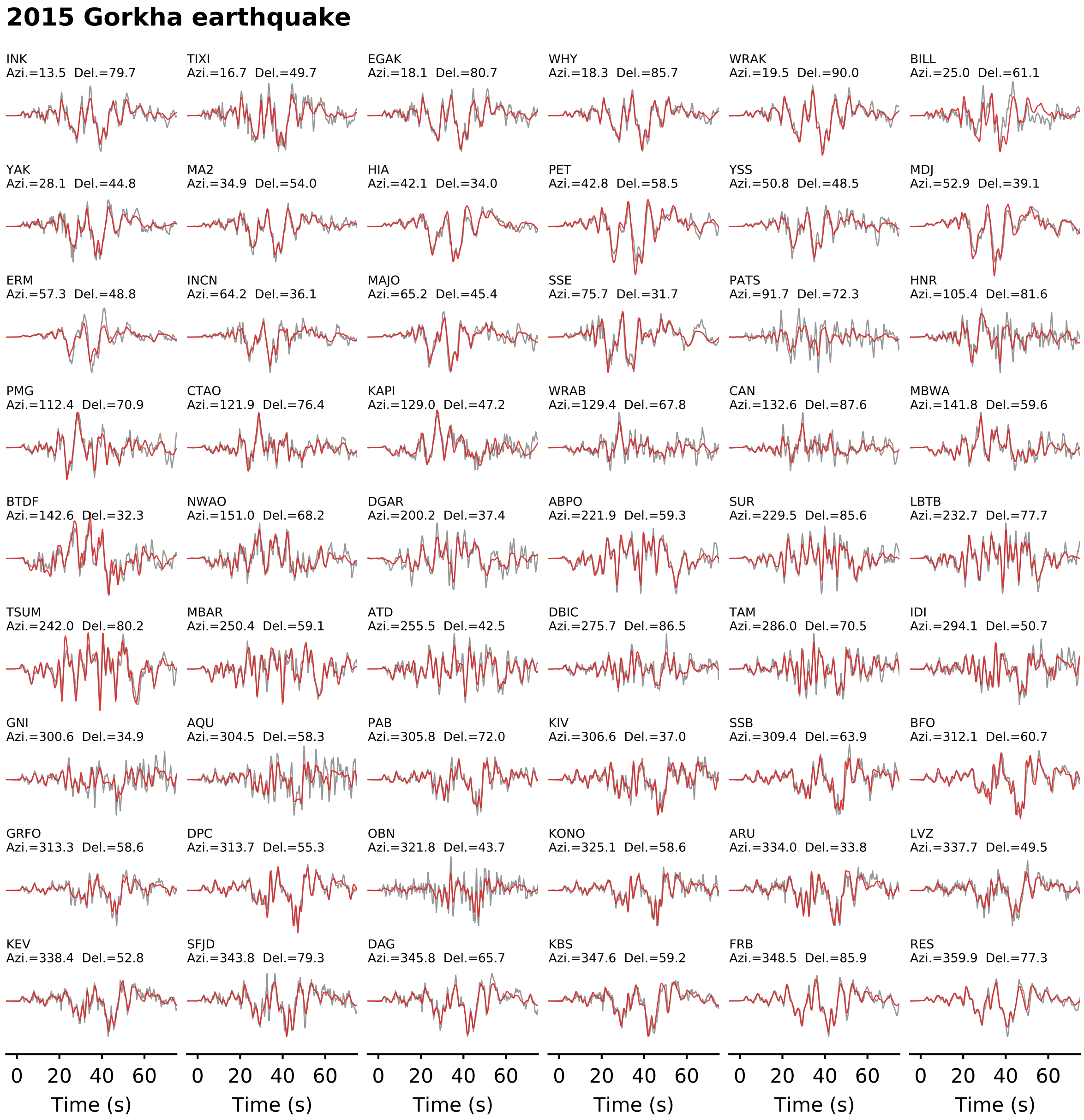

Figure 3.12: Waveform fitting at all stations between observed (gray line) and synthetic waveforms (red line) in the analysis of the Gorkha earthquake. Station code, azimuth, and epicentral distance at each station are shown above the traces. The variance (eq. 2.17) is 0.179.

cal data in which the central portion had a 7° dip and the adjoining portions on the up-dip and down-dip sides had a 26° dip. Duputel *et al.* (2016) conducted a receiver function analysis and proposed a ramp-flat-ramp fault geometry for the Gorkha earthquake.

In the inversion analysis, we used vertical components of teleseismic *P* waveforms observed at the 54 stations shown in Fig. 3.5c and converted to velocity waveforms (Fig. 3.12), which are the same teleseismic waveforms used by Yagi & Okuwaki (2015), and then resampled the waveform data at a 1.0 s interval without applying any filter. We adopted the USGS epicenter (28.231°N, 84.731°E) and the hypocentral depth of 15 km used by Yagi & Okuwaki (2015). Theoretical Green's functions were computed using the one-dimensional near-source velocity structure (Table 3.1) of the CRUST 1.0 model (Laske *et al.*, 2013) in the same way as the synthetic tests in Section 3.2. The initial fault plane has a length of 160 km and a width of 110 km with a strike of 285° and a dip of 0°, that entirely covered the possible source region estimated by Yagi & Okuwaki (2015) (Fig. 3.10a). The potency rate density functions on the model fault plane were expanded by bilinear B-spline functions with a spatial interval of 10 km and 5 km along the strike and dip directions, respectively, and by linear B-spline functions with a temporal interval of 1.0 s and a total duration of 28 s. Following Yagi & Okuwaki (2015), we assumed the maximum rupture-front velocity to be 3 km/s and the total source duration to be 60 s. We adopted a plane striking 326° and dipping 8°, derived from the total potency tensor obtained by a preliminary analysis, as the reference surface used for selecting realistic nodal planes.

The nonlinear inversion procedure finished after the third iteration, and the resultant source model is shown in Fig. 3.10 and well reproduced observed waveforms (Fig. 3.12) with a variance (eq. 2.17) of 0.179. The fault plane dips towards the north-east and is 105 km wide (Figs 3.10 b and c). The potency density tensor distribution (Fig. 3.10a) shows that the main rupture area, more than 50% of the maximum slip, is distributed around 50 km east of the epicenter with the maximum slip of 5.0 m and is dominated by thrust faulting with dip angles ranging from 2° to 22°. The total potency tensor shows thrust faulting with a strike of 332° and a dip of 9° (Fig. 3.10a). The total seismic moment release is 9.1×10^{20} Nm (M_W 7.9), which is consistent with the 9.1×10^{20} Nm (M_W 7.9) estimated by Yagi & Okuwaki (2015). The cross sectional view of the estimated fault surface (Fig. 3.10c) perpendicular to the fault strike (the A–B line shown in Fig. 3.10a), indicates a variation of dip angle, showing 42° at the up-dip edge around 45 km south-west of the hypocenter, 6° at the hypocenter and 15° at the down-dip edge around 55 km north-east of the hypocenter. The three-dimensional view of the fault model (Fig. 3.10b) showed that the main rupture area was distributed in the low-dipping (<10°) flat part of the model fault plane, and the main rupture area was surrounded by a high-dipping ramp structure.

3.4 Discussion

In this Chapter, we proposed a nonlinear inversion approach to construct the fault geometry of an earthquake by adopting the finite-fault potency density tensor inversion estimating spatial distribution of potency density tensors on an assumed fault plane and providing us information on slip direction on the fault plane. Through synthetic tests and applications to real waveform data, we showed that our proposed method successfully construct the fault geometry, even if the strike or dip along the fault surface changes. Thus, it is possible to more directly compare the obtained source model with other observational data, as can be done for source models provided by conventional finite-fault inversion methods.

The surface ruptures after the Balochistan earthquake recorded by Zinke *et al.* (2014) can be easily compared with our source model (Fig. 3.7a) and found to be in good agreement. The prominent surface displacement around the hypocenter in our model (Figs 3.7 b and c) is also consistent with the distribution of surface displacement across the fault trace estimated by the analyses of optical satellite images (e.g. Avouac *et al.*, 2014; Zinke *et al.*, 2014) and the slip distribution of finite-fault model of Avouac *et al.* (2014) (Figs 3.8 a and b). The Arabia plate subducts under the Eurasia plate in the southern part of the Makran accretionary wedge, and it has been shown that active thrust faults exist in the Makran accretionary wedge (Haghipour *et al.*, 2012), the site of the Balochistan earthquake source area. The estimated depth dependent dip angle on the constructed fault surface, showing shallowing dip with increasing depth (Fig. 3.7d), may suggest that the earthquake ruptured such the thrust fault having listric geometry. Our source model shows a distribution of dip angles that is steep near the epicenter and shallow in the area about 100 km south of the epicenter (Fig. 3.7d), and its dip angle variation along strike seems discontinuous and basically steeper than those in the models of Avouac *et al.* (2014) (Fig. 3.8c) and Jolivet *et al.* (2014). Although our model supports the idea of a listric fault geometry ruptured by the Balochistan earthquake as discussed in Avouac *et al.* (2014) and Jolivet *et al.* (2014), it should be difficult to judge whether model of Avouac *et al.* (2014) or

Jolivet *et al.* (2014) would be more comparable with our model.

Since rupture of the Gorkha earthquake did not reach the surface of the Earth (e.g. Avouac *et al.*, 2015), there are no observational data that can be compared directly with our estimated fault geometry. Our source model of the Gorkha earthquake represents a ramp-flat-ramp fault structure (Figs 3.10 b, c and 3.11), which is consistent with the fault geometry modelled by using geophysical and geological data (e.g. Elliott *et al.*, 2016; Hubbard *et al.*, 2016; Duputel *et al.*, 2016), although the flat section in our model is narrower than those studies. In particular, the upper and lower ramp structures of our fault model seems to represent the middle and deep ramps of the Main Himalayan Thrust model proposed by Hubbard *et al.* (2016). The estimated slip distribution, in which larger slip is concentrated in the flat part of fault (Figs 3.10 a, b and 3.11), is also consistent with the analysis result of InSAR and GNSS data by Elliott *et al.* (2016). The fault model proposed by Hubbard *et al.* (2016), using geological knowledge and the slip distribution estimated by Avouac *et al.* (2015), also places the main rupture area in the flat part of the fault. Although the dip angles of the ramp structures in the up- and down-dip parts of our fault model are not exactly equal to those of the fault geometry modelled by Hubbard *et al.* (2016), our source model seems to resolve the main rupture area surrounded by the ramp structures, which is consistent with the model of Hubbard *et al.* (2016). Therefore, our proposed method, based solely on teleseismic data, provides a source model of the Gorkha earthquake that is comparable to fault geometry and slip distributions independently estimated from geophysical and structural geology.

Since our proposed method employs spline interpolation to construct the fault geometry, continuous and geometrically smooth faults are suitable for this method. Furthermore, a realistic strike or dip is selected at each subfault on the basis of the similarity of the resolved nodal plane to the single reference surface for simplicity. This procedure implicitly limits the variation of strike or dip to 45° or less because a rotation of a focal mechanism around its own B axis greater than 45° reverses the similarity of the conjugate nodal plane to the reference surface. This assumption was sound in the cases the Balochistan and Gorkha earthquakes because the variations of strike and dip of their faults were within 45°. Our proposed method may be extended to construct a fault geometry with a greater variation of strike or dip than 45° by determining a realistic nodal plane on the basis of the nodal plane of the adjacent subfault and sequentially extending this procedure in the direction away from the epicenter. Unlike the geodetic data inversion method, the method proposed in this study can estimate not only the fault geometry but also the rupture process, and can be applied to earthquakes that occurred on the seafloor where geodetic observations are insufficient. On the other hand, it would be difficult to use our proposed method to construct a conjugated fault system or a multiple plane fault, such as the faults of the M_W 7.8 2016 Kaikoura, New Zealand, and the M_W 7.9 2018 Alaska earthquakes.

In each application of our method to both synthetic and real waveforms, it took only a few iterations of the finite-fault inversion to construct fault geometry, which was expected from the assumption that the fault geometry can be constructed from strike or dip data alone. Although this assumption results in a weak nonlinearity in our method, nonlinearities may also originated from the low spatial resolution of teleseismic data and the fact that the uncertainty of Green's function is well defined in the potency density tensor inversion and its framework (Yagi & Fukahata, 2011a).

Our proposed method is optimized for application to teleseismic P waveform data because modeling error of teleseismic P-wave Green's function is explicitly taken into account in the inversion formulation used in this study. It would be possible to use teleseismic S waveforms jointly and geodetic data by defining possible errors of picking first motion of S-phase and modeling error of geodetic Green's function. Although the spatial resolution of the fault geometry constructed by our proposed method is limited by the product of the sampling interval of waveform data and the assumed maximum rupture front velocity, the joint use of geodetic data would increase the spatial resolution and constrain the absolute location of the constructed fault geometry.

4. General discussion

This dissertation proposes two methods to probe fault geometry ruptured during earthquake. One method is the potency density tensor inversion, which enables us to estimate spatiotemporal potency density tensor distribution within a framework of finite-fault inversion of teleseismic waveforms. By taking into account the relative sensitivity of teleseismic P-wave Green's function to slip direction, that method no longer requires detailed assumption of fault geometry which has been an inevitable constraint in finite-fault source modeling, making it possible to obtain less biased source model and opening window to flexible seismic source inversion. Because the obtained potency density tensor distribution represents fault geometry during rupture propagation, the potency density tensor inversion unwraps relationships between rupture propagation and fault geometry by using only teleseismic P waveforms. The multiple point source inversions (e.g. Kikuchi & Kanamori, 1991; Duputel *et al.*, 2012b) resolve a focal mechanism for each subevent under an assumption of a simplified source-time function but miss rupture propagation between subevents as well as a change of focal mechanism during a subevent. It is natural for a focal mechanism to vary in space and time during a subevent, and the source-time function generally reflects the directivity effect and hence should be able to express azimuth-dependent shapes and durations. Therefore, it is difficult for multiple point source inversion approach to estimate detailed rupture propagation between subevents and smoothly curved fault geometry, such as those of the 2013 Balochistan earthquake. On the other hand, the potency density tensor inversion flexibly estimates spatiotemporal potency density tensor distribution representing rupture propagation and variation of the focal mechanism without non-negative slip constraint, which is a clear advantage over the multiple point source inversions. So far, the potency density tensor inversion has been applied to analyses for earthquakes other than the 2013 Balochistan and the 2015 Gorkha earthquakes, such as the 2016 M_{W} 7.1 Romanche (Hicks *et al.*, 2020), the M_{W} 7.6 2018 Palu Indonesia (Okuwaki *et al.*, 2020; Aránguiz *et al.*, 2020), the M_{W} 7.9 2018 Gulf of Alaska (Yamashita *et al.*, 2021), the M_{W} 8.0 2019 Peru (Hu *et al.*, 2021), and the M_{W}

7.7 2020 Caribbean (Tadapansawut *et al.*, 2021) earthquakes, and is expected to continue to contribute to detailed understanding of seismic source process and regional tectonics.

Another one is an approach to construct fault geometry, which is a nonlinear inversion method and updates model fault geometry by performing the potency density tensor inversion iteratively. As mentioned in Section 3.4, for earthquakes that ruptured geometrically continuous and smooth fault, this method works well for constructing its fault geometry and reveals a more direct relationship between rupture propagation and fault geometry than running the potency density tensor inversion analysis once. Therefore, it is desirable to use the potency density tensor inversion for earthquakes with drastic change in fault geometry, and to construct the geometry for earthquakes with geometrically continuous and smooth changes in fault geometry. The two methods using teleseismic waveforms can be applied to analyze a variety of earthquakes regardless of the source region, such as under seafloors where geodetic observation is difficult to obtain, and would be used to reveal geometry of faults existing inland but also geometry of subducting slab through an application to analysis of interplate earthquake, such as the M_W 9.1 2011 Tohoku-oki and the M_W 7.6 2012 Nicoya, Costa Rica earthquakes.

4.1 Effects of smoothing constraints

The potency density tensor inversion solves 2.5 times larger number of model parameters than the conventional methods (Fig. 2.1), which is equivalent to a freedom from the constraint on shear-slip direction that is one of prior constraints imposed implicitly in conventional methods. A noteworthy prior probability density function adopted by the potency density tensor inversion method is the smoothing constraint. As discussed in Section 2.1, the potency density tensor inversion adopts the ABIC without the non-negative constraint, and over- and under-smoothing problem can be avoided. However, this method tends to solve smooth potency density tensor distribution in space and time, and inferred focal mechanisms contain CLVD components even when a true source mechanism is a pure double couple, which can be found in the synthetic tests (Figs 2.2–2.5).

The spatial resolution of the fault geometry constructed by the iterative inversion approach developed in Chapter 3 is limited by the product of the sampling interval of waveform data and the assumed maximum rupture front velocity, but may be lower due to the smoothing constraints adopted by the potency density tensor inversion, making the constructed fault model geometrically smooth. Furthermore, it is difficult for the potency density tensor inversion to constrain the strike of low angle thrust fault due to the contamination of CLVD components, such as that of the Gorkha earthquake (Fig. 3.10). This makes it difficult to use strike angles to construct fault geometry of such low angle thrust by using our proposed method and was the reason why we used only dip angles to construct the fault geometry of the Gorkha earthquake in Chapter 3. It would be necessary to adopt a smoothing constraint providing a sharper source image for constructing finer geometric structures of fault.

Recently, Yamashita *et al.* (2021) tackled this problem and succeeded in resolving finer source image with an approach that makes the strength of the smoothing constraint even among basis double-couple components. They are also working on developing a new smoothing constraint that makes the strength of the smoothness spatiotemporally even among basis double-couple components (Yamashita *et al.*, 2021b), and the combination of the new smoothing constraint and our method would enable us to construct more detailed fault geometries.

4.2 Future prospects for seismic source process analysis

In Chapter 3, we assumed for simplicity that the fault geometry to be constructed changes only either along strike or along dip (Fig. 3.1), but in general, earthquake faults have three dimensional variation of geometry. It is possible to use both strike and dip to construct highly non-planar fault geometry in principle but should be considered that a finite-fault inversion scheme needs to allow subfaults that differ greatly in their respective areas or to adopt triangular subfaults instead of rectangular ones. In a study similar to ours, Dutta *et al.* (2021) proposed a methodology that constructs three-dimensionally non-planar fault geometry and estimates spatial distribution of slip from geodetic data within a framework of Bayesian inference. They adopted triangular subfaults in their finite-fault inversion but only considered geometrically continuous fault, neglecting discontinuity of fault. It would also be necessary for constructing three-dimensionally non-planar fault to consider how to distinguish between discontinuous areas and stretched areas in fault.

Finite-fault inversion of seismic waveforms generally requires data processing and parameter setting, such as fault geometry and area, rupture duration, and maximum rupture velocity, which makes it difficult to automatically obtain a reliable source model immediately after an earthquake. The potency density tensor inversion is free from detailed assumption of fault geometry which has been one of the settings that greatly affect the results of inversion and is a huge obstruction to automation inversion analysis. It can be said that the development of potency density tensor inversion has taken a step forward in automating inversion analysis.

5. Conclusion

In this dissertation, we developed new finite-fault inversion approaches to simultaneously estimate fault geometry and rupture evolution during earthquake. In Chapter 2, we proposed a new finite-fault inversion of teleseismic *P* waveforms, named potency density tensor inversion, which represents shear slip along an assumed fault by a superposition of five basis double-couple components. By adopting the formulation of Yagi & Fukahata (2011a) as the fundamental framework, the new method makes it possible not only to extract information on fault geometry during rupture propagation but also to suppress effects originated from uncertainties of Green's function and fault geometry, which are two major sources of modeling errors. Through numerical simulations and application to real waveforms, we evaluated effectiveness and flexibility of the potency density tensor inversion method and conclude that the new method is applicable to an earthquake that involves geometrically complex fault and makes it possible to provide information of the fault geometry, contributing to more reliable and informative source modeling. In Chapter 3, we proposed an approach of constructing fault geometry that uses only teleseismic data and performs potency density tensor inversion iteratively. We assumed that an estimated fault bends only along the strike or only in the dip direction, which contributes to weaken a nonlinearity of the iterative approach. We tested the performance of the method by conducting numerical simulations and then applied this method to teleseismic waveforms of the 2013 Balochistan and 2015 Gorkha earthquakes, which occurred along geometrically complex fault systems. Results of applications for both events showed that the estiamted fault geometry were consistent with geometric models proposed by previous studies based on different observational data. This method is suitable for constructing fault geometries for earthquakes that rupture geometrically smooth and continuous fault surfaces. These two developed methods are expected to reveal fault geometry and its relation to rupture propagation by using only teleseismic data, and deepen our understanding of earthquake dynamics and regional tectonics.

6. Acknowledgments

Teleseismic waveforms of the following networks: the United States National Seismic Network, Pacific21, the MEDNET Project, GEOFON, Czech Regional Seismic Network, the Canadian National Seismograph Network, Global Seismograph Network (GSN-IRIS/USGS), Global Seismograph Network (GSN-IRIS/IDA), New China Digital Seismograph Network, Global Telemetered Seismograph Network (USAF/USGS), Hong Kong Seismographic Network, and GEOSCOPE, were obtained from the IRIS-DMC website (https://ds.iris.edu/ds/nodes/dmc/). The figures were generated with ObsPy (Krischer *et al.*, 2015; Megies *et al.*, 2011; Beyreuther *et al.*, 2010, Version 1.2.1; http://doi.org/10.5281/zenodo.3706479), matplotlib (Hunter, 2007, Version 3.2.1; https://doi.org/10.5281/zenodo.3714460), and Generic Mapping Tools (Wessel *et al.*, 2013). This dissertation was written in LaTeX.
First of all, I would like to pay my special regards to my supervisor, Prof. Yuji Yagi. He invited me to take a PhD course and warmly welcomed me to his laboratory again for the first time in two years after graduation. He also supported my research life while continuing my current work at the Japan Meteorological Agency. The staff at the student office of University of Tsukuba were very sincere in their support and administrative procedures related to the PhD program, and I greatly appreciate it. I would like to express my gratitude and appreciation for Ryo Okuwaki, Assistant Professor of University of Tsukuba, who encouraged me to take a PhD course and provided me valuable and insightful comments. Yukitoshi Fukahata, Associate Professor of Disaster Prevention Research Institute, Kyoto University, gave me insightful comments and suggestions, and I would like to offer my special thanks to him. I am also grateful to the members of Prof. Yagi's laboratory for their helpful comments and supports. Especially, Shinji Yamashita, a Master course student, supported my remote research activity and I would like to thank him. I would like to thank my current colleagues, expecially my boss, at the Japan Meteorological Agency for their encouragements. Finally, I sincerely thank to my family for supports and encouragements.

References

Akaike, H., 1980. Likelihood and the Bayes procedure. *Trabajos de Estadistica Y de Investigacion Operativa*, **31**(1), 143–166. doi:10.1007/BF02888350.

Aki, K., 1979. Characterization of barriers on an earthquake fault. *Journal of Geophysical Research: Solid Earth*, **84**(B11), 6140–6148. doi:10.1029/JB084iB11p06140.

Aki, K. & Richards, P. G., 2002. *Quantitative Seismology*.

Ampuero, J. P. & Dahlen, F. A., 2005. Ambiguity of the moment tensor. *Bulletin of the Seismological Society of America*, **95**(2), 390–400. doi:10.1785/0120040103.

Aránguiz, R., Esteban, M., Takagi, H., Mikami, T., Takabatake, T., Gómez, M., González, J., Shibayama, T., Okuwaki, R., Yagi, Y., Shimizu, K., Achiari, H., Stolle, J., Robertson, I., Ohira, K., Nakamura, R., Nishida, Y., Krautwald, C., Goseberg, N., & Nistor, I., 2020. The 2018 Sulawesi tsunami in Palu city as a result of several landslides and coseismic tsunamis. *Coastal Engineering Journal*, **62**(4), 445–459. doi:10.1080/21664250.2020.1780719.

Asano, K. & Iwata, T. Kinematic Source Inversion using Strong Motion Data Considering Three-Dimensional Fault Geometry. In *AGU Fall Meeting Abstracts*, volume 2009, pages S31A–1688, 2009.

Avouac, J. P., Ayoub, F., Wei, S., Ampuero, J. P., Meng, L., Leprince, S., Jolivet, R., Duputel, Z., & Helmberger, D., 2014. The 2013, Mw 7.7 Balochistan earthquake, energetic strike-slip reactivation of a thrust fault. *Earth and Planetary Science Letters*, **391**, 128–134. doi:10.1016/j.epsl.2014.01.036.

Avouac, J.-P., Meng, L., Wei, S., Wang, T., & Ampuero, J.-P., 2015. Lower edge of locked Main Himalayan Thrust unzipped by the 2015 Gorkha earthquake. *Nature Geoscience*, **8** (9), 708–711. doi:10.1038/ngeo2518.

Backus, G. & Mulcahy, M., 1976. Moment Tensors and other Phenomenological Descriptions of Seismic Sources—I. Continuous Displacements. *Geophysical Journal International*, **46** (2), 341–361.

Barnhart, W. D., Hayes, G. P., Briggs, R. W., Gold, R. D., & Bilham, R., 2014. Ball-and-socket tectonic rotation during the 2013 Mw7.7 Balochistan earthquake. *Earth and Planetary Science Letters*, **403**, 210–216. doi:10.1016/j.epsl.2014.07.001.

Beresnev, I. A., 2003. Uncertainties in finite-fault slip inversions: To what extent to believe? (A critical review). *Bulletin of the Seismological Society of America*, **93**(6), 2445–2458. doi:10.1785/0120020225.

Beyreuther, M., Barsch, R., Krischer, L., Megies, T., Behr, Y., & Wassermann, J., 2010. ObsPy: A Python Toolbox for Seismology. *Seismological Research Letters*, **81**(3), 530–533. doi:10.1785/gssrl.81.3.530.

Bodin, T., Sambridge, M., & Gallagher, K., 2009. A self-parametrizing partition model approach to tomographic inverse problems. *Inverse Problems*, **25**(5). doi:10.1088/0266-5611/25/5/055009.

Dal Zilio, L., van Dinther, Y., Gerya, T., & Avouac, J.-P., 2019. Bimodal seismicity in the Himalaya controlled by fault friction and geometry. *Nature Communications*, **10**(1), 48. doi:10.1038/s41467-018-07874-8.

Danielson, J. J. & Gesch, D. B. Global multi-resolution terrain elevation data 2010 (GMTED2010). Technical report, 2011. URL http://pubs.er.usgs.gov/publication/ofr20111073.

DeMets, C., Gordon, R. G., & Argus, D. F., 2010. Geologically current plate motions. *Geophysical Journal International*, **181**(1), 1–80. doi:10.1111/j.1365-246X.2009.04491.x.

Du, Y., Aydin, A., & Segall, P., 1992. Comparison of various inversion techniques as applied to the determination of a geophysical deformation model for the 1983 Borah Peak earthquake. *Bulletin of the Seismological Society of America*, **82**(4), 1840–1866.

Duputel, Z. & Rivera, L., 2017. Long-period analysis of the 2016 Kaikoura earthquake. *Physics of the Earth and Planetary Interiors*, **265**, 62–66. doi:10.1016/j.pepi.2017.02.004.

Duputel, Z., Kanamori, H., Tsai, V. C., Rivera, L., Meng, L., Ampuero, J. P., & Stock, J. M., 2012a. The 2012 Sumatra great earthquake sequence. *Earth and Planetary Science Letters*, **351-352**, 247–257. doi:10.1016/j.epsl.2012.07.017.

Duputel, Z., Rivera, L., Kanamori, H., & Hayes, G., 2012b. W phase source inversion for moderate to large earthquakes (1990-2010). *Geophysical Journal International*, **189**(2), 1125–1147. doi:10.1111/j.1365-246X.2012.05419.x.

Duputel, Z., Agram, P. S., Simons, M., Minson, S. E., & Beck, J. L., 2014. Accounting for prediction uncertainty when inferring subsurface fault slip. *Geophysical Journal International*, **197**(1), 464–482. doi:10.1093/gji/ggt517.

Duputel, Z., Vergne, J., Rivera, L., Wittlinger, G., Farra, V., & Hetényi, G., 2016. The 2015 Gorkha earthquake: A large event illuminating the Main Himalayan Thrust fault. *Geophysical Research Letters*, **43**(6), 2517–2525. doi:10.1002/2016GL068083.

Dutta, R., Jónsson, S., & Vasyura-Bathke, H., 2021. Simultaneous Bayesian Estimation of Non-Planar Fault Geometry and Spatially-Variable Slip. *Journal of Geophysical Research: Solid Earth*, **126**(7). doi:10.1029/2020JB020441.

Dziewonski, A. M., Chou, T., & Woodhouse, J., 1981. Determination of earthquake source parameters from waveform data for studies of global and regional seismicity. *Journal of Geophysical Research: Solid Earth*, **86**(B4), 2825–2852. doi:10.1029/JB086iB04p02825.

Ekström, G., Nettles, M., & Dziewoński, A. M., 2012. The global CMT project 2004 - 2010: Centroid-moment tensors for 13,017 earthquakes. *Physics of the Earth and Planetary Interiors*, **200-201**, 1–9. doi:10.1016/j.pepi.2012.04.002.

Elliott, J. R., Jolivet, R., Gonzalez, P. J., Avouac, J. P., Hollingsworth, J., Searle, M. P., & Stevens, V. L., 2016. Himalayan megathrust geometry and relation to topography revealed by the Gorkha earthquake. *Nature Geoscience*, **9**(2), 174–180. doi:10.1038/ngeo2623.

Fielding, E. J., Sladen, A., Li, Z., Avouac, J. P., Bürgmann, R., & Ryder, I., 2013. Kinematic fault slip evolution source models of the 2008 M7.9 wenchuan earthquake in china from SAR interferometry, GPS and teleseismic analysis and implications for longmen shan tectonics. *Geophysical Journal International*, **194**(2), 1138–1166. doi:10.1093/gji/ggt155.

Freymueller, J., King, N. E., & Segall, P., 1994. The Coseismic Slip Distribution of the Landers Earthquake. *Bulletin of the Seismological Society of America*, **84**(3), 646–659.

Fukahata, Y. & Wright, T. J., 2008. A non-linear geodetic data inversion using ABIC for slip distribution on a fault with an unknown dip angle. *Geophysical Journal International*, **173** (2), 353–364. doi:10.1111/j.1365-246X.2007.03713.x.

Fukahata, Y., Yagi, Y., & Matsu'ura, M., 2003. Waveform inversion for seismic source processes using ABIC with two sorts of prior constraints: Comparison between proper and improper formulations. *Geophysical Research Letters*, **30**(6), 1–4. doi:10.1029/2002GL016293.

Fukahata, Y., Nishitani, A., & Matsu'ura, M., 2004. Geodetic data inversion using ABIC to estimate slip history during one earthquake cycle with viscoelastic slip-response functions. *Geophysical Journal International*, **156**(1), 140–153. doi:10.1111/j.1365-246X.2004.02122.x.

Fukuda, J. & Johnson, K. M., 2008. A fully Bayesian inversion for spatial distribution of fault slip with objective smoothing. *Bulletin of the Seismological Society of America*, **98**(3), 1128–1146. doi:10.1785/0120070194.

Haghipour, N., Burg, J. P., Kober, F., Zeilinger, G., Ivy-Ochs, S., Kubik, P. W., & Faridi, M., 2012. Rate of crustal shortening and non-Coulomb behaviour of an active accretionary wedge: The folded fluvial terraces in Makran (SE, Iran). *Earth and Planetary Science Letters*, **355-356**, 187–198. doi:10.1016/j.epsl.2012.09.001.

Hartzell, S. H. & Heaton, T. H., 1983. Inversion of strong ground motion and teleseismic waveform data for the fault rupture history of the 1979 Imperial Valley, California, earthquake. *Bulletin of the Seismological Society of America*, **73**(6), 1553–1583.

Hayes, G. P., 2017. The finite, kinematic rupture properties of great-sized earthquakes since 1990. *Earth and Planetary Science Letters*, **468**(June 2016), 94–100. doi:10.1016/j.epsl.2017.04.003.

Hicks, S. P., Okuwaki, R., Steinberg, A., Rychert, C. A., Harmon, N., Abercrombie, R. E., Bogiatzis, P., Schlaphorst, D., Zahradnik, J., Kendall, J.-M., Yagi, Y., Shimizu, K., &

Sudhaus, H., 2020. Back-propagating supershear rupture in the 2016 Mw 7.1 Romanche transform fault earthquake. *Nature Geoscience*, **13**(9), 647–653. doi:10.1038/s41561-020-0619-9.

Hu, Y., Yagi, Y., Okuwaki, R., & Shimizu, K., 2021. Back-propagating rupture evolution within a curved slab during the 2019 Mw 8.0 Peru intraslab earthquake. *Geophysical Journal International*, **227**(3), 1602–1611. doi:10.1093/gji/ggab303.

Hubbard, J., Almeida, R., Foster, A., Sapkota, S. N., Bürgi, P., & Tapponnier, P., 2016. Structural segmentation controlled the 2015 MW 7.8 Gorkha earthquake rupture in Nepal. *Geology*, **44**(8), 639–642. doi:10.1130/G38077.1.

Hunter, J. D., 2007. Matplotlib: A 2D graphics environment. *Computing in Science & Engineering*, **9**(3), 90–95. doi:10.1109/MCSE.2007.55.

Ide, S., Takeo, M., & Yoshida, Y., 1996. Source Process of the 1995 Kobe Earthquake: Determination of SpatioTemporal Slip Distribution by Bayesian Modeling. *Bulletin of the Seismological Society of America*, **86**(3), 547–566.

Ji, C., Wald, D. J., & Helmberger, D. V., 2002. Source description of the 1999 Hector Mine, California, earthquake, part I: Wavelet domain inversion theory and resolution analysis. *Bulletin of the Seismological Society of America*, **92**(4), 1192–1207. doi:10.1785/0120000916.

Jolivet, R., Duputel, Z., Riel, B., Simons, M., Rivera, L., Minson, S. E., Zhang, H., Aivazis, M. A., Ayoub, F., Leprince, S., Samsonov, S., Motagh, M., & Fielding, E. J., 2014. The 2013 Mw7.7 Balochistan earthquake: Seismic potential of an accretionary wedge. *Bulletin of the Seismological Society of America*, **104**(2), 1020–1030. doi:10.1785/0120130313.

Kikuchi, M. & Kanamori, H., 1991. Inversion of Complex Body Waves-III. *Bulletin of the Seismological Society of America*, **81**(6), 2335–2350.

Koketsu, K., Hikima, K., Miyazaki, S., & Ide, S., 2004. Joint inversion of strong motion and geodetic data for the source process of the 2003 Tokachi-oki, Hokkaido, earthquake. *Earth, Planets and Space*, **56**(3), 329–334. doi:10.1186/BF03353060.

Krischer, L., Megies, T., Barsch, R., Beyreuther, M., Lecocq, T., Caudron, C., & Wassermann, J., 2015. ObsPy: a bridge for seismology into the scientific Python ecosystem. *Computational Science & Discovery*, **8**(1), 14003. doi:10.1088/1749-4699/8/1/014003.

Laske, G., Masters, G., Ma, Z., & Pasyanos, M., 2013. Update on CRUST1.0—A 1-degree global model of Earth's crust. *EGU General Assembly 2013*, **15**, 2658.

Mai, P. M., Spudich, P., & Boatwright, J., 2005. Hypocenter Locations in Finite-Source Rupture Models. *Bulletin of the Seismological Society of America*, **95**(3), 965–980. doi:10.1785/0120040111.

Mai, P. M., Schorlemmer, D., Page, M., Ampuero, J., Asano, K., Causse, M., Custodio, S., Fan, W., Festa, G., Galis, M., Gallovic, F., Imperatori, W., Käser, M., Malytskyy, D., Okuwaki, R., Pollitz, F., Passone, L., Razafindrakoto, H. N. T., Sekiguchi, H., Song, S. G., Somala, S. N., Thingbaijam, K. K. S., Twardzik, C., van Driel, M., Vyas, J. C., Wang, R., Yagi, Y., & Zielke, O., 2016. The Earthquake - Source Inversion Validation (SIV) Project. *Seismological Research Letters*, **87**(3), 690–708. doi:10.1785/0220150231.

Megies, T., Beyreuther, M., Barsch, R., Krischer, L., & Wassermann, J., 2011. ObsPy - What can it do for data centers and observatories? *Annals of Geophysics*, **54**(1), 47–58.

Meier, M.-A., Ampuero, J. P., & Heaton, T. H., 2017. The hidden simplicity of subduction megathrust earthquakes. *Science*, **357**(6357), 1277 LP – 1281. doi:10.1126/science.aan5643.

Minson, S. E., Simons, M., & Beck, J. L., 2013. Bayesian inversion for finite fault earthquake source models I-theory and algorithm. *Geophysical Journal International*, **194**(3), 1701–1726. doi:10.1093/gji/ggt180.

Nocquet, J. M., 2018. Stochastic static fault slip inversion from geodetic data with non-negativity and bound constraints. *Geophysical Journal International*, **214**(1), 366–385. doi:10.1093/gji/ggy146.

Okuwaki, R. & Yagi, Y., 2017. Rupture Process During the Mw 8.1 2017 Chiapas Mexico Earthquake: Shallow Intraplate Normal Faulting by Slab Bending. *Geophysical Research Letters*, **44**(23), 11,816–11,823. doi:10.1002/2017GL075956.

Okuwaki, R. & Yagi, Y., 2018. Role of geometric barriers in irregular-rupture evolution during the 2008 Wenchuan earthquake. *Geophysical Journal International*, **212**(3), 1657–1664. doi:10.1093/gji/ggx502.

Okuwaki, R., Kasahara, A., Yagi, Y., Hirano, S., & Fukahata, Y., 2019. Backprojection to image slip. *Geophysical Journal International*, **216**, 1529–1537. doi:10.1093/gji/ggy505.

Okuwaki, R., Hirano, S., Yagi, Y., & Shimizu, K., 2020. Inchworm-like source evolution through a geometrically complex fault fueled persistent supershear rupture during the 2018 Palu Indonesia earthquake. *Earth and Planetary Science Letters*, **547**, 116449. doi:10.1016/j.epsl.2020.116449.

Olson, A. H. & Apsel, R. J., 1982. Finite faults and inverse theory with applications to the 1979 Imperial Valley earthquake. *Bulletin of the Seismological Society of America*, **72**(6), 1969–2001.

Qiu, Q., Hill, E. M., Barbot, S., Hubbard, J., Feng, W., Lindsey, E. O., Feng, L., Dai, K., Samsonov, S. V., & Tapponnier, P., 2016. The mechanism of partial rupture of a locked megathrust: The role of fault morphology. *Geology*, **44**(10), 875–878. doi:10.1130/G38178.1.

Ragon, T., Sladen, A., & Simons, M., 2018. Accounting for uncertain fault geometry in earthquake source inversions - I : theory and simplified application. *Geophysical Journal International*, **214**, 1174–1190. doi:10.1093/gji/ggy187.

Shi, Q., Wei, S., & Chen, M., 2018. An MCMC multiple point sources inversion scheme and its application to the 2016 Kumamoto Mw 6.2 earthquake. *Geophysical Journal International*, **215**(2), 737–752. doi:10.1093/gji/ggy302.

Shimizu, K., Yagi, Y., Okuwaki, R., & Fukahata, Y., 2020. Development of an inversion method to extract information on fault geometry from teleseismic data. *Geophysical Journal International*, **220**(2), 1055–1065. doi:10.1093/gji/ggz496.

Shimizu, K., Yagi, Y., Okuwaki, R., & Fukahata, Y., 2021. Construction of fault geometry by finite-fault inversion of teleseismic data. *Geophysical Journal International*, **224**(2), 1003–1014. doi:10.1093/gji/ggaa501.

Tadapansawut, T., Okuwaki, R., Yagi, Y., & Yamashita, S., 2021. Rupture Process of the 2020 Caribbean Earthquake Along the Oriente Transform Fault, Involving Supershear Rupture and Geometric Complexity of Fault. *Geophysical Research Letters*, **48**(1), e2020GL090899. doi:10.1029/2020GL090899.

Trifunac, M., 1974. A three dimensional dislocation model for the San Fernando, California, earthquake of February 9, 1971. *Bulletin of the Seismological Society of America*, **64**(1), 149–172.

Wald, D. J. & Heaton, T. H., 1994. Spatial and temporal distribution of slip for the 1992 Landers, California, earthquake. *Bulletin of the Seismological Society of America*, **84**(3), 668–691.

Wang, D., Kawakatsu, H., Mori, J., Ali, B., Ren, Z., & Shen, X., 2016. Backprojection analyses from four regional arrays for rupture over a curved dipping fault: The Mw7.7 24 September 2013 Pakistan earthquake. *Journal of Geophysical Research: Solid Earth*, **121**(3), 1948–1961. doi:10.1002/2015JB012168.

Wessel, P., Smith, W. H. F., Scharroo, R., Luis, J., & Wobbe, F., 2013. Generic Mapping Tools: Improved Version Released. *Eos, Transactions American Geophysical Union*, **94**(45), 409–410. doi:10.1002/2013EO450001.

Yabuki, T. & Matsu'ura, M., 1992. Geodetic data inversion using a Bayesian information criterion for spatial distribution of fault slip. *Geophysical Journal International*, **109**(2), 363–375. doi:10.1111/j.1365-246X.1992.tb00102.x.

Yagi, Y. & Fukahata, Y., 2011a. Introduction of uncertainty of Green's function into waveform inversion for seismic source processes. *Geophysical Journal International*, **186**(2), 711–720. doi:10.1111/j.1365-246X.2011.05043.x.

Yagi, Y. & Fukahata, Y., 2011b. Rupture process of the 2011 Tohoku-oki earthquake and absolute elastic strain release. *Geophysical Research Letters*, **38**(19), 1–5. doi:10.1029/2011GL048701.

Yagi, Y. & Okuwaki, R., 2015. Integrated seismic source model of the 2015 Gorkha, Nepal, earthquake. *Geophysical Research Letters*, **42**(15), 6229–6235. doi:10.1002/2015GL064995.

Yagi, Y., Nakao, A., & Kasahara, A., 2012a. Smooth and rapid slip near the Japan Trench during the 2011 Tohoku-oki earthquake revealed by a hybrid back-projection method. *Earth and Planetary Science Letters*, **355-356**, 94–101. doi:10.1016/j.epsl.2012.08.018.

Yagi, Y., Nishimura, N., & Kasahara, A., 2012b. Source process of the 12 May 2008 Wenchuan, China, earthquake determined by waveform inversion of teleseismic body waves with a data covariance matrix. *Earth, Planets and Space*, **64**(7), e13–e16. doi:10.5047/eps.2012.05.006.

Yamashita, S., Yagi, Y., Okuwaki, R., Shimizu, K., Agata, R., & Fukahata, Y., 2021. Consecutive ruptures on a complex conjugate fault system during the 2018 Gulf of Alaska earthquake. *Scientific Reports*, **11**(1), 5979. doi:10.1038/s41598-021-85522-w.

Yamashita, S., Yagi, Y., Okuwaki, R., Shimizu, K., Agata, R., & Fukahata, Y., 2021b. Potency density tensor inversion of complex body waveforms introducing time-adaptive smoothing constraint. *EarthArXiv*. doi:10.31223/X5JW4V.

Ye, L., Lay, T., Kanamori, H., & Rivera, L., 2016. Rupture characteristics of major and great (Mw ⊠⊠⊠ 7.0) megathrust earthquakes from 1990 to 2015: 1. *Journal of Geophysical Research: Solid Earth*, **121**(2), 826–844. doi:10.1002/2015JB012426.

Ye, L., Lay, T., Bai, Y., Cheung, K. F., & Kanamori, H., 2017. The 2017 Mw 8.2 Chiapas, Mexico, Earthquake: Energetic Slab Detachment. *Geophysical Research Letters*, **44**(23), 11,811–824,832. doi:10.1002/2017GL076085.

Yue, H. & Lay, T., 2020. Resolving Complicated Faulting Process Using Multi-Point-Source Representation: Iterative Inversion Algorithm Improvement and Application to Recent Complex Earthquakes. *Journal of Geophysical Research: Solid Earth*, **125**(2), 1–24. doi:10.1029/2019JB018601.

Yue, H., Lay, T., Schwartz, S. Y., Rivera, L., Protti, M., Dixon, T. H., Owen, S., & Newman, A. V., 2013. The 5 September 2012 Nicoya, Costa Rica Mw 7.6 earthquake rupture process from joint inversion of high-rate GPS, strong-motion, and teleseismic P wave data and its relationship to adjacent plate boundary interface properties. *Journal of Geophysical Research: Solid Earth*, **118**(10), 5453–5466. doi:10.1002/jgrb.50379.

Zinke, R., Hollingsworth, J., & Dolan, J. F., 2014. Surface slip and off-fault deformation patterns in the 2013 Mw7.7 Balochistan, Pakistan earthquake: Implications for controls on the distribution of near-surface coseismic slip. *Geochemistry, Geophysics, Geosystems*, **15** (12), 5034–5050. doi:10.1002/2014GC005538.